Strength and Behaviour of Double-coped Steel Beams under Combined Loads

by

Graeme Johnston

A thesis submitted in partial fulfillment of the requirements for the degree of

Master of Science

in

Structural Engineering

Department of Civil and Environmental Engineering
University of Alberta

ABSTRACT

Current design procedures for double-coped beams tend to be overly conservative and do not include considerations for axial load. The reduced strength and stability of the coped region increase the susceptibility of the connection to a local failure, and the complexity of the connection behaviour is compounded if axial load is present in addition to shear. However, this behaviour is not well understood due to a lack of research. No published research exists on the full-scale physical testing of double-coped beams.

To address these problems, an investigation into the strength and behaviour of double-coped beams was completed by testing 29 full-scale specimens. Test specimens varied in beam depth and cope length to represent geometries found in typical structures that may be susceptible to stability issues. The specimens were subjected to a combination of shear, as well as axial loads that varied from 100 kN in tension to 300 kN in compression, and were tested at reasonable upper and lower bounds for typical beam end rotations and end-support conditions.

Critical failure modes of the double-coped beam tests are described and the effects of the test variables on the behaviour and strength of the connections are discussed. Based on the test results, four design procedures are assessed for their ability to predict the failure mode and capacity of the connections accurately. Conclusions are made on the strength, behaviour, and ductility of double-coped beams based on the tested variables.

ACKNOWLEDGEMENTS

Funding for this research project was provided by the Natural Sciences and Engineering Research Council of Canada and the Steel Structures Education Foundation. Financial support in the form of scholarships from the University of Alberta, the Government of Alberta, and DIALOG are gratefully acknowledged. In-kind support, in the form of donation and fabrication of the test specimens, was provided by Waiward Steel Fabricators of Edmonton, AB.

TABLE OF CONTENTS

LIST OF TABLES

LIST OF FIGURES

LIST OF SYMBOLS

A	=	cross-sectional area
C_b	=	moment gradient coefficient for lateral–torsional buckling
C_e	=	Euler buckling strength
C_f	=	compressive force in a member
C_r	=	resistance to compressive load
c	=	cope length
c_b	=	length of bottom cope
c_t	=	length of top cope
d	=	beam depth
d_c	=	cope depth
d_{cb}	=	depth of bottom cope
d_{ct}	=	depth of top cope
E	=	modulus of elasticity
e	=	geometric eccentricity
e_{eff}	=	effective eccentricity
F_{cr}	=	flexural local buckling stress
F_e	=	Euler's buckling stress
F_u	=	ultimate strength
F_y	=	specified minimum yield strength
f	=	plate buckling model adjustment factor
f_d	=	adjustment factor
G	=	shear modulus
h_0	=	reduced beam depth
I	=	moment of inertia
I_x	=	strong-axis moment of inertia
I_y	=	weak-axis moment of inertia
J	=	St. Venant torsional constant
k	=	plate buckling coefficient

k_d	=	effective length factor
K	=	effective length factor for column buckling
L	=	length of compression element; length of finite element cantilever model
L_b	=	distance between brace points
M	=	moment
$M_{cope\ face}$	=	moment at the face of the cope
M_{cr}	=	critical buckling moment
$M_{end\text{-}plate}$	=	moment at the face of the end-plate
M_n	=	available flexural strength; nominal moment
M_{net}	=	moment at the net section at the beginning of the re-entrant corners
M_p	=	plastic moment
$M_{p,v}$	=	plastic moment, reduced to account for the required shear load
$M_{p,vp}$	=	plastic moment, reduced to account for the required shear and axial load
$M_{support}$	=	moment at the support
M_u	=	critical elastic moment of a laterally unbraced beam
M_{weld}	=	moment at the toe of the fillet weld to the end-plate
M_y	=	yield moment
n	=	parameter for compressive resistance
P	=	nominal applied axial load
P_y	=	axial yield load
Q	=	first moment of area; nondimensional yield stress reduction factor for plate buckling
r	=	radius of gyration
S_{net}	=	net section modulus
S_x	=	elastic modulus
t	=	element thickness
t_e	=	end-plate thickness
t_w	=	web thickness

$t_{w,min}$	=	minimum web thickness to prevent lateral–torsional buckling
U_1	=	factor to account for moment gradient and second-order effects of gravity loads acting on the deformed member
V	=	shear
V_y	=	elastic shear strength
V_p	=	plastic shear strength
y	=	distance from neutral axis to extreme fibre
Z	=	plastic modulus
κ	=	ratio of smaller end moment to larger, positive for double curvature and negative for single curvature
λ	=	slenderness parameter
λ_p	=	limiting slenderness for the limit state of yielding
λ_r	=	limiting slenderness for the limit state of inelastic lateral–torsional buckling
ν	=	Poisson's ratio
σ	=	normal stress
σ_{cr}	=	critical normal stress
τ	=	shear stress
ω_1	=	coefficient to determine equivalent uniform bending effect in beam-columns
ω_2	=	coefficient to account for increased moment resistance of a laterally unsupported doubly symmetric beam segment when subject to a moment gradient

CHAPTER 1: INTRODUCTION

1.1 Statement of Problem

Often steel framed buildings maintain a constant floor height by constraining the top flanges of beams and supporting girders to the same elevation. Removing a portion of the beam flanges, known as "coping", is commonly used to eliminate interferences between the beam and the supporting member. Beams may be coped at the top flange only, bottom flange only, or both the top and bottom flanges, depending on the connection geometry and layout. Commonly, coped beams are used in beam-to-girder connections, and, in situations where the supporting girder depth is greater than the beam depth, shown schematically in Figure 1-1(a), a single cope is required—typically the top (compression) flange. Copes are required at both flanges in situations where the girder depth and beam depth are equal, shown schematically in Figure 1-1(b). In both cases, the "coped region" remaining after the removal of the flange(s) has an increased susceptibility to failure due to a reduction in strength and lateral and torsional stiffness.

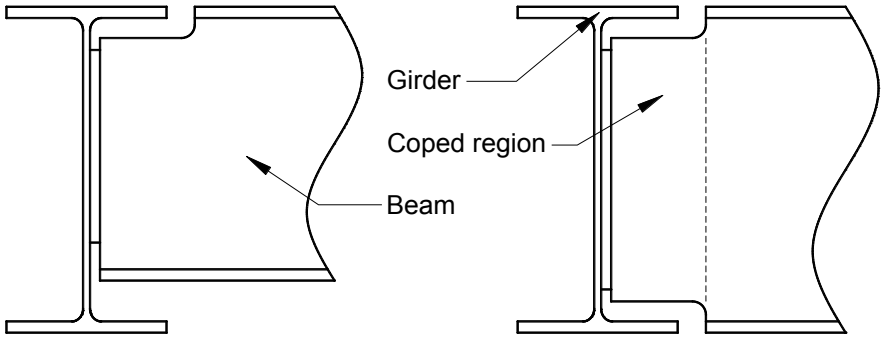

Figure 1-1: Beam coped at (a) top flange only and (b) both flanges

The connection of a coped beam to the support can be made either at the end of the coped region, e.g., with a welded end-plate, or against the web of the coped region, e.g., by bolted or welded angles. The former is more commonly used in industrial construction, and the method used in this research. The end-plate is typically shop welded to the end of the coped region and field bolted to the support. The flexibility of the end-plate, in addition to that of the support, affects the behaviour of the coped

region. Even if the support is considered to be rotationally flexible, the behaviour of the coped beam may be different if the connection is one-sided, i.e., a beam framing into the girder from one side of the girder web only, shown schematically in Figure 1-2(a), or if the connection is symmetric about the girder web, i.e., two beams framing into the girder on opposite sides of the web, shown schematically in Figure 1-2(b). The former case is likely to be used in an end bay, with little or no axial load in the supported beam. Due to the connection asymmetry, gravity loads on the beam will tend to cause twisting of the girder, depending on the torsional stiffness of the girder and the flexibility of its web. The latter case will not exhibit twisting of the girder if the beams have the same span and loading, and even if they have different geometry and loading, some rotational restraint will be still be provided.

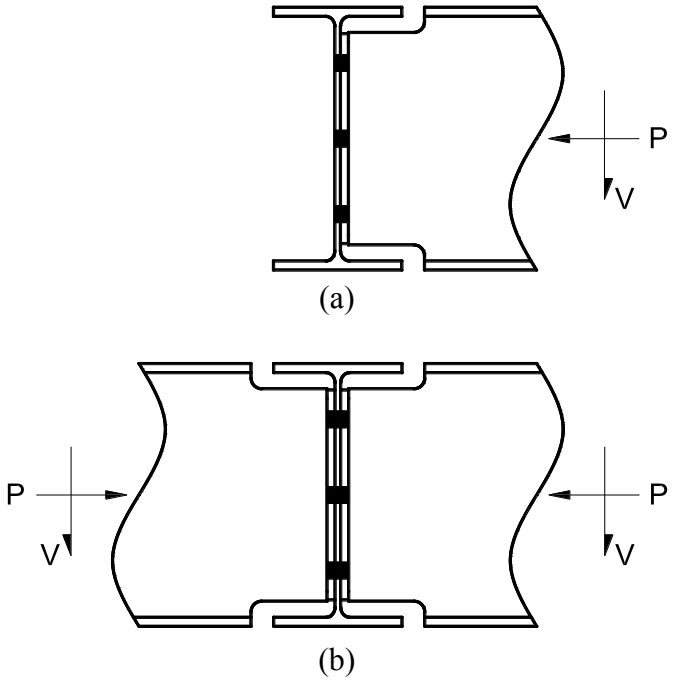

Figure 1-2: Combined loading on (a) one-sided connection and (b) symmetric connection

Structural steel fabricators are commonly required to design shear connections to transfer axial load—compressive or tensile—in addition to shear. Axial loads existing in shear connections could arise from horizontal brace forces or diaphragm forces transferred through the building's lateral load-resisting system. Connections

may also be required to resist axial loads for the purpose of global structural robustness to prevent collapse in extreme load events. Axial forces in symmetric connections are considered to pass through, and so may exist in larger magnitudes compared to the case of a beam on one side only.

The resistance of beams with double-copes under the combined action of bending, shear and axial loads, depends on the strength and lateral–torsional stiffness of the coped region. The global lateral–torsional buckling strength of the beam is greatly reduced due to the removal of the flanges at the connection locations; however, in typical construction practices, structural elements would likely be braced by the floor diaphragm or discrete bracing, so lateral–torsional buckling would be prevented. Even in a braced system, the coped region remains susceptible to local failures. Due to the slenderness of the coped region, the stability of the connection is a concern, especially when subjected to axial compression. If the coped region is very slender, elastic buckling could occur. If local yielding occurs due to the stress concentrations present at the re-entrant corners, or if the coped region yields under shear or bending stresses, inelastic buckling may govern. If the coped region is stocky, a stability-based failure may not occur, and the cross-sectional strength will govern.

Despite their common use, the behaviour of double-coped beams is not well understood due to a lack of research. Very few research programs on the local strength of double-coped beams have been completed, and no published information exists on full-scale physical tests. Connection support conditions, discontinuities, and combined loading create complexity in the stress state of the coped region, and current capacity equations based on elastic stress distributions limited by a first yield criterion often lead to overly conservative and costly connections. Therefore, a research program consisting of full-scale connection tests on double-coped beams is required to better describe the connection behaviour and failure modes, and to assess the validity of currently used design procedures.

1.2 Objectives and Scope

The principal objective of this research is to investigate the local strength and behaviour of a broad variety of double-coped beams by completing full-scale laboratory tests, and in the process create a well-documented database of physical test results. A secondary objective is to study the behaviour of the connections by investigating the failure modes under combined loading—axial and shear—and determining the effect of the test variables on that behaviour. Lastly, the suitability of currently-used design practices will be assessed by comparing test specimen capacities and failure modes to those predicted.

The experimental program included in this research includes 29 full-scale tests on beams coped equally at both the top and bottom flanges. The test beam, braced laterally to isolate the local connection behaviour, was used to load the specimen with shear and axial forces. The geometry of test specimens varied in section depth and cope length, and specimens were subjected to axial loads (tensile or compressive) of various magnitudes. The effects of the end-support rotational stiffness and beam end rotation were also investigated.

1.3 Organization of Chapters

This report is organized into five chapters. Chapter 2 reviews the literature regarding coped beam connections. Design methodologies and equations used in current North American practice are described. The procedures used by a local steel fabricator in the design of double-coped beam connections are also presented. Laboratory testing conducted as part of this research is discussed in Chapter 3. Details of the test specimens—geometry and material properties—are presented, followed by a discussion of the test set-up, instrumentation, and test procedure. A summary and discussion of the test results is presented in Chapter 4. Observed behaviour is discussed, and the critical failure modes are identified and described. The effects of experimental variables on the connection strength and behaviour are compared, and the predicted strengths from four currently-used design procedures are compared to the test capacities. A summary of the research and recommendations for further work are presented in Chapter 5. Appendix A contains

sample calculations for the four design procedures assessed. Material data, including stress–strain curves, can be found in Appendix B, and Appendix C contains load–displacement, moment–displacement, and eccentricity–displacement curves for each test.

CHAPTER 2: LITERATURE REVIEW

2.1 Introduction

Extensive research on steel shear connections has been conducted in the last half-century. However, despite their common use little published research is available on the local behaviour and design of double-coped beam connections subjected to combined axial and shear loads. Consequently, there is no widely accepted limit states design procedure. Elastic stress distribution assumptions, although simple to apply, generally lead to overly conservative connection details.

This chapter reviews the literature on double-coped beam connections to provide context to this research. First, a review of the available literature on shear connection behaviour in general is presented. The relevant research projects on coped-beam connections, which form the basis of the current design guidelines used in North America, are then summarized. Finally, some design methodologies currently used by connection designers for the local stability of double-coped beams, and the associated capacity equations, are shown and discussed.

2.2 Previous Research

2.2.1 Shear Connection Behaviour

Steel connections can be divided into three categories based on their rotational stiffness and bending moment strength: rigid, simple, and semi-rigid. According to Astaneh (1989), rigid connections are those that can develop moments greater than or equal to 90% of that at a fixed support, while the beam end rotation is less than or equal to 10% of the rotation of a pinned support. Similarly, simple connections can develop moments less than or equal to 20% of that at a fixed support, while the beam end rotation is greater than or equal to 80% of the rotation of a pinned support. Between these limits, are semi-rigid connections. Because the limits are based on the relationship between an actual connection and its theoretical counterpart—fixed-end or pin-end—the limits are not absolute, but relative to the bending stiffness of the connected beam.

It is well known that simple connections must satisfy both strength and ductility design criteria; i.e., they require sufficient strength to transfer reaction forces to the support and sufficient ductility to allow the beam end to rotate without failure. The American Institute of Steel Construction *Specification for Structural Steel Buildings*, AISC 360 (AISC 2010) Section B3.6a notes that a simple connection should transfer negligible moment to the supporting element, but have sufficient "…rotation capacity to accommodate the required rotation…" from the supported beam. Section J1.2 states that "…inelastic but self-limiting deformation in the connection is permitted to accommodate the end rotation of a simple beam." It is therefore desirable for shear connections to act as closely as possible to the theoretical case of a pinned support by transferring the beam end shear reaction and developing no moment. In reality, some moment will be developed at the support and its magnitude depends on the rotational stiffness of the connection.

To quantify beam end rotation, Astaneh (1989) proposed a representative shear–rotation relationship, shown in Figure 2-1, based on numerical modelling that investigated nonlinear behaviour of a simply supported beam with a uniformly increasing gravity load.

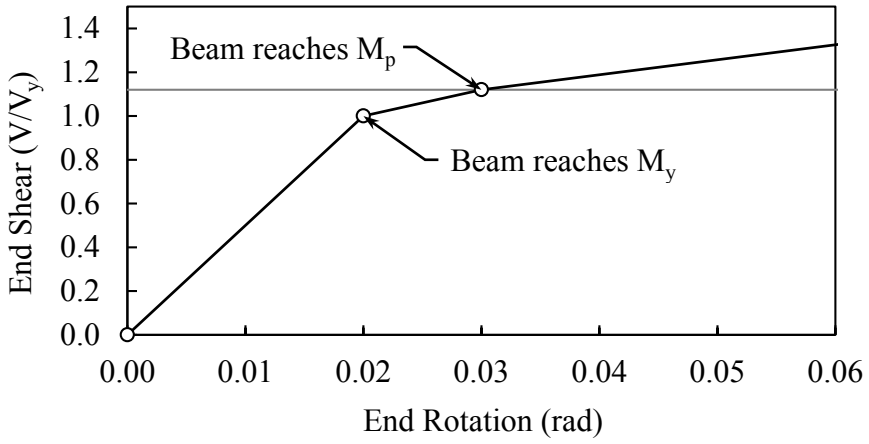

Figure 2-1: Typical shear–rotation behaviour of simple connections

The horizontal axis represents the beam end rotation, and on the vertical axis the beam end shear, V, is normalized by the shear yield capacity, V_y. The shear–rotation relationship is linear and elastic until the point of first yield at a beam end rotation

of 0.02 radians, when the beam reaches its yield moment, M_y, at midspan. Further rotation of the beam end is associated with an inelastic response as a plastic hinge forms at midspan. The model predicts the beam end rotation will reach 0.03 radians once the plastic hinge is fully formed and the beam has reached its plastic moment, M_p. Following this, strain hardening takes place and the beam end rotation could reach up to 0.10 radians, a practical limit consistent with the assumptions of the model. In actual structures, it is likely that local buckling at midspan would limit the vertical load. The shear–rotation relationship proposed by Astaneh (1989) is widely accepted and is commonly used to study shear connection behaviour. Because beams are not typically designed to resist greater than their plastic moment, the beam end rotation of 0.03 radians is considered a reasonable upper limit for testing shear connections.

Beam theory that describes the elastic distribution of normal and shear stresses has been used historically to design connection elements with rectangular cross-sections due to its simple application. The normal and shear stresses due to bending, axial and shear force, are:

$$\sigma = \frac{P}{A} \pm \frac{My}{I} \qquad 2\text{-}1$$

$$\tau = \frac{VQ}{It} \qquad 2\text{-}2$$

where P is the axial force, A is the cross-sectional area, M is the bending moment, y is the distance from the neutral axis to the point of interest, I is the moment of inertia about the axis of bending, V is the shear force, Q is the first moment of area about the neutral axis, and t is the thickness of the element.

When designing a simply supported beam subjected to a uniform gravity load, it is appropriate to neglect the interaction between shear and bending stresses because the points of maximum shear and normal stress are not only at different locations along the beam length, but also act at different locations on the cross-section. When designing connection elements, the interaction of normal and shear stresses must be accounted for because they often occur at the same location along the element

length and interact on the cross-section. Connection elements are regularly subjected to stresses higher than those calculated using traditional stress distributions due to the presence of welds, stress raisers, discontinuities, or local constraints. In-plane restraint may also cause moments to develop at locations of high shear force. Compared to a simply supported beam subject to a uniform gravity load, where shear force and moment are proportional to the applied load, the moment developed in a simple connection is indeterminate and depends on the rotational stiffness of the end-support, even if shear is constant (Astaneh 1989). If the end-support is flexible and the connection is free to rotate, such as the one-sided beam-to-girder connection shown in Figure 1-2(a), the moment at that location may be low or zero, depending on the torsional stiffness of the girder and the flexibility of its web. If the end-support is rigid, which may be the case if two such connections are symmetric about the girder web, as shown in Figure 1-2(b), larger moments could develop. For cases in between, the moment developed at the beam end depends on the stiffness of the end-support. Further complexity in the normal stress distribution of simple connections can occur due to the presence of axial loads, material hardening, residual stresses, and inelasticity, the last of which is generally present locally from early stages of loading (Astaneh 1989).

Normal and shear stress distributions do not match those described by Equations 2-1 and 2-2 for flexural elements with low span-to-depth ratios. Research by Barry and Ainso (1983) and Shawki and Hendry (1961) on simply supported deep beams—beams having a depth and span of the same order of magnitude—showed that stress distributions described by beam theory are only adequate for beams with span-to-depth ratios of 1.5 or greater. Ahmed et al. (1996) investigated deep beams with fixed supports and found that a span-to-depth ratio of 3.0 or greater was required for beam-theory stress distributions to be accurate. Inaccuracy at low span-to-depth ratios is due to the neglected contributions from vertical normal stress induced from applied loads or supports, and shear deformations.

To avoid the need to predict the true stress state, which can be very complex due to local constraints and low span-to-depth ratio, connection elements with rectangular cross-sections have often been designed assuming elastic stress distributions;

however, the resulting designs tend to be overly conservative because the elastic limit underestimates the true strength. Additionally, the calculated normal and shear stresses are assumed to not interact, despite the local effects that act as stress raisers. A plastic strength-based design including the interaction of stresses may be more rational for steel connections with complex stress states.

2.2.2 Coped Beams

Several aspects of coped beam behaviour have been researched over the past 40 years. Research by Cheng et al. (1984) on the local stability of single- and double-coped beams provided the basis for the design procedures in the 14th edition of the AISC *Steel Construction Manual* (AISC 2011). Generally, research on coped beams has focused on the effect of the reduced bending and torsional stiffness, resulting from the removal of one or both flanges, on beam capacity. The region remaining after coping is susceptible to several failure modes, as discussed below.

If the beam is coped at both ends and is laterally unsupported, the resistance to lateral–torsional buckling (LTB) over the beam span is reduced and depends directly on the torsional stiffness of the coped sections. Traditional lateral–torsional buckling formulations assume the beam ends are restrained from lateral and rotational movement, but due to the removal of the flanges at the connection location the beam is highly susceptible to this failure mode. Lateral buckling of coped beams has been studied experimentally by du Plessis (1977) and Cheng et al. (1984; 1988a; 1988b), and numerically by Gupta (1984), Lam et al. (2000), and Maljaars et al. (2005a; 2005b). In typical construction practices, structural elements may be braced by the floor diaphragm or by discrete bracing, and so lateral–torsional buckling would not govern.

The end-support conditions of double-coped beams may differ. Connections to the support can be made either at the end of the coped region, e.g., with an end-plate, or at the web of the coped region, e.g., with welded or bolted angles. In the latter case, the web of the coped region is susceptible to block shear failure. Formulations for the block shear strength of coped beams have been assessed on bolted and welded connections experimentally by Aalberg and Larsen (2000), Franchuk et al.

(2003; 2004), Fang et al. (2013), Yam et al. (2007b) and Wei et al. (2010) and numerically by Topkaya (2007) and Yam et al. (2007c; 2011).

Yam and Cheng (1990) performed full-scale tests and finite element analyses to investigate the fatigue strength of coped beams. They focused on the effect of tension at the free edges of the coped region, which can initiate fatigue cracks at the re-entrant corners if the connection is loaded cyclically. Holden (2012) studied the rehabilitation of fatigue cracking using carbon fibre reinforced polymers.

Yam et al. (2007a; 2011) and Yam and Chung (2013) investigated—both numerically and experimentally—the use of longitudinal or transverse stiffeners or doubler plates to provide local reinforcement to the coped region if the strength is insufficient; however, the AISC *Manual* (AISC 2011) states that the most economical option may be to select a beam with a thicker web. Alternatively, a connection type that is independent of the beam web thickness, such as a shear tab, may be more appropriate than coping.

Yam et al. (2014) summarized the relevant research done on various local failures of coped beams. They note that design approaches for some failures have been relatively well covered, but design guidance on local stability "…seems to lag behind experimental evidence." The local stability of single-coped beams was examined experimentally by Cheng et al. (1984) and Aalberg and Larsen (2001), and numerically by Cheng et al. (1984) and Yam et al. (2003). Local stability of double-coped beams was researched numerically by Cheng et al. (1984), and more recently by Dowswell and Whyte (2014), but has not been studied experimentally.

2.2.3 Design Standards and Guidelines

In CSA Standard S16, *Design of Steel Structures* (CSA 2014), the local stability of beams coped at one or both flanges is not explicitly addressed—it is simply stated that the shear resistance of flexural members without two flanges should be determined "…by rational analysis"—but the shear stress in the cross-section is limited to the shear yield stress. Block shear resistance of coped beams is addressed, but determining the resistance of the beam to lateral–torsional buckling, as well as evaluating the strength and stability of the coped region, is left to the designer.

The Canadian Institute of Steel Construction *Handbook of Steel Construction* (CISC 2012) provides design tables for single-copes; however, no design information is given for double-coped beams. Design strengths of end-plate connections are also given, but the tables provided are restricted to uncoped beams. In a section discussing coped beams, the CISC *Handbook* (CISC 2012) recognizes the susceptibility of beams with copes to local buckling, but the only guidance is to refer to the 13th edition of the AISC *Manual* (AISC 2005).

The predominant design procedure for the local limit states of all coped beams, given in the AISC *Manual* (AISC 2011), is based on determining the flexural strength of the coped region. The moment demand in this region is:

$$M = V \cdot e \tag{2-3}$$

where V is the beam end reaction and e is the geometric eccentricity, defined as the distance from the face of the cope, where stresses for buckling are checked, to the inflection point of the beam. The inflection point is typically assumed to be at the face of the supporting member, following the assumption that no moment is transferred. The available flexural local buckling strength of a coped beam is:

$$M_n = F_{cr} S_{net} \tag{2-4}$$

where F_{cr} is the flexural local buckling stress, and S_{net} is the elastic section modulus of the coped region. For beams coped at one flange only, the net section modulus is associated with the free edge. The notation and assumed normal stress distribution of a double-coped beam are shown schematically in Figure 2-2, where c is the length of the cope, d is the overall beam depth, h_0 is the coped region depth, d_{ct} and d_{cb} are the cope depths at the top and bottom copes, respectively, t_w is the beam web thickness, and the setback is the distance from the end of the coped beam to the support location. The AISC design method, which is based on the research project described in the next section, provides equations to evaluate the critical flexural stress, F_{cr}, at the face of the cope in order to determine the capacity of the connection.

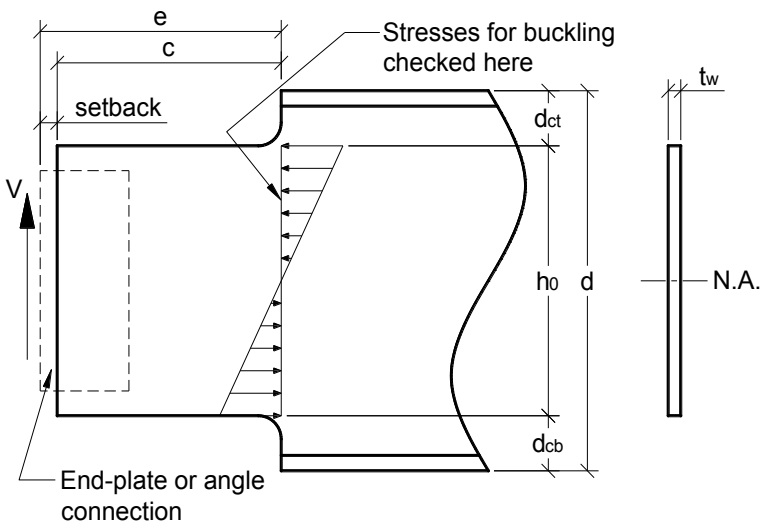

Figure 2-2: Double-coped beam notation and assumed normal stress distribution (after AISC 2011)

2.2.4 Cheng et al. (1984)

Cheng et al. (1984) studied the effect of coping beams with various connection geometries using two methods: finite element analysis and physical testing. Design models and recommendations were made based on results for the different geometric situations investigated: connections coped at the top flange only and connections coped at both flanges. Sixteen full-scale tests were completed to validate the finite element analysis results and perform a reliability analysis on the proposed design recommendations, which showed the equations give conservative and reasonable results. Six tests were used to consider lateral–torsional buckling over the beam span, and the remaining ten tests were used to consider local web buckling at the coped region.

Cheng et al. (1984) noted that special attention must be given by connection designers to the coped region due to the strength and torsional stiffness reductions, which can lead to local failures such as yielding from shear and bending stresses, or local web buckling. The authors also predicted that stress concentrations at the re-entrant corners would invalidate Equations 2-1 and 2-2 for the normal and shear stress distributions at the face of the cope. At the time, design standards only recommended checking the coped region for yielding under shear force and

moment, but neglected any effect from the stress concentration. The interaction of normal and shear stresses was also not considered. As such, the design assumptions produced a very conservative solution and did not address local stability. The main objectives of the research described below were to investigate the behaviour of coped beams and provide practical design recommendations for local web buckling.

2.2.4.1 Single-coped Beams

Cheng et al. (1984) used finite element analysis to consider a plate buckling model for the design of beams coped at the top—compression—flange only, which was then verified experimentally. For practical purposes, coped-beam models were limited to cope lengths less than two times the beam depth ($c \leq 2d$) and cope depths less than half of the beam depth ($d_c \leq d/2$). Because the finite element models were created to investigate local effects only, a short cantilever was used—free to move vertically at the coped end and fixed at the uncoped end. Lateral displacement was prevented at the coped end and at the top flange at the face of the cope. A vertical load was applied at the free end and increased until buckling took place.

Elastic local web buckling was studied on a W410×39 (W16×26) beam with a 38.1 mm (1.5 in) cope depth for three cope lengths: 203.2 mm (8 in), 406.4 mm (16 in) and 812.8 mm (32 in). Cheng et al. (1984) found that a classical plate buckling model with one free edge, three simply supported edges, and a triangular normal stress distribution, shown schematically in Figure 2-3, was appropriate for the design model because it resulted in similar deformed shapes to the finite element analyses.

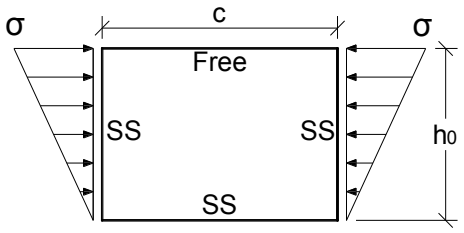

Figure 2-3: Plate buckling model

To increase the accuracy of the design model, the authors used an adjustment factor to account for variables not captured by classical theory. The classical plate buckling equation for the critical normal stress is:

$$\sigma_{cr} = k\frac{\pi^2 E}{12(1-\nu^2)}\left(\frac{t_w}{h_0}\right)^2 \qquad 2\text{-}5$$

where E is the elastic modulus, ν is Poisson's ratio, and k is the plate buckling coefficient found by curve-fitting to the finite element solutions a function of the cope-length-to-reduced-beam-depth ratio (c/h_0):

for $\frac{c}{h_0} \leq 1.0$: $$k = 2.2\left(\frac{h_0}{c}\right)^{1.65} \qquad 2\text{-}6$$

for $\frac{c}{h_0} > 1.0$: $$k = 2.2\left(\frac{h_0}{c}\right) \qquad 2\text{-}7$$

In comparing elastic bending stresses from the finite element models to the theoretical normal stresses, the authors found that the stress concentration at the re-entrant corner resulted in stresses significantly greater in magnitude than the theoretical stresses when the cope length is short; however, this effect decreased as the cope length increased. Additionally, the area of the concentrated stress region for models with long copes was less than that for models with short cope lengths. The effect of shear stress was also found to decrease as the cope length increased, noted by observing the buckling line that tended to be more vertical for longer copes, deviating away from the 45° angle associated with pure shear buckling.

Cope depth was found to have a larger effect on models with short copes, as those models produced larger lateral displacements near the re-entrant corner. However, upon further analysis it was concluded that generally the cope depth has relatively little effect on the nominal buckling stress. Finite element models showed that increasing the cope depth from 38.1 mm (1.5 in) to 190.5 mm (7.5 in) reduced the critical buckling stress for a plate with a web thickness of 6.4 mm (¼ in) by 4% and 17% for $c/h_0 = 2$ and $c/h_0 = 1$, respectively.

To investigate the effect of inelasticity on the connection behaviour, a W250×33 (W10×22) beam model with 38.1 mm (1.5 in) cope depth, 228.6 mm (9 in) cope length and 345 MPa (50 ksi) yield strength was analyzed. The critical end reaction was found to be 68% lower than the critical elastic load, indicating a large effect due to inelasticity at the re-entrant corner. The authors found that local yielding reduced the stress concentration and forced the normal stress distribution closer to the elastic distribution. Continuing the study to other geometries, it was found that the critical load for either pure bending or pure shear using first yield as the limit state always produced a lower bound compared to the inelastic buckling capacity.

Accounting for the effects of stress concentration at the re-entrant corners, shear stress, cope depth, and the moment distribution from the cope face to the supporting element, a single adjustment factor, f, was proposed that depends on the cope-length-to-beam-depth ratio (c/d):

for $\frac{c}{d} \leq 1.0$: $$f = \frac{2c}{d} \qquad 2\text{-}8$$

for $\frac{c}{d} > 1.0$: $$f = 1 + \frac{c}{d} \qquad 2\text{-}9$$

Including the adjustment factor, Equation 2-5 for the critical buckling stress becomes:

$$F_{cr} = k\frac{\pi^2 E}{12(1-\nu^2)}\left(\frac{t_w}{h_0}\right)^2 f \leq F_y \qquad 2\text{-}10$$

which is limited to F_y, the nominal flexural yield stress of the beam. Cheng et al. (1984) also investigated the reliability of Equations 2-8 to 2-10 by comparing them to a series of elastic finite element models with varying cope length and cope-depth-to-beam-depth ratios (d_c/d), and found the equations give close results but tend to be very conservative for shallow copes; e.g., the proposed design model underestimates the buckling capacity by 20% for connections with $d_c/d = 0.10$.

Of the ten connection tests performed on single-coped beams to assess the proposed local design procedure, five test specimens were designed to fail by inelastic local

web buckling following either shear or flexural yielding and were also used to study the effects of end restraint, and five were designed to fail by elastic local web buckling. The main test variables were: cope length, cope depth, and the ratio c/d. The end-support used for all tests was a stub column, and the connections were either welded clip angles or an end-plate. In–plane restraint was minimized for four tests by using an end-plate bolt gauge 45% greater than that of the other end-plates, and by placing washers between the end-plate and the supporting column. Out-of-plane bracing was provided at discrete locations along the beam length, and at the end of the cope.

Of the five specimens designed to fail inelastically, the two that were designed to fail by shear yielding—which differed only in cope length: 88.9 mm (3.5 in) and 165.1 mm (6.5 in)—resulted in tested capacities within 5% of the load predicted by shear yielding. The specimen with the greater cope length had a buckling capacity 3% lower than the specimen with the shorter cope length. Both of the specimens benefitted from the out-of-plane restraint provided by welded clip angles, which also altered the normal stress distribution from the theoretical. The three test specimens designed to fail by flexural yielding were also used to evaluate the effects of end-support conditions. The two specimens with high in-plane restraint had test capacities 17% and 28% greater than that predicted by the bending stress yield criterion because moment that developed at the support reduced the moment, and therefore the normal stresses, at the face of the cope. Out-of-plane restraint provided by the clip angles also resisted out-of-plane displacement and delayed buckling. In comparison, the test specimen with reduced in-plane restraint (end-plate connection) failed at a load only 7% greater than that predicted by the flexural yield stress criterion. Nonlinear load–displacement responses for the five inelastic buckling tests provided evidence of yielding prior to buckling.

Of the five specimens designed to fail by elastic local web buckling, three were rolled W-shapes and two were built-up plate girders. The load–displacement responses for the test specimens made from W-shapes were linear until the buckling load, followed by a sudden decrease in strength, which indicates a purely elastic response. The capacity predicted by Equations 2-8 to 2-10 was conservative by 32

to 39% for the three tests. The two plate girder test specimens, which differed only in their cope lengths, had nonlinear load–displacement relationships due to initial out-of-straightness of the thin girder web. The proposed local web buckling equation gave capacities 34% and 108% conservative for specimens with cope lengths equal to 203.2 mm (8 in) and 330.2 mm (13 in), respectively. The very conservative results for these tests were partly due to the conservatism in the design model, but mainly due to the normal stress distribution that was significantly different than the assumed distribution because the values of c/d for the test specimens were low: 0.3 and 0.49. The buckled shapes showed a combination of buckling modes, including effects from both shear and local web buckling. After reaching the shear buckling capacity, a tension field developed that provided significant post–buckling strength.

2.2.4.2 Double-coped Beams

Finite element models using a similar cantilever format were used to study beams coped at both flanges. Coped-beam models were limited to $c \leq 2d$, as for single-coped beams, and cope depths less than one-fifth of the beam depth ($d_c \leq d/5$). Because the elastic normal and shear stress distributions were always found to provide a lower bound to the inelastic buckling loads for single-coped beams, inelastic local web buckling was not investigated for double-coped beams.

The three models used to study elastic local web buckling on beams coped at both flanges were similar to those used for single-coped beams: a W410×39 (W16×26) beam with a 38.1 mm (1.5 in) cope depth at the top and bottom flanges in three cope lengths—203.2 mm (8 in), 406.4 mm (16 in) and 812.8 mm (32 in). The design model for double-coped beams was based on lateral–torsional buckling of a rectangular beam with a span of length c because it produced similar deformed shapes to the finite element analyses: lateral displacement and twisting of the cross-section. The moment distribution was assumed to be linear along the laterally unsupported coped region: maximum at the cope face and zero at the support, as shown schematically in Figure 2-4. The top and bottom edges are free, and the remaining edges are restrained from out-of-plane displacement but not rotation.

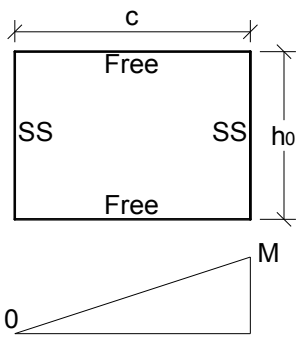

Figure 2-4: Lateral–torsional buckling model

According to this design model, double-coped beams with slender cross-sections and large cope lengths can fail by lateral–torsional buckling before yielding. The elastic lateral–torsional buckling strength of a simply supported beam with a rectangular cross-section under strong axis bending is:

$$M_{cr} = C_b \left(\frac{\pi}{k_d c}\right) \sqrt{EI_y GJ} \qquad 2\text{-}11$$

where C_b is the moment gradient coefficient, k_d is an effective length factor for the restraint conditions at the ends of the coped region, c is the span length—in this case the cope length—I_y is the moment of inertia about the weak axis, G is the shear modulus, and J is the St. Venant torsional constant. Warping torsion is neglected for a thin rectangular member.

Cheng et al. (1984) noted the ratio of C_b/k_d was nearly constant for the three models and concluded that the effects of stress concentrations at the re-entrant corners, shear stress, cope depth, and in-plane restraint do not change for different cope lengths and could therefore be represented by a single adjustment factor, f_d. Including the moment gradient coefficient in the adjustment factor changes Equation 2-11 to:

$$M_{cr} = f_d \left(\frac{\pi}{c}\right) \sqrt{EI_y GJ} \qquad 2\text{-}12$$

Equation 2-12 can be further simplified by substituting in the formulations for a rectangular cross-section as follows:

$$I_y = \frac{1}{12} h_0 t_w^3 \qquad 2\text{-}13$$

$$J = \frac{1}{3} h_0 t_w^3 = 4I_y \qquad 2\text{-}14$$

$$G = \frac{E}{2(1+\nu)} = \frac{E}{2.6} \qquad 2\text{-}15$$

where Poisson's ratio is 0.3 for steel. The result expressed in terms of the critical buckling stress, F_{cr}, is limited to the flexural yield stress, as follows:

$$F_{cr} = 0.62\pi E \frac{t_w^2}{ch_0} f_d \le F_y \qquad 2\text{-}16$$

where the adjustment factor, f_d, is calculated as:

$$f_d = 3.5 - 7.5\left(\frac{d_{ct}}{d}\right) \qquad 2\text{-}17$$

Equation 2-17 was developed from finite element models of a W410×39 (W16×26) beam with a constant cope length of 203.2 mm (8 in) and equal cope depths up to 0.2 of the beam depth. The numerical results were compared to Equation 2-16 as a function of the top flange cope-depth-to-beam-depth ratio (d_{ct}/d) and a linear expression was fit to the results. To verify the reliability of Equations 2-16 and 2-17, further analyses were done on finite element models with the three cope lengths described previously, a web thickness of 2.54 mm (0.10 in), and various cope depths. The results were compared and the proposed design equations were found to be reasonable and conservative. No physical tests were completed on double-coped beams.

To determine when the critical buckling stress given by Equation 2-16 is limited by yielding, the results are plotted in Figure 2-5 against c/d for different beam-depth-to-web-thickness ratios (d/t_w) at $d_{ct}/d = 0.1$. Because most rolled W-shapes have $d/t_w < 60$, the cope length must be greater than the beam depth in order for local buckling to control any rolled W-shape with $F_y = 350$ MPa.

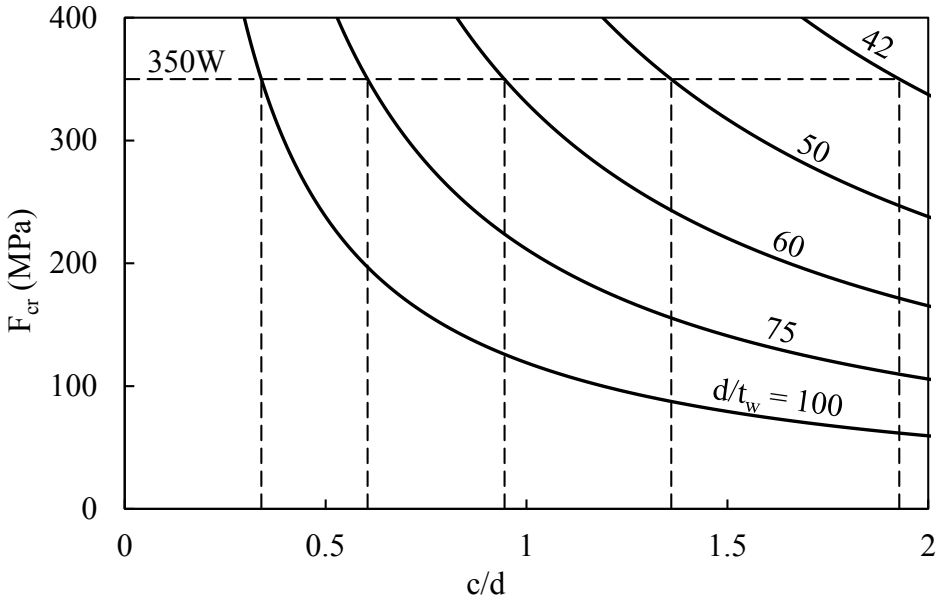

Figure 2-5: Buckling strength of double-coped beams with $d_{ct}/d = 0.1$ (after Cheng et al. 1984)

Sections with d/t_w significantly less than 60 require very long copes, relative to the section depth, for local buckling predicted by Equation 2-16 to govern. If the cope length is approximately twice the section depth, and $d/t_w < 42$, buckling will not govern if the yield strength is less than 350 MPa. For built-up sections such as plate girders with $60 < d/t_w < 100$, local web buckling is more likely to occur, even if the cope length is short compared to the section depth.

The design methods described by Equations 2-8 to 2-10 for single-coped beams and Equations 2-16 to 2-17 for double-coped beams were subsequently published by Cheng and Yura (1986) and are currently included in the AISC *Manual* (AISC 2011). To use either method, the cope length is restricted to less than or equal to two times the beam depth ($c \leq 2d$), and the limits of applicability on the cope depths for beams coped at the top flange only and for beams coped at both flanges are $d_c \leq d/2$ and $d_c \leq d/5$, respectively. In both procedures, the critical stress is limited to the yield strength of the beam web, and neither accounts for the presence of axial load. For cases not within the defined geometric limits, the AISC *Manual* (AISC 2011) gives a procedure based on the classical plate buckling equation, which is described in Section 2.3.2.1.

2.2.5 Dowswell and Whyte (2014)

Dowswell and Whyte (2014) further explored the problem of local stability on double-coped beams and proposed a new design approach based on coped region's strength and stability. The method also extends the limits of applicability imposed on the design equations by Cheng and Yura (1986). The design method is based on Section F11 of the AISC *Specification* (AISC 2010) that provides a design procedure for rectangular bars bent about their major axis (at the time of writing, it is expected that this method will be unchanged in the 2016 edition of the *Specification*). The procedure is outlined below.

The failure mode of the section—yielding, inelastic lateral–torsional buckling, or elastic lateral–torsional buckling—is first predicted through a nondimensional slenderness parameter, $L_b d/t^2$:

for yielding:

$$\frac{L_b d}{t^2} \leq \frac{0.08E}{F_y} \qquad 2\text{-}18$$

for inelastic lateral–torsional buckling:

$$\frac{0.08E}{F_y} < \frac{L_b d}{t^2} \leq \frac{1.9E}{F_y} \qquad 2\text{-}19$$

for elastic lateral–torsional buckling:

$$\frac{L_b d}{t^2} > \frac{1.9E}{F_y} \qquad 2\text{-}20$$

where L_b is the distance between brace points—equal to the cope length, c—d is the rectangular 'beam' depth—equal to the reduced beam depth, h_0—and t is the beam width—in this case the beam web thickness, t_w. The resulting nominal flexural strength, M_n, is:

for yielding:

$$M_n = M_p = F_y Z \leq 1.6 M_y \qquad 2\text{-}21$$

for inelastic lateral–torsional buckling:

$$M_n = C_b \left[1.52 - 0.274 \left(\frac{L_b d}{t^2}\right) \frac{F_y}{E}\right] M_y \leq M_p \qquad 2\text{-}22$$

for elastic lateral–torsional buckling:

$$M_n = F_{cr} S_x \leq M_p \qquad 2\text{-}23$$

and the critical buckling stress is:

$$F_{cr} = \frac{1.9EC_b}{\frac{L_b d}{t^2}} \qquad 2\text{-}24$$

where C_b is the lateral–torsional buckling modification factor for nonuniform moment discussed in Section F1 of the AISC *Specification* (AISC 2010), M_y and M_p are the yield and plastic moments, respectively, and S_x and Z are the elastic and plastic section moduli, respectively. Equation 2-24 is a theoretical lateral–torsional buckling formula equivalent to Equation 2-12 and therefore Equation 2-16 when $C_b = f_d$, $t = t_w$, and $L_b = c$.

Dowswell and Whyte (2014) conducted a parametric study on 54 elastic finite element models of double-coped beams to address three geometric cases related to local stability that extend beyond the limits imposed by Cheng et al. (1984):

1) cope depths greater than 20% of the beam depth;
2) unequal cope depths at the top and bottom; and
3) unequal cope lengths at the top and bottom.

Of the 54 models studied, 30 had equal cope lengths at the top and bottom, in 12 the top cope length was greater than the bottom, and in the remaining 12 the bottom cope length was greater than the top. The models were created using the same W410×39 (W16×26) beam used in the research by Cheng et al. (1984). Models analyzed had cope lengths between 195 mm and 780 mm and cope depths varying between 43.4 mm and 160.3 mm. All models were braced laterally at the face of the cope.

Of the geometries that fell within the limitations imposed by the equations in the AISC *Manual* (AISC 2011), Dowswell and Whyte (2014) found an average ratio of the critical load from the finite element models to that from the AISC equations of 1.54, with a coefficient of variation of 32%, which is notably conservative considering all models remained in the elastic range.

The buckling modes observed in the parametric study by Dowswell and Whyte (2014) were similar to those seen by Cheng et al. (1984): lateral translation and twisting at the shear centre, and lateral translation only at the tension edge. The compression edge buckled in the shape of a half sine wave, and buckling extended partially into the uncoped web. The buckled shapes showed several independent buckling modes including local buckling, lateral–torsional buckling, shear buckling, and distortional buckling; however, lateral–torsional buckling was selected as the basis for the design model because the buckled shapes most closely resembled this buckling mode over the range of variables tested. A lateral–torsional buckling factor, C_b, was proposed to account for the effect of other buckling modes, derived by curve-fitting the finite element data.

For beams with equal cope lengths, or those with the top cope length shorter than the bottom, the following was proposed for the new lateral–torsional buckling factor:

$$C_b = \left[3 + \ln\left(\frac{L_b}{d}\right)\right]\left(1 - \frac{d_{ct}}{d}\right) \geq 1.84 \qquad 2\text{-}25$$

where L_b is taken as the top cope length. For beams with the top cope length longer than the bottom, the following was proposed:

$$C_b = \left(\frac{c_b}{c_t}\right)\left[3 + \ln\left(\frac{L_b}{d}\right)\right]\left(1 - \frac{d_{ct}}{d}\right) \geq 1.84 \qquad 2\text{-}26$$

where L_b is the average of the top and bottom cope lengths, c_t and c_b, respectively. Both equations are limited to a minimum of 1.84, a value developed by Dowswell (2004) for a rectangular beam loaded at the shear center to account for different behaviour when the cope length is small compared to the coped region height.

When the cope length is less than half of the beam depth, the behaviour is dominated by shear buckling and the values of C_b would be unrealistically low if they were not limited.

The following design procedure was proposed based on the inelastic procedure in the AISC *Specification* (AISC 2010):

for yielding, $\lambda \leq \lambda_p$:

$$M_n = M_p \tag{2-27}$$

for inelastic lateral–torsional buckling, $\lambda_p < \lambda \leq \lambda_r$:

$$M_n = C_b \left[1.52 - 0.274\lambda \frac{F_y}{E}\right] M_y \leq M_p \tag{2-28}$$

for elastic lateral–torsional buckling, $\lambda > \lambda_r$:

$$M_n = F_{cr} S_x \leq M_p \tag{2-29}$$

where C_b is calculated by Equation 2-25 or 2-26, depending on the geometry of the connection. The critical stress is:

$$F_{cr} = \frac{1.9EC_b}{\lambda} \tag{2-30}$$

where the slenderness parameter, λ, and slenderness limits, λ_p and λ_r, are:

$$\lambda = \frac{L_b h_0}{t_w^2} \tag{2-31}$$

$$\lambda_p = \frac{0.08E}{F_y} \tag{2-32}$$

$$\lambda_r = \frac{1.9E}{F_y} \tag{2-33}$$

For all predicted failure modes, the nominal design moment, M_n, is limited to the plastic moment capacity of the cross-section, M_p. Because Dowswell and Whyte's (2014) proposed calculation of C_b in Equations 2-25 and 2-26 uses the method

outlined in the AISC *Specification* (AISC 2010)—which relies on a strength-based design methodology—the plastic strength of the cross-section must be accounted for, including the interaction between bending and shear stresses.

Neal (1961) derived a lower bound equation to account for the interaction of normal and shear stresses on the plastic moment of a beam with a rectangular cross-section. The derivation is based on a cantilever model subject to a transverse shear force and normal force at the free end. The interaction equation is:

$$\frac{M}{M_p} + \left(\frac{P}{P_y}\right)^2 + \frac{\left(\frac{V}{V_p}\right)^4}{1 - \left(\frac{P}{P_y}\right)^2} \leq 1.0 \qquad 2\text{-}34$$

where M, P, and V are the moment, axial and shear forces applied to the cross-section, respectively, M_p is the plastic moment due to bending only, P_y is the axial yield force, and V_p is the plastic shear strength. If the cross-section is not subject to axial force, Equation 2-34 simplifies to:

$$\frac{M}{M_p} + \left(\frac{V}{V_p}\right)^4 \leq 1.0 \qquad 2\text{-}35$$

Dowswell and Whyte (2014) suggest the designer use Equation 2-35 to calculate the reduced plastic moment that can be used for the strength limit in Equations 2-27 to 2-29. For short copes dominated by shear behaviour, the required shear load, V, may approach the plastic shear strength, and the plastic moment may be significantly reduced.

The equations proposed for C_b by Dowswell and Whyte (2014) are only valid for $d_{ct} \leq 0.4d$, based on the geometry chosen for the finite element models studied. For the 30 models analyzed with equal cope lengths at the top and bottom flanges ($c_t = c_b$), the average ratio of the critical load from the finite element models to that from the proposed design method is 1.18, with a coefficient of variation of 12%.

2.3 Capacity Equations

Several capacity equations are widely accepted for use in the design of shear connections. Equations relevant to the resistance of double-coped beam connections include calculations for: gross section yielding, out-of-plane displacement, local web buckling, axial load and bending interaction, and end-plate resistance, as described in the sections below.

2.3.1 Cross-sectional Strength

If the coped region is sufficiently robust to resist a stability failure, the cross-sectional capacity will be governed by the material strength. The cross-sectional strength may be reached under tensile or shear loads, bending, or through the interaction of all three effects.

Section yielding is a ductile failure mode associated with yielding over the entire depth of the cross-section. Because the removal of the flanges typically reduces the cross-sectional area by 50% or more, yielding must be checked. The resistance of the net section under tensile load is:

$$T_r = AF_y = h_0 t_w F_y \qquad 2\text{-}36$$

where A is the area under tension, in this case the cross-sectional area of the coped region. The shear resistance assuming an elastic stress distribution can be calculated by rearranging Equation 2-2 and using the von Mises yield criterion for pure shear:

$$V_y = \frac{0.577AF_y}{1.5} = \frac{0.577h_0 t_w F_y}{1.5} \qquad 2\text{-}37$$

If the shear stress distribution is assumed to be plastic, the shear resistance is:

$$V_p = 0.577h_0 t_w F_y \qquad 2\text{-}38$$

To account for the effect of strain hardening, design standards commonly increase the 0.577 shear coefficient; CSA Standard S16 (CSA 2014) and the AISC *Specification* (AISC 2010) use values of 0.66 and 0.6, respectively. Under bending

about the strong axis, the moment at which the extreme fibre of a rectangular cross-section begins to yield, known as the yield moment, is:

$$M_y = \frac{h_0^2 t_w F_y}{6} \qquad 2\text{-}39$$

The moment at which the entire rectangular cross-section has yielded, known as the plastic moment, is:

$$M_p = \frac{h_0^2 t_w F_y}{4} \qquad 2\text{-}40$$

Neal (1961) first proposed a strength interaction relationship (Equation 2-34), accounting for the combined effects of bending, shear and axial loads, and later (Neal 1977) noted the rarity in which the combined effects of shear and axial force "…will be of sufficient magnitude to have an appreciable effect on the fully plastic moment." However, for beams with short cope lengths, the required shear load may approach the plastic shear strength, which can reduce the plastic moment significantly.

Astaneh (1998) proposed a modified equation for the seismic design of gusset plates when a rectangular cross-section is subjected to the combined effects of moment, shear and axial forces. The interaction equation suggested was:

$$\frac{M}{M_p} + \left(\frac{P}{P_y}\right)^2 + \left(\frac{V}{V_p}\right)^4 \leq 1.0 \qquad 2\text{-}41$$

2.3.2 Local Stability

Stability-based failures of slender coped regions may occur prior to the cross-section reaching its yield or plastic moment under bending or its resistance under pure shear. Because current design standards do not give adequate guidance on the stability of double-coped beams—especially under compressive loads—designers often assume behaviour based on design equations for other structural elements.

2.3.2.1 Classical Plate Buckling

For coped beams that fall outside the geometric bounds of the current equations in the AISC *Manual* (AISC 2011), a conservative procedure based on the classical plate buckling equation is given. Muir and Thornton (2004) simplified the procedure to determine the associated plate buckling coefficient for the case of one free and three simply supported edges under uniform compression based on buckling curves presented by Gerard and Becker (1957). The buckling stress is:

$$F_{cr} = Q\, F_y \qquad 2\text{-}42$$

This procedure accounts for both elastic and inelastic buckling through the factor Q, which depends on the slenderness parameter, λ, as shown in the procedure below:

for $\lambda \leq 0.7$: $$Q = 1 \qquad 2\text{-}43$$

for $0.7 < \lambda \leq 1.41$: $$Q = 1.34 - 0.486\lambda \qquad 2\text{-}44$$

for $\lambda > 1.41$: $$Q = \frac{1.30}{\lambda^2} \qquad 2\text{-}45$$

$$\lambda = \frac{h_0\sqrt{F_y}}{10t_w\sqrt{475 + 280\left(\frac{h_0}{c}\right)^2}} \qquad 2\text{-}46$$

where F_y is the minimum specified yield stress in kips/inch^2.

2.3.2.2 Elastic Lateral–Torsional Buckling

The elastic lateral–torsional buckling resistance of a rectangular cross-section is discussed in Section 2.2.4.2 and shown Equation 2-11. The moment gradient coefficient, C_b, was included in the adjustment factor, f_d, proposed by Cheng et al. (1984) and therefore its effect is somewhat unclear. Because there are no intermediate shear loads acting on the coped region of a double-coped beam, it may be appropriate to use a linear moment distribution between the cope face and the support. One method to account for the increased moment resistance when subject

to a moment gradient is provided in S16 (CSA 2014) by including the ω_2 factor, which is calculated as:

$$\omega_2 = 1.75 + 1.05\kappa + 0.3\kappa^2 \leq 2.5 \qquad 2\text{-}47$$

where κ is the ratio of the smaller to the larger moment at the ends of the unbraced segment—positive for double curvature and negative for single curvature. Applying the ω_2 coefficient to Equation 2-11 and assuming $k_d = 1.0$, implying that the sections at the face of the cope and at the weld to the end-plate do not provide restraint against rotation about the vertical axis, gives the elastic lateral–torsional buckling strength of a beam with a rectangular cross-section and span equal to c subject to a linear moment gradient:

$$M_u = \frac{\omega_2 \pi}{c} \sqrt{EI_y GJ} \qquad 2\text{-}48$$

Because elastic lateral–torsional buckling gives little warning prior to failure, and is generally followed by low post-buckling strength, it is considered a brittle failure mode that should be avoided. To prevent elastic lateral–torsional buckling of the coped region, a minimum web thickness can be determined by equating the lateral–torsional buckling moment from Equation 2-48 to the yield moment of the coped region given in Equation 2-39, and solving for the web thickness using the properties of a rectangular cross-section shown in Equations 2-13 to 2-15. To avoid elastic lateral–torsional buckling at the coped region and ensure yielding will take place, the web thickness of the beam should be greater than:

$$t_{w,min} = 0.716 \sqrt{\frac{ch_0}{\omega_2} \frac{F_y}{E}} \qquad 2\text{-}49$$

2.3.2.3 Column-style Buckling

It is not uncommon for shear connections to resist compressive load in addition to shear. If the coped region of a double-coped beam is subjected to a compressive

force, a column-style buckling failure could be considered. The resistance of a doubly symmetric shape to a column-style failure, C_r, is given by (CSA 2014):

$$C_r = AF_y\left(1 + \lambda^{2n}\right)^{-1/n} \quad 2\text{-}50$$

where n is taken as 1.34 for hot-rolled structural sections, and λ is a nondimensional slenderness parameter given by:

$$\lambda = \frac{KL}{r}\sqrt{\frac{F_y}{\pi^2 E}} \quad 2\text{-}51$$

where K is the effective length factor for column bucking, taken as 1.0 for pinned supports at both ends, L is the unbraced length, taken as the cope length for this case, and r is the least radius of gyration, associated with weak-axis buckling of the coped region.

2.3.2.4 Beam-column Interaction

Connection designers may choose to consider the coped region as a beam-column in order to account for stability effects associated with the interaction of bending and compressive force. Because the procedure for the design of a beam-column is lengthy and described in detail in other sources (CSA 2014), it is not shown here. Although beam-column capacity equations do not require the member to remain elastic, they tend to be inaccurate at low span-to-depth ratios and, as such, the applicability of these equations for the coped region of a double-coped beam is largely unknown, and likely overly conservative.

2.3.3 End-plate Resistance

In the design of welded end-plates subjected to shear and tensile loads, designers may consider failure modes associated with the weld strength under combined loads, bolt bearing or bolt shear failures including prying effects, or block shear over the end-plate bolt pattern. Because the phenomena associated with these components and failure modes are relatively well understood and covered in design standards, they will not be discussed herein.

2.4 Summary

Many research projects have been completed on aspects of coped beams, including elastic and inelastic behaviour of single-coped beams, lateral–torsional buckling of beams coped at both ends, block shear of connections made at the beam web, local reinforcement, and fatigue strength and repair; however, little research has been published on double-coped beam behaviour, despite their common use, and no published information exists on the full-scale testing of double-coped beams. Research completed by Cheng et al. (1984) was used in the development of the current design procedure in the AISC *Manual* (AISC 2011). However, the design method specific to beams coped at both flanges neglects inelastic effects and gives very conservative results for short cope lengths and shallow cope depths. More recent research by Dowswell and Whyte (2014) has proposed revisions to the lateral–torsional buckling modification factor included in the procedure for the design of rectangular beams in the AISC *Specification* (AISC 2010). Neither of these procedures addresses the effect of the presence of axial load on the stability of the coped region.

Other failures modes of shear connections have been investigated previously and may be applicable to the design of double-coped beams such as: cross-sectional strength including the effect of combined bending, axial and shear, coped region stability such as plate buckling, column style buckling, or elastic lateral–torsional buckling, or the interaction of shear and normal stresses on the cross-sectional strength. However, because the effect of axial load has not been explicitly considered by design standards in assessing the local stability of double-coped beams, connection designers are left to select the limit states they deem most appropriate, which often leads to overly conservative connections.

CHAPTER 3: EXPERIMENTAL PROGRAM

3.1 Introduction

A total of 29 full-scale tests were completed to investigate the behaviour of double-coped beam connections subjected to combined vertical and horizontal loads. Primary objectives of the testing program were to contribute test data to the knowledge base, determine the effect of key variables, and assess currently-used design procedures. In addition to the magnitude and direction (tensile or compressive) of axial loads, the testing program investigated the influence of beam section, cope length, end-support conditions, and end rotation on the behaviour of double-coped beams.

In this chapter, a discussion of the experimental program for this research is presented. First, the selection of test variables and test specimen geometry are discussed. The methodology used to design the specimens, as-built dimensions, and material properties are then summarized. Finally, the test set-up, instrumentation, and testing procedures are discussed.

3.2 Test Specimens

3.2.1 Selection of Test Variables

Local geometric parameters of double-coped beams—the reduced beam depth, cope length, and web thickness—are critical to the stability of the coped region. To investigate the effect of stability, the cope length and beam section were chosen as test variables, while the nominal cope depth at both flanges was kept constant. In practice, steel connection designers commonly select the shallowest cope depth possible, while maintaining clearance to the support, to avoid large capacity reductions in the connection. By varying the beam section and maintaining a constant cope depth, the combined effects of web thickness and reduced beam depth are captured in the test results. Three beam sections were used: W200×27, W310×33, and W410×54, which represent a typical range of sections suitable for double-coped connections. Beam sections with thicker webs—robust enough to

resist stability failures—tend to be governed by shear or flexural yielding failure modes. The three beam sections chosen have relatively thin webs, so an instability failure is more likely to occur before the cross-section has fully yielded.

The strength of the coped region has been shown previously to depend on the length of the cope; however, the behaviour depends more on the cope-length-to-reduced-beam-depth ratio. Cheng et al. (1984) found that shear capacities for beams with longer cope lengths are less than beams with shorter cope lengths, and that beams with greater c/h_0 ratios tended to be controlled by bending behaviour, and beams with lower c/h_0 ratios were controlled by shear behaviour. The three double-coped beam finite element models analyzed by Cheng et al. (1984) had c/h_0 ratios of 0.63, 1.26, and 2.52, and the 30 numerical models investigated by Dowswell and Whyte (2014) had c/h_0 ratios varying between 0.83 and 4.99, including three with $c/h_0 \leq 1.0$. In neither research project were models with very low c/h_0 ratios studied.

Similar to the cope depth, designers commonly detail copes at the minimum required length, i.e., the smallest length such that the flange of the beam does not interfere with the girder flange, to avoid large capacity reductions caused by stability limit states. From the face of the girder web, or end-plate if applicable, the minimum cope length required is the distance to the girder flange tip plus an appropriate clearance that may include fire protection. Based on typical dimensions of rolled W-shapes, c/h_0 would rarely be greater than 1.0 if the cope length is selected as the minimum required, and it may be much lower.

Depth-to-flange-width ratios (d/b) for rolled W-shapes vary between about 1.0 for column sections and 3.4 for deep beam sections. Although relatively long cope lengths are possible if the supporting member has a very wide flange—such as in the case of a W-shape chord of a large truss—or if the connection is skewed, the reduced depth of the beam in the coped region would likely be at least equal to the cope length. Based on the minimum required cope lengths of double-coped beams framing into equal-depth girders, the range of c/h_0 is between about 0.2 and 1.0. As such, three cope lengths were tested in this research: 100 mm, 150 mm,

and 175 mm. By testing some cope lengths larger than the practical maximum, the appropriateness of the equations governing the local stability of the coped region can be assessed, but beams with very long copes ($c/h_0 > 1.2$) are not considered here. Considering the chosen beam sections, equal top and bottom cope depths ($d_c = 30$ mm), and three cope lengths, the range of c/h_0 for specimens in this testing program is 0.29 to 1.19 and the range of c/d is 0.25 to 0.85, as shown in Table 3-1. Additional dimensions and key nondimensional geometric ratios are also shown in the table.

Table 3-1: Nominal coped region geometry

Beam Section	d (mm)	h_0 (mm)	t_w (mm)	d_{ct}/d	d/t_w	h_0/t_w	c (mm)	c/d	c/h_0
W200×27	207	147	5.8	0.14	35.7	25.3	100	0.48	0.68
							150	0.72	1.02
							175	0.85	1.19
W310×33	313	253	6.6	0.10	47.4	38.3	100	0.32	0.40
							150	0.48	0.59
							175	0.56	0.69
W410×54	403	343	7.5	0.07	53.7	45.7	100	0.25	0.29
							150	0.37	0.44
							175	0.43	0.51

The magnitude and direction of the applied axial load was also considered a critical parameter to the local stability of the coped region. Under compressive force, a connection may be more susceptible to a stability-based failure than a specimen subjected to shear only. Similarly, applied tensile force may act to stabilize the connection by delaying or preventing out-of-plane movement. Five axial load values were used to investigate these effects: 100 kN in tension, 0 kN, and 100 kN, 200 kN, and 300 kN in compression.

The rotational stiffness of the end-support—typically assumed in design to be zero for simple connections—was varied to investigate the effect of in-plane restraint on the connection capacity and behaviour. Simple connections that are considered to act as a pinned support can transfer moment to the support in sufficient magnitude to affect the behaviour if the actual in-plane restraint is significant. Because it is

generally considered unrealistic for designers to account for the rotational stiffness of the support at each connection, which would add significant computational effort combined with an uncertain outcome, the relevant design procedure should account for this effect. Comparing supports acting as an upper and lower bound for the rotational stiffness allows the critical capacity to be considered, thus accounting for a reasonable range of support cases and reducing the effort by the designer.

The end-support of a coped beam may either be made along the web, by bolting or welding to a parallel connection element such as an outstanding angle leg, or at the end of the coped region through the use of a welded end-plate. The latter is a common method used in industrial construction, and the method used in this research program, where the end-plate is typically shop welded to the end of the coped region and then field bolted to the support. The rotational stiffness of the connection is affected by the end-plate thickness, the bolt pattern, and the rotational (torsional for a girder) stiffness of the supporting member. As such, four end-supports were tested in this research, labelled A through D, which represent a range of potential support conditions both with and without end-plates. End-supports designated A or B had end-plates that were bolted to the supporting element, and those designated C or D were welded directly to the supporting element to eliminate the effect of the end-plate flexibility. End-support A represents a typical one-sided beam-to-girder connection, shown in Figure 1-2(a), which may exist in an exterior bay, and would not typically be subjected to high axial loads. End-support B represents a rotationally stiff boundary condition such as a symmetric scenario with connections on both sides of the girder web, shown in Figure 1-2(b), which may be subjected to larger compressive forces that pass through the connection. End-supports C and D are similar to end-supports B and A, respectively, however, the beams are welded directly to the support and do not have end-plates. The end-supports in ascending order of rotational stiffness are A, D, B, and C, and they are discussed further in Section 3.4.

The end rotation of a beam with simple supports depends on the stiffness of the connection and the beam itself. The effect of end rotation on double-coped connections was varied to investigate this effect when combined with in-plane

restraint from different end-supports. Astaneh's (1998) shear–rotation relationship showed that a "typical" beam end rotation reaches about 0.03 radians at the point where a plastic hinge is fully formed at the beam midspan. The relationship was studied for beams with span-to-depth ratios between 10 and 35, and the representative model proposed corresponds to a beam with a span-to-depth ratio of 25. For beams with low span-to-depth ratios, i.e., less than 10, end rotation can be less than 0.01 radians at the point the beam reaches the plastic moment, M_p. The numerical analysis was completed for the beam and connection only, and did not account for the additional stiffness from the floor system above, which would further decrease the end rotation. An end rotation of 0.03 radians is widely accepted as a reasonable upper limit for typical cases and has been used in previous testing programs; however, it is not unrealistic for beams to have very low end rotations at M_p. Therefore, specimens were tested at rotations of either 0 radians or 0.03 radians to investigate the effect of end rotation.

3.2.2 Specimen Matrix

To investigate the effects of beam section, cope length, axial load, end-support, and end rotation, 29 full-scale double-coped beam test specimens were fabricated and tested. The specimen matrix is summarized in Table 3-2.

Table 3-2: Specimen matrix

Section	W200×27			W310×33			W410×54		
Axial Load \ Cope length (mm)	100	150	175	100	150	175	100	150	175
100 kN tension	B C	–	–	–	A†	–	–	–	A†
0 kN	A A†	A A† D†	A A† B	–	A† D†	A†	–	–	A†
100 kN compression	A A† B C	–	–	A†	A†	A†	–	–	–
200 kN compression	–	–	–	B C	–	–	–	B	–
300 kN compression	–	–	–	–	–	–	B	B	B

† Specimen end rotation was 0 radians

The nominal dimensions and cope geometry for all specimens can be determined from the nominal dimensions of each beam section and the location of the specimen in the matrix. Where possible, the specimen geometry and testing conditions were selected to model a typical connection. For example, end-support A and D specimens are subjected to axial load magnitudes of up to only 100 kN, whereas end-support B and C specimens are subjected to axial loads up to 300 kN compression. Shallower specimens are also subjected to lower axial loads than deeper ones. Each test variable has several potential comparisons so its effect can be quantified through the tested capacities. Specimens were tested at an end rotation of 0.03 radians unless indicated otherwise in Table 3-2. Test specimens were assigned a five–variable alphanumeric identification (ID) that includes information on the cope geometry, end-support type, applied axial load, and end rotation, as described in Figure 3-1.

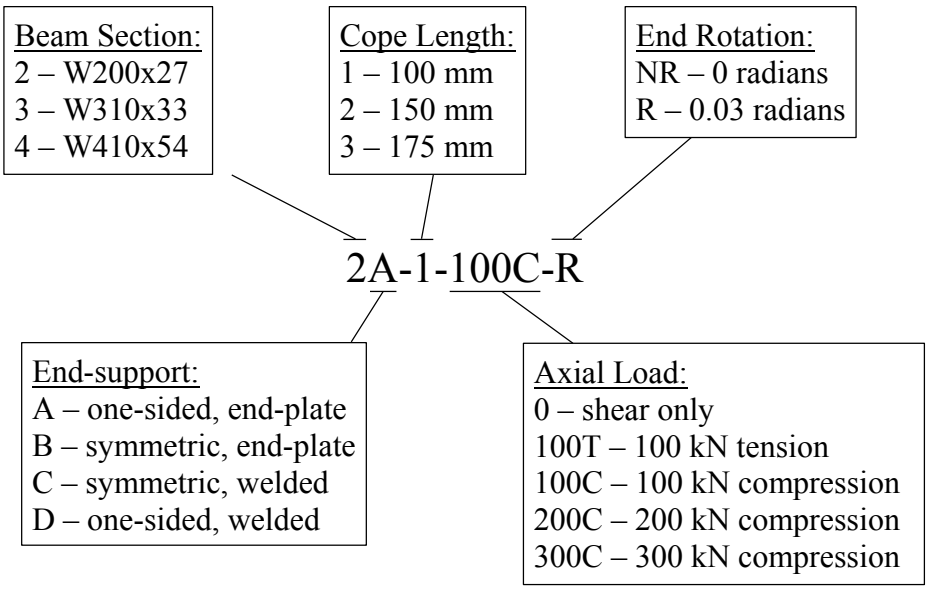

Figure 3-1: Specimen ID convention

The specimen group—the group of specimens with identical nominal geometry at the coped region and end-support type—is represented by the first three variables in the ID, e.g., 2A-1 is the group of four W200×27 specimens with 100 mm cope lengths and end-support A, whereas 2A-1-100C-R is one specimen in that group tested at an end rotation of 0.03 radians and with an axial load of 100 kN compression.

3.2.3 Specimen Design

The test specimens, shown schematically in Figure 3-2 for end-supports A and B, were fabricated from beam stubs and coped at one end only—the opposite end was used to connect the specimen to the test set-up. All specimens were specified to be coped at both the top and bottom flanges with equal cope lengths and the same cope depth and radius at the re-entrant corners: 30 mm and 12.7 mm (½ in), respectively. The cope depth is based on the required clearance in a typical beam-to-girder connection, and the radius at the re-entrant corners is the minimum recommended in the AISC *Manual* (AISC 2011)—radii greater than the minimum would have less severe stress concentrations. Copes were cut manually by thermal cutting according to the recommended coping practices in the AISC *Manual* (AISC 2011). All beam stubs were fabricated from CSA-G40.21-13 (CSA 2013) grade 350W steel.

End-plates at the coped end were fabricated from CSA-G40.21-13 (CSA 2013) grade 300W steel and had the same bolt pattern that differed only in the number of horizontal bolt rows: W200×27, W310×33, and W410×54 specimens with end-plates had two, three, and four rows of bolts, respectively. End-plates were made from 9.5 mm (⅜ in) flat bar with a nominal width—perpendicular to the rolling direction—of 152.4 mm (6 in). Bolt holes were drilled to 20.6 mm (13/16 in) diameter for 19.1 mm (¾ in) diameter ASTM A325 bolts. Bolt gauge and pitch for end-plates were 100 mm and 80 mm, respectively, and the edge and end distances were 26.2 mm and 35 mm, respectively. The total height of the end-plate was based on the number of bolt rows, the pitch, and the end distance, and therefore was not exactly equal to the reduced beam depth, which was based on the beam section depth and the cope depth at the top and bottom flanges. End-plates were welded, centered vertically, to the coped region using 6 mm fillet welds on both sides of the web with E49XX electrodes. Specimens without end-plates were welded directly to the support using the same weld size and type. The overall beam stub length, including the end plate if present, was 407 mm for all specimens with end-supports A and D (connected to a girder web), and 500 mm for all specimens

with end-supports B and C (connected to a column-stub flange), based on the required clearance between the support at the coped end, and the test set-up at the opposite end.

Connections at the uncoped end were made to the test set-up by a standardized moment connection with a 31.8 mm (1¼ in) end-plate and either 8 or 12 pretensioned 25.4 mm (1 in) diameter A325 bolts, depending on the beam section, with a 130 mm gauge and 100 mm pitch. Moment connection end-plates were welded at both flanges and the web of the test specimens using 6, 8, or 10 mm fillet welds, as appropriate. Due to the depth of the W310×33 specimens interfering with the bolt pattern, 12.7 mm (½ in) stiffeners were added at the top and bottom of the beam flanges to strengthen the moment connection.

As-built dimensions for all test specimens were measured prior to testing to confirm the specimens were fabricated as specified. Coped region dimensions are reported in Table 3-3 according to the notation in Figure 2-2. All measurements were completed with a digital caliper except the section depth, which was measured using a tape measure. The dimensions reported are the average of several measurements taken at different locations because of variability in each dimension. The reduced beam depth, h_0, was calculated by subtracting the average cope depth at the top and bottom flanges from the section depth. End-plate dimensions such as plate thickness, edge and end distance, and bolt gauge and pitch were measured and found to be within normal fabrication tolerances, but were not recorded because they are not critical to the calculated capacity of the connection. Re-entrant corner radii and end-plate weld sizes were observed to be consistent with those specified, but were not measured.

Specimens of the same beam section were not necessarily fabricated from the same steel heat because specimens with different end-supports were fabricated in batches, meaning material properties are not constant among specimens of the same beam section. The corresponding beam and end-plate material for each specimen are also reported in Table 3-3. Material properties and material testing methods are discussed in Section 3.3.

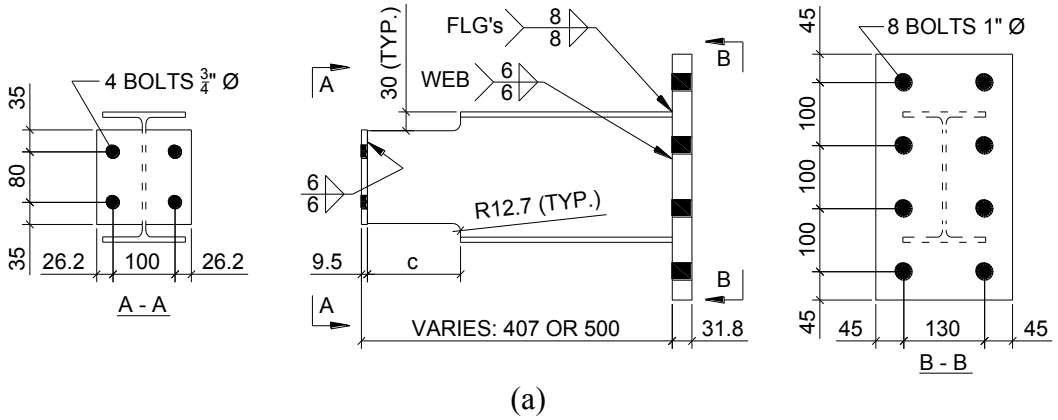

(a)

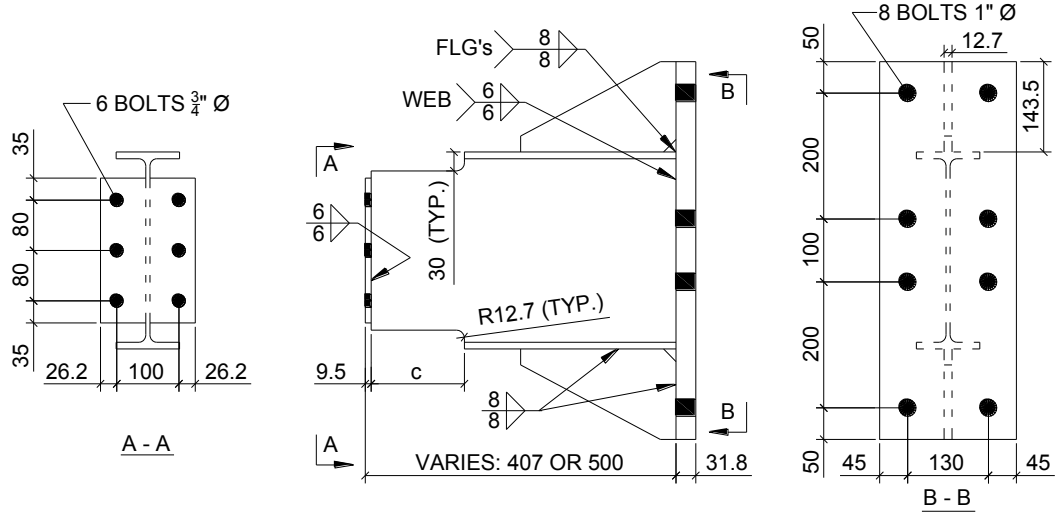

(b)

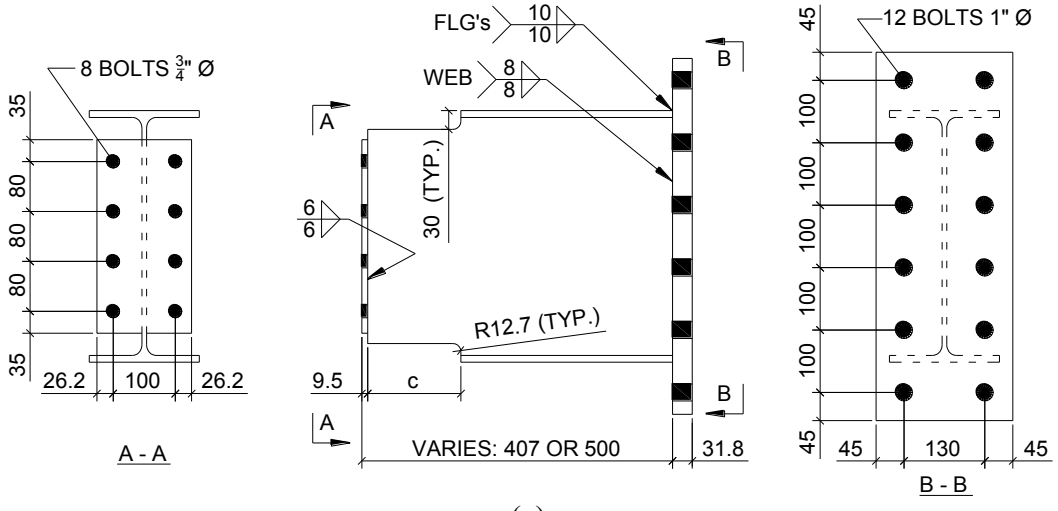

(c)

Figure 3-2: Specimen dimensions for (a) 2A, 2B (b) 3A, 3B and (c) 4A, 4B

Because there is no widely-accepted design method available for the local design of double-coped beams, the unfactored shear capacity of each test specimen was predicted based on the design procedures used at Waiward Steel Fabricators Ltd. of Edmonton, Alberta, referred to as "the Fabricator" in the remainder of this document, using the as-built dimensions and material properties. The procedure examines each component in the connection for its shear and axial capacity; however, it is common for the coped region to govern the capacity over the end-plate and the bolts. The predicted shear capacity and associated failure modes are shown in Table 3-3. Appendix A provides detailed sample calculations for two test specimens.

The Fabricator's procedure generally uses the capacity equations presented in Section 2.3 to evaluate the strength and stability of the coped region with known dimensions, material properties, and applied loads. To calculate the capacity of the test specimens, the specified axial load was entered and the applied shear load was increased until one of the limit states was reached. Several design checks were completed, as described below, but only four failure modes were predicted to govern the coped region of the test specimens: flexural yielding (FY), lateral–torsional buckling (LTB), the interaction of axial tension and bending (TB), and the interaction of axial compression and bending (CB).

First, the cross-sectional strength is considered—the axial yield strength of the net section (Equation 2-36) is checked against the specified axial load and the shear yield strength, assuming an elastic distribution (Equation 2-37), is compared to the applied shear load. To account for the effect of strain hardening, the 0.577 shear coefficient in Equation 2-37 is increased to 0.66 according to CSA Standard S16 (CSA 2014). These checks did not govern the test specimens because the axial loads selected for the tests were low compared to the axial yield strength of the net section, and the coped region geometries that resulted in a shear yielding failure were avoided because the local stability of the coped region was considered an important aspect to this research.

Table 3-3: Test specimen as-built properties

Specimen ID	Dimensions						Material type		Fabricator's procedure	
	d (mm)	c (mm)	d_{ct} (mm)	d_{cb} (mm)	h_0 (mm)	t_w (mm)	Beam	End-plate	Capacity (kN)	Failure mode†
2A-1-0-R	208	101.1	29.2	30.5	148.3	5.8	IV	2	105	FY
2A-1-0-NR	209	100.9	29.9	29.5	149.6	5.8	IV	2	106	FY
2A-1-100C-R	205	101.3	31.0	31.4	142.6	6.1	V	2	58	CB
2A-1-100C-NR	204	100.1	29.8	31.4	142.7	6.1	V	2	58	CB
2A-2-0-R	208	150.9	28.7	29.0	150.3	5.6	IV	2	69	LTB
2A-2-0-NR	205	149.1	30.6	31.1	143.3	6.2	V	2	75	FY
2A-3-0-R	207	176.0	28.9	29.3	148.7	5.7	IV	2	53	LTB
2A-3-0-NR	204	175.6	30.0	29.4	144.6	6.0	V	2	61	LTB
2B-1-100T-R	209	99.4	29.3	28.7	151.0	5.9	I	1	75	TB
2B-1-100C-R	208	99.2	29.6	29.0	149.5	5.9	I	1	57	CB
2B-3-0-R	208	181.8	28.7	27.2	152.1	5.8	I	1	55	LTB
2C-1-100T-R	209	98.0	29.0	28.6	151.4	5.8	I	–	83	TB
2C-1-100C-R	209	98.3	27.3	29.2	152.5	5.8	I	–	65	CB
2D-2-0-NR	209	150.5	30.4	27.7	150.9	5.5	IV	–	71	LTB
3A-1-100C-NR	313	102.8	30.9	30.1	252.0	6.5	VI	2	212	CB
3A-2-100T-NR	314	149.1	30.9	29.7	253.4	6.5	VI	2	187	LTB
3A-2-0-NR	314	148.5	30.7	31.4	251.9	6.3	VI	2	174	LTB
3A-2-100C-NR	313	150.5	31.3	30.5	251.2	6.5	VI	2	113	CB
3A-3-0-NR	314	175.0	31.0	33.1	249.9	6.4	VI	2	132	LTB
3A-3-100C-NR	313	175.6	30.3	33.7	249.0	6.5	VI	2	79	CB
3B-1-200C-R	311	99.7	29.3	30.8	250.9	7.2	II	1	233	CB
3C-1-200C-R	311	98.3	30.7	30.6	249.7	7.2	II	–	265	CB
3D-2-0-NR	313	151.5	29.8	28.1	255.2	6.6	VI	–	208	LTB
4A-3-100T-NR	403	176.0	31.4	30.4	341.1	6.7	VII	2	204	LTB
4A-3-0-NR	403	175.0	31.6	30.6	340.8	6.9	VII	2	225	LTB
4B-1-300C-R	404	100.1	31.7	30.2	342.1	7.2	III	1	362	CB
4B-2-200C-R	405	149.3	31.3	31.1	342.6	7.1	III	1	219	CB
4B-2-300C-R	404	148.1	30.3	29.6	344.1	7.2	III	1	178	CB
4B-3-300C-R	405	176.1	31.5	33.0	340.4	7.1	III	1	73	CB

† Failure modes: FY – Flexural yielding
LTB – Lateral–torsional buckling
TB – Bending and tension interaction
CB – Bending and compression interaction

Next, the flexural strength of the coped region is compared to the moment demand at the cope face, given in Equation 2-3, assuming the inflection point is at the face of the support. The critical beam end reaction can be solved by setting the flexural strength equal to the flexural demand. The flexural buckling strength method in the AISC *Manual* (AISC 2011) is checked, but local web buckling from Equations 2-16 and 2-17 does not govern due to the relatively low d/t_w and c/d ratios of the test specimens (see Figure 2-5). The Fabricator uses the plastic moment capacity (Equation 2-40) to determine the flexural strength of the coped region when local buckling does not govern.

For specimens subjected to combined tensile and bending normal stresses, an interaction equation similar to Equation 2-41 is checked. The effect of shear stresses are neglected ($V/V_p = 0$), and the exponent to the axial load to resistance ratio (P/P_y) is conservatively taken as one. The interaction is checked at the face of the cope where the applied moment is taken as the beam end reaction multiplied by the geometric eccentricity.

Finally, the stability of the coped region may be governed either by elastic lateral–torsional buckling or by the interaction of bending and compressive stresses. To determine if elastic lateral–torsional buckling occurs, the web thickness is compared to the minimum thickness requirement in Equation 2-49; however, to provide some ductility and ensure yielding occurs, the 0.716 coefficient is increased to 0.877, which corresponds to setting the unbraced moment capacity (Equation 2-48) equal to the plastic moment (Equation 2-40) rather than the yield moment (Equation 2-39). If the web thickness of the coped region is less than this minimum, the flexural strength is calculated with the elastic lateral–torsional buckling formulation in Equation 2-48, even though in reality some yielding will take place, and the Fabricator uses $\omega_2 = 1.0$ (Equation 2-47) assuming that the moment is constant over the coped region. If the web thickness is greater than the minimum, the flexural strength is assumed to be the plastic moment if no axial force is present. If the specimen is subjected to compression, the Fabricator considers the coped region to act as a beam–column, as discussed in Section 2.3.2.4, and accounts

for the interaction of bending and compressive stresses using the interaction equations given in CSA Standard S16 (CSA 2014).

The Fabricator's procedure does not explicitly account for end rotation or the in-plane restraint from different end-support types, but does account for different specimen geometries and material properties. The procedure also evaluates the shear and axial resistance of the end-plate, including the weld capacity, block shear and bearing failure, and bolt shear and tension interaction including prying effects; however, they are not discussed here because all test specimen capacities were governed by the coped region according to the Fabricator's procedure.

3.3 Material Properties

A series of ancillary tests were completed to determine the relevant material properties of the beams and end-plates at the coped end used in the test specimens. All test specimens fabricated from the same material heat were cut from the same piece, and an additional beam stub or flat bar, also cut from the same piece, was provided for material testing.

Sheet-type tension coupons were water-jet cut from the webs of the beam sections and flat bars in a dogbone profile. All coupons were cut parallel to the longitudinal axis of beam sections, and parallel to the rolling direction for flat bar specimens. Three coupons were cut for each material except Beam I, where four were cut due to a water-jet cutting error at the grip location in one coupon (although this error is not considered to have affected the coupon test result).

Coupon tests were performed using the method prescribed in ASTM Standard A370-14 (ASTM 2014). Load was applied at a rate of 0.25 mm per minute in the elastic region, and was increased to a rate of 2.5 mm per minute following the onset of strain hardening. During each coupon test, static readings were taken at a minimum of three points during the yield plateau, and averaged to find the static yield strength, and once at the approximate maximum engineering stress for the static ultimate strength.

The engineering stress was calculated by dividing the applied force, measured by a load cell in the testing apparatus, by the initial area of the coupon in the reduced section, measured with a digital caliper. Strain was measured with a 50 mm gauge length extensometer, which was removed during the latter stages of testing to avoid potential damage. The static yield strength for the end-plate specimens, which did not have defined yield plateaus, was found using the 0.2% offset method. The elastic modulus for all coupons was found using a linear regression technique on the elastic portion of the stress–strain curve. The final elongation is presented as a percentage of the measured gauge length, and the reduction of area is the percentage difference comparing the initial and final cross-sectional areas. A summary of the material property data is presented in Table 3-4, and stress–strain curves for all coupons can be found in Appendix B.

3.4 Test Set-up

The test set-up was designed to model a double-coped beam subjected to combined vertical and horizontal loads with different end-support types, and it allowed for any combination of vertical load, horizontal load, and end rotation to be applied to the connection. Because the end-support type varied, two reaction systems were used: one for end-supports A and D, shown in Figure 3-3, which represents a beam on one side of a girder, and one for end-supports B and C, shown in Figure 3-4, which simulates the behaviour of two connections symmetric about the girder web or another case where in-pane rotation is highly restrained. (Note that the test specimen is not present in either figure.) Schematics of the test set-ups in elevation are shown in Figure 3-5 and Figure 3-7, and the set-up for end-supports A and D is depicted in plan in Figure 3-6.

Connections were tested using a system of three independent hydraulic actuators—two vertical and one horizontal (see Figure 3-5 to Figure 3-7). Actuators 1 and 2 were used to apply vertical load and to apply and control rotation, respectively. Actuator 3—actually two actuators in parallel—was used to apply horizontal load. Each actuator was pinned at both ends to allow rotation in the plane of the beam web.

Table 3-4: Material properties

Coupon Mark	Elastic Modulus (MPa)	Yield Strength (MPa)	Ultimate Strength (MPa)	Final Elongation (%)	Reduction of Area (%)
W200×27 - Beam I					
i	202 832	362	449	35.4%	70.0%
ii	200 465	360	428	35.2%	70.8%
iii	203 760	353	429	36.4%	71.5%
iv	202 626	361	443	36.6%	68.3%
Mean	202 421	359	437	35.9%	70.2%
W310×33 - Beam II					
i	197 074	400	465	32.5%	61.4%
ii	196 730	398	468	32.9%	62.9%
iii	195 906	391	466	30.2%	62.3%
Mean	196 570	396	466	31.9%	62.2%
W410×54 - Beam III					
i	199 791	392	491	35.1%	64.7%
ii	196 184	405	493	36.0%	64.3%
iii	194 823	392	474	34.9%	63.6%
Mean	196 933	396	486	35.3%	64.2%
W200×27 - Beam IV					
i	197 935	362	442	32.9%	63.0%
ii	197 350	363	445	33.4%	64.0%
iii	198 826	362	443	35.9%	63.7%
Mean	198 037	362	443	34.1%	63.6%
W200×27 - Beam V					
i	192 476	370	470	31.2%	60.7%
ii	197 944	382	479	33.6%	59.5%
iii	197 790	377	475	36.3%	59.2%
Mean	196 070	376	475	33.7%	59.8%
W310×33 - Beam VI					
i	199 287	355	442	38.3%	64.5%
ii	194 738	355	441	33.7%	62.2%
iii	194 948	356	447	40.0%	62.4%
Mean	196 324	355	443	37.4%	63.0%
W410×54 - Beam VII					
i	196 181	435	505	34.4%	64.8%
ii	194 579	435	503	33.0%	66.6%
iii	194 052	431	508	34.2%	63.2%
Mean	194 937	434	506	33.9%	64.9%
End-plate bar 1					
i	203 415	433	498	27.7%	64.5%
ii	204 856	437	503	26.3%	64.5%
iii	202 446	443	504	25.4%	63.2%
Mean	203 572	438	502	26.5%	64.1%
End-plate bar 2					
i	198 552	408	460	31.7%	55.5%
ii	194 371	410	460	31.6%	58.8%
iii	198 963	410	463	32.2%	58.0%
Mean	197 295	409	461	31.8%	57.4%

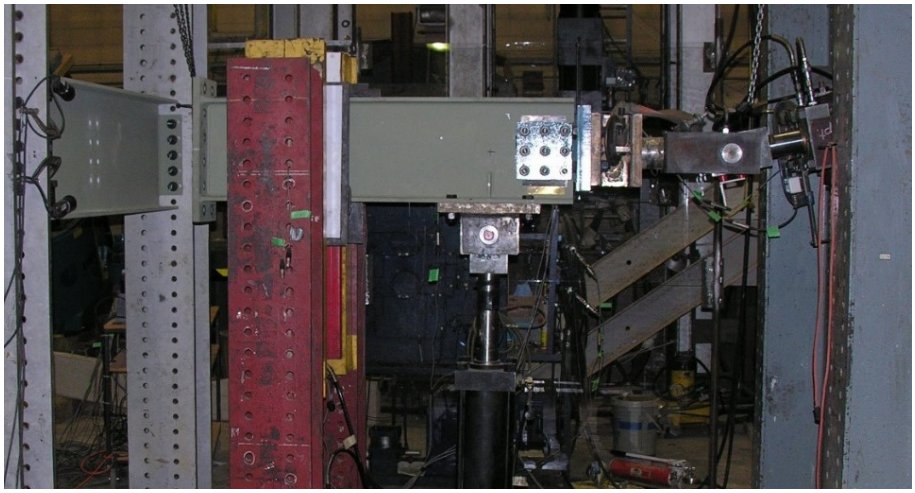

Figure 3-3: Test set-up for end-support A (D similar)

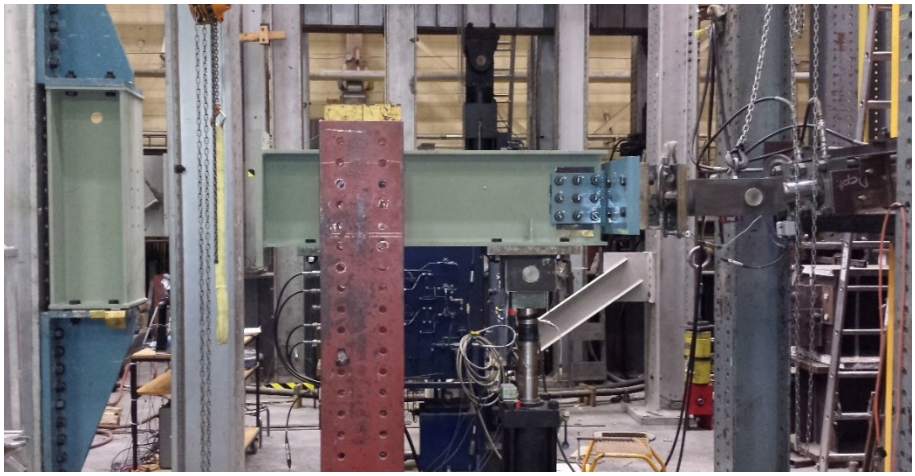

Figure 3-4: Test set-up for end-support B (C similar)

Reaction forces were provided by a steel base plate and strong floor for the two vertical actuators, and a pair of steel plate shear walls for the horizontal actuator. For specimens tested at an end rotation of 0.03 radians, Actuator 3 was inclined so the actuator and beam centrelines were approximately aligned when the specified rotation was met. For specimens tested without end rotation, Actuator 3 was aligned horizontally. In this orientation, the connection is loaded upwards.

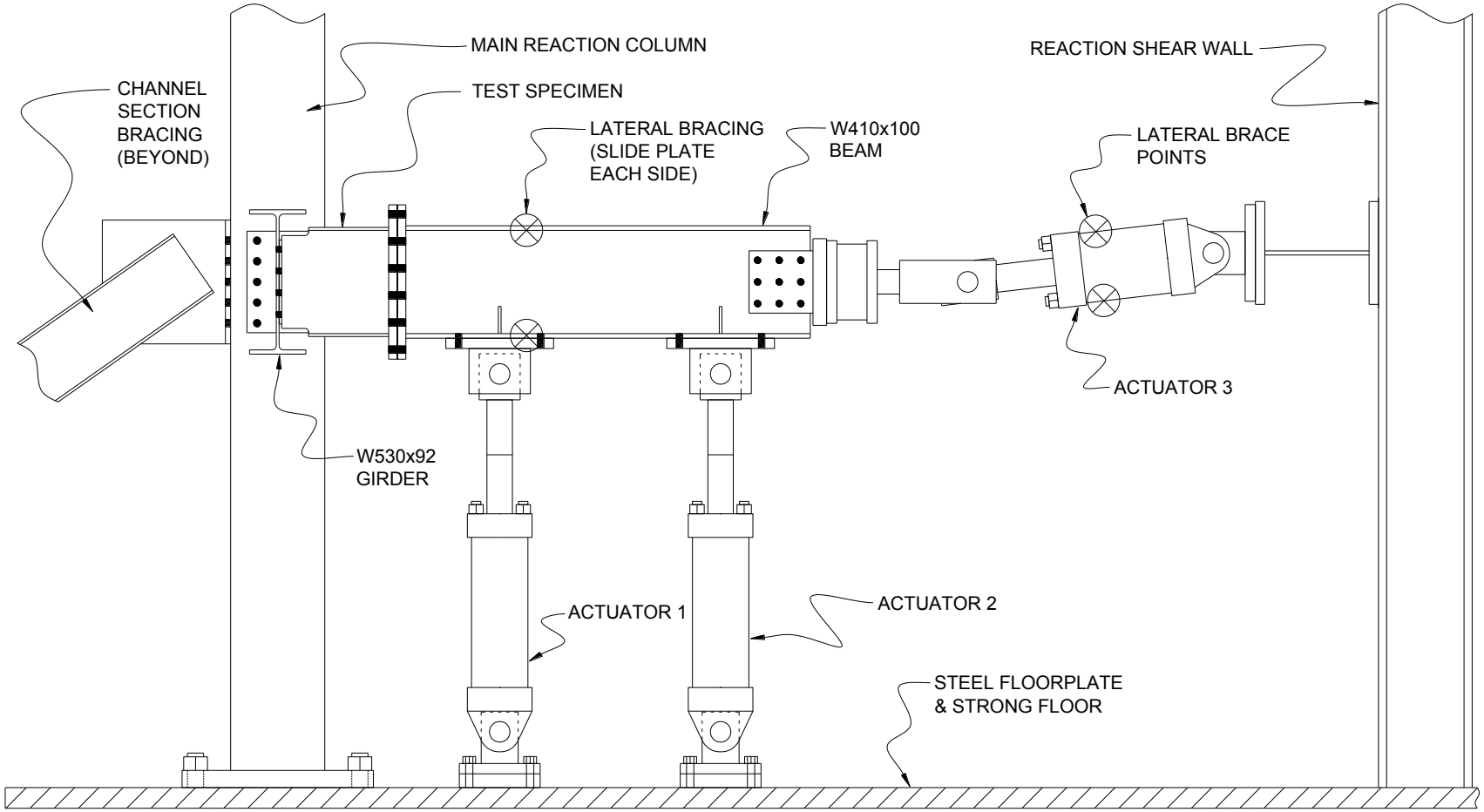

Figure 3-5: Test set-up for end-support A in elevation (D similar)

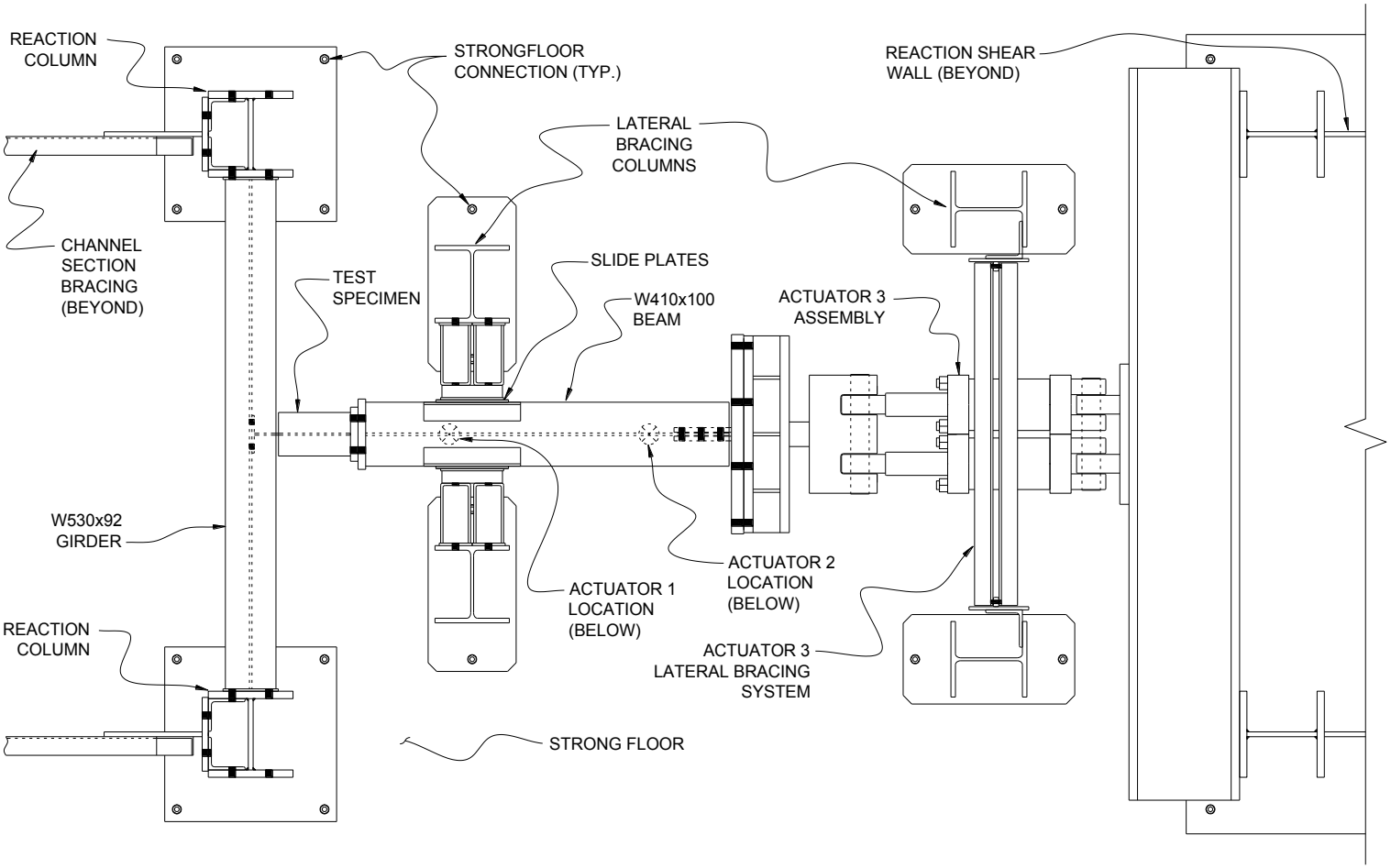

Figure 3-6: Test set-up for end-support A in plan (D similar)

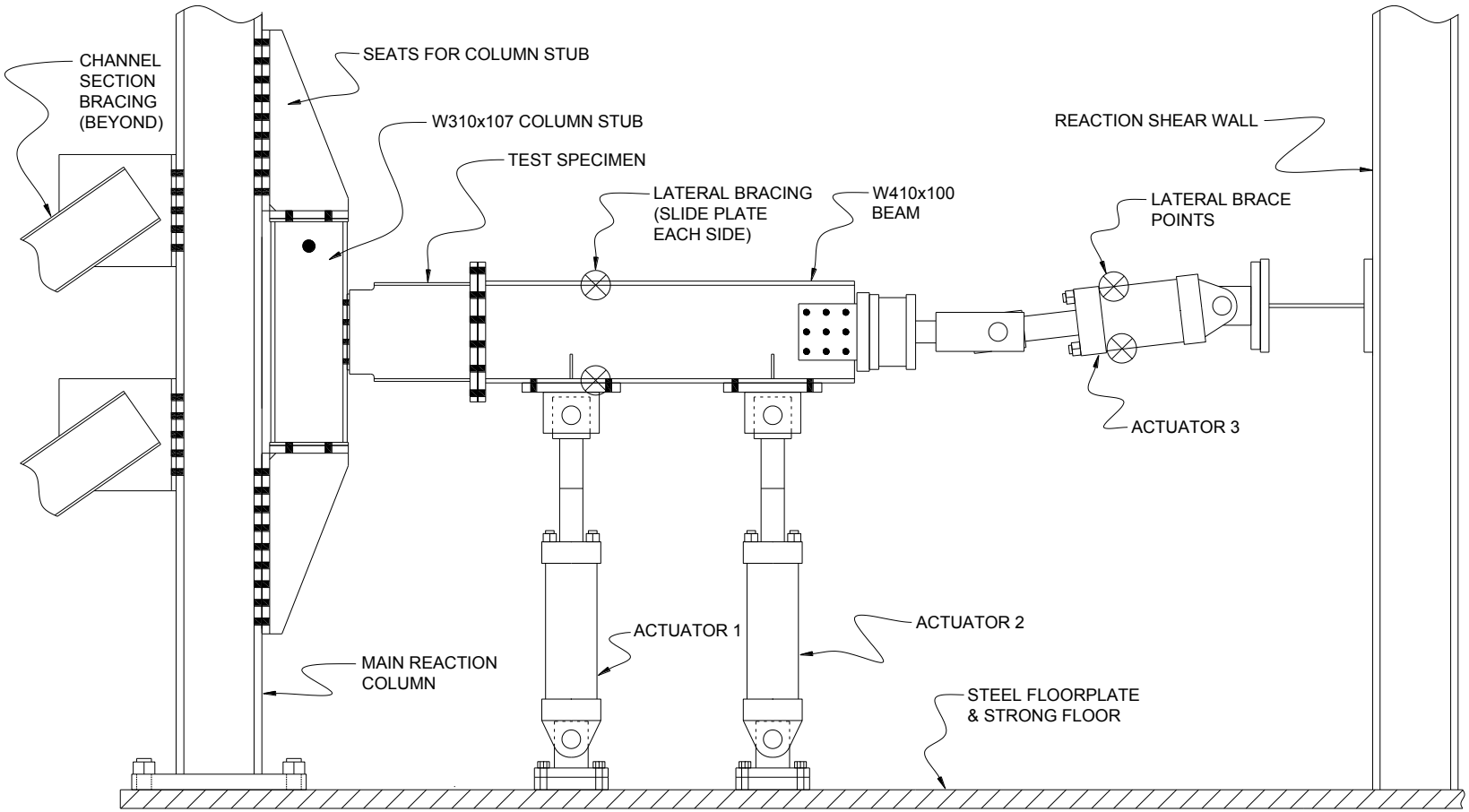

Figure 3-7: Test set-up for end-support B in elevation (C similar)

A W410×100 beam, shown schematically in Figure 3-8, connected the three actuators to the test specimen in all tests.

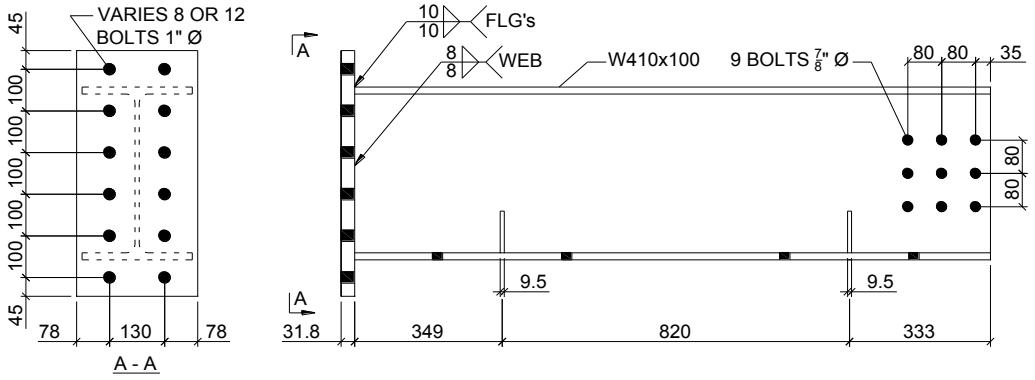

Figure 3-8: W410×100 beam dimensions

This beam section was chosen to resist the predicted applied loads to the test specimen, and to meet the required geometry of the actuator connections and bracing system. The vertical actuators were connected to the beam at the bottom flange using four 25.4 mm (1 in) diameter pretensioned A325 bolts, and the horizontal actuator was connected to the beam using a 12.7 mm (½ in) lap plate on each side of the beam web and nine 22.2 mm (7/8 in) diameter pretensioned A325 bolts in double shear. The lap plates were welded to a 50.8 mm (2 in) thick load transfer plate that was bolted to the horizontal actuator using eight 25.4 mm (1 in) diameter pretensioned A325 bolts. 9.5 mm (⅜ in) thick partial-depth stiffeners were provided on each side of the W410×100 beam web at the location of the vertical actuator connections to prevent web crippling or yielding. At the moment connection to the test specimen, a 31.8 mm (1¼ in) thick end-plate was used—welded to the web and both flanges of the beam with 8 mm and 10 mm fillet welds, respectively. The moment connection bolt pattern—130 mm gauge and 100 mm pitch—matched the uncoped end of all test specimens and was connected with eight or twelve 25.4 mm (1 in) diameter pretensioned A325 bolts, according to the test specimen depth.

The supporting member at the coped end of the test specimens was either a girder, for end-supports A and D, or a column stub, for B and C. For end-support A, the

girder was a 2062 mm long W530×92 member, shown schematically in Figure 3-9, connected to braced reaction columns at both ends using 9.5 mm (⅜ in) thick end-plates welded to the web only, to allow warping, and ten 25.4 mm (1 in) diameter pretensioned A325 bolts.

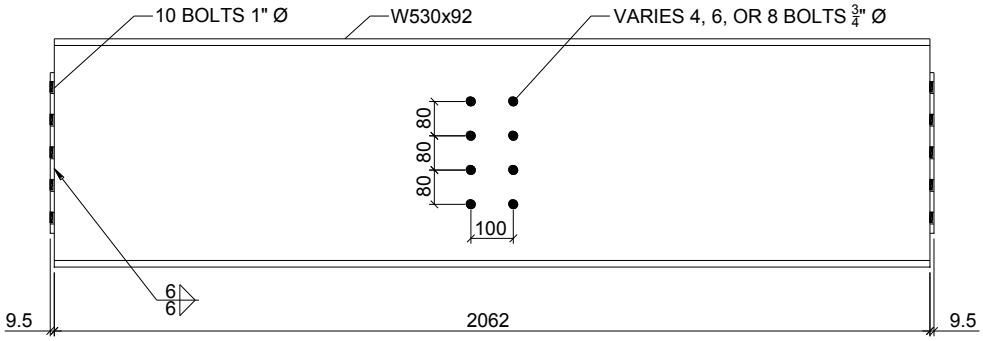

Figure 3-9: W530×92 girder dimensions for end-support A

The girder section was selected to be reused for all tests with end-support A, and was required to resist the biaxial moments applied from the test specimen with the highest predicted vertical and horizontal loads. The connection of the test specimen to the girder web was centred longitudinally and vertically, and matched the bolt pattern in the connection end-plates—100 mm gauge and 80 mm pitch. Four horizontal rows of bolt holes were provided to accept all specimen types.

For end-support B, a 900 mm long W310×107 column stub was used, shown schematically in Figure 3-10.

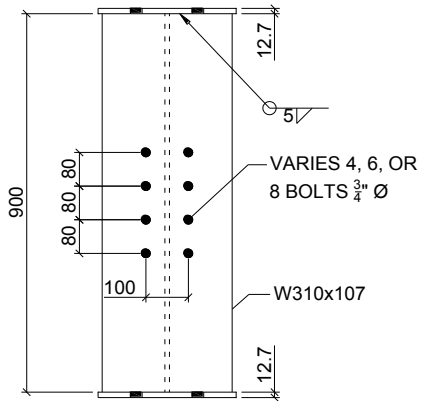

Figure 3-10: W310×107 column stub dimensions for end-support B

The column was capped at the top and bottom with 12.7 mm (½ in) plates used to connect the column stub to a reaction column using heavy seats at the top and bottom. The stub column, selected for strength and geometric parameters, was reused for all tests with end-support B. The connection to the column stub was made at the flange to provide high in-plane restraint, and the hole pattern matched those previously described for all coped end connections.

The three end-support C tests used similar column stubs to those used with end-support B; however, they were fabricated with test specimens welded directly to the flange. Therefore, end-support C column stubs were used only once.

Two end-support D tests were conducted. Because the girders for these two tests would be used only once, a shallower section could be used to create a more typical beam-to-girder connection. Accounting for the predicted strength of each specimen, 2D-2-0-NR was welded to a W200×36 girder, and 3D-3-0-NR was welded to a W310×39 girder. End-plates for these girders were similar to those used on the W530x92 girder, but had two and three horizontal rows of bolts, respectively, compared to five rows.

Lateral supports were provided to the beam at two locations: near Actuator 1 close to the test specimen, and at Actuator 3 (see Figure 3-6). In both locations, support was provided on both sides of the test set-up. At Actuator 1, steel-backed Teflon® slide plates were used, which reacted against the flanges of bracing columns mounted to the strong floor. At Actuator 3, lateral braces with end rollers reacted against stiff steel running surfaces.

3.5 Instrumentation

Figure 3-11 shows the general arrangement of electronic instrumentation used in this testing program to measure the applied forces and resulting displacements and rotations of the test specimens. The instruments were connected to an HBM MGCplus® data acquisition system, and HBM's catmanEasy® data acquisition software recorded a data point from each instrument at a frequency of 0.5 Hz.

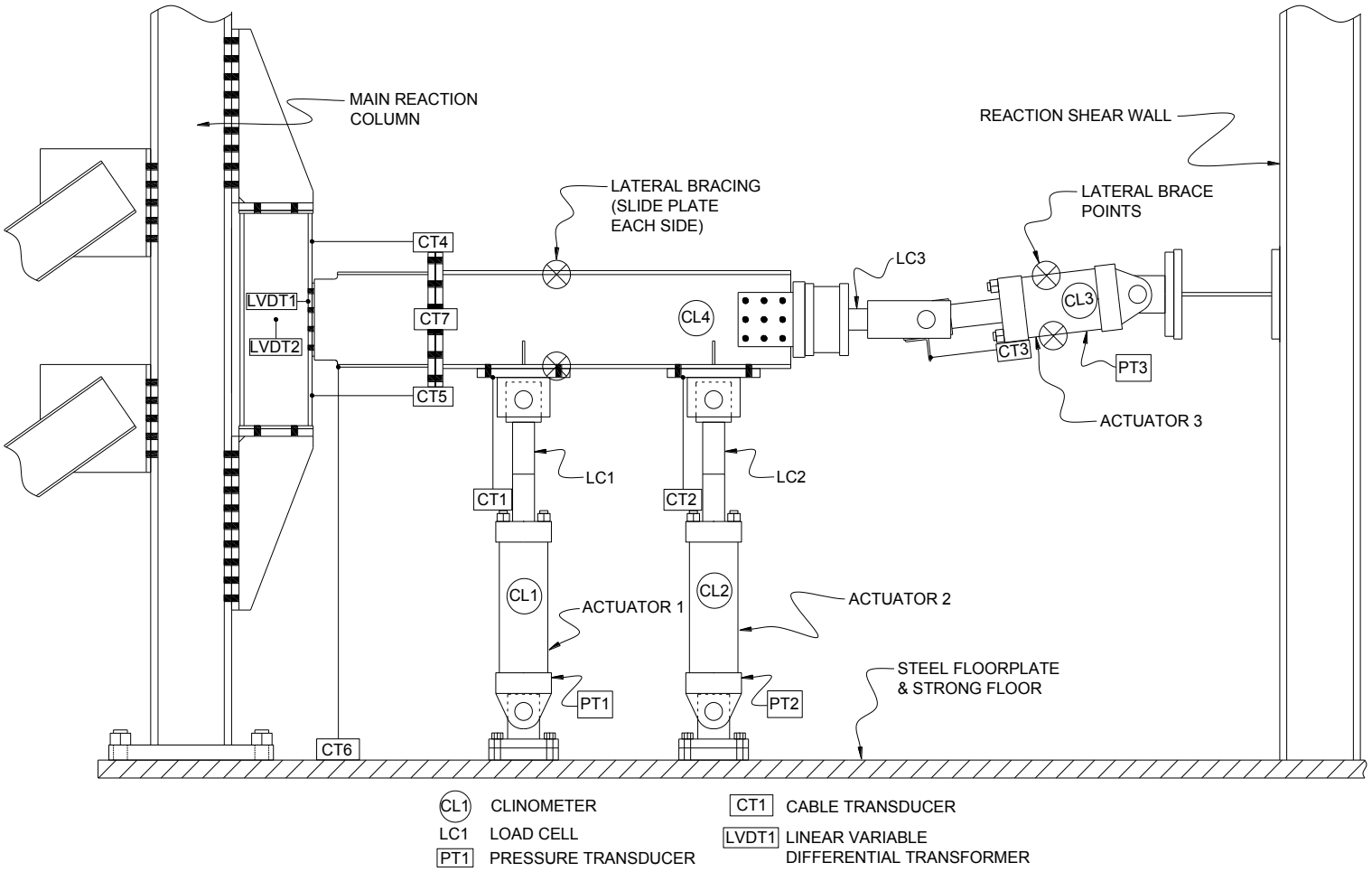

Figure 3-11: Instrumentation diagram for end-support B (other tests similar)

The software also performed real-time calculations based on instrumentation data so the test operator could accurately apply the specified horizontal load and end rotation and monitor the connection behaviour.

Each of the three actuators was instrumented with an electronic load cell, clinometer, and cable transducer to measure the applied force, rotation, and stroke, respectively. The magnitude, direction, and location of the forces applied to the test beam from each actuator were explicitly calculated throughout the test by resolving the applied forces into their orthogonal components. By summing the three vertical and three horizontal load components, the total loads on the connection in those principal directions were calculated. Additionally, moment applied at the face of the end-support was calculated using the horizontal and vertical load components of each actuator and their respective moment arms, which were determined using the attached cable transducers and clinometers and the initial dimensions of the test set-up measured prior to each test. Pressure transducers installed on the actuator hydraulic lines provided redundant force measurements through the calculation of the applied force.

End rotation was measured directly using a clinometer mounted to the beam web. The rotation was also calculated for redundancy using the cable transducers and clinometers on Actuators 1 and 2, and the ratio of the rotation from the clinometer to the calculated rotation was monitored during the tests to confirm that the instruments were operating correctly.

Relative horizontal in-plane displacement of the specimen between the moment connection (between the W410×100 beam and the test specimen) and the support was measured by two cable transducers: one above and one below the specimen. Under the rotation phase, these cable transducers were also used to confirm the measurement of the beam rotation by the clinometer.

An additional cable transducer monitored out-of-plane displacement of the test specimen at the moment connection location. To minimize the error resulting from in-plane movement of the specimen, the cable transducer was connected over a

metre away from the plane of coped region. The displacement never exceeded 7 mm at the peak vertical load.

The vertical displacement of the specimen was measured by a cable transducer connected at the tip of the bottom flange, immediately adjacent to the cope. Note that this location depends on the cope length and was not the same distance from the support for all tests. The error in the vertical measurement resulting from in-plane horizontal displacement of this point was minimized by connecting the cable transducer to the steel floor plate, which was about two meters away.

Two linear variable displacement transducers measured localized displacement of the column stub for tests with end-supports B and C. Out-of-plane movement of the web and bending of the flange directly behind the connection were monitored, but found to be very small for all tests. For end-supports A and D, girder rotation was measured by two clinometers: one mounted on the top flange and one mounted on the web next to the connection, centered vertically between the girder flanges.

3.6 Test Procedure

The procedure for all tests began with connecting the test specimen to the W410×100 beam. Actuator 3 was retracted to provide clearance between the test specimen and the support, and the beam was levelled using the readings from the attached clinometer. The test specimen was lifted into place with a chain hoist and bolted to the beam using the appropriate number of bolts, which were then pretensioned using the turn-of-nut method. Next, the beam was moved closer to the end-support using the horizontal load actuator and bolted to the support using new bolts for each test. The horizontal load and beam rotation were monitored and held constant at or near zero during this process. The bolts at the specimen connection were installed snug-tight, as is standard practice for shear connections not considered slip-critical or subjected to tensile loads. For 2A specimens, the middle two rows of bolt holes in the girder web were used, i.e., the test specimen was centred vertically at the connection to the girder. For 3A specimens, the top three bolt hole rows were used, and for 4A specimens, all four rows were used. Once the

specimen was installed, one side was whitewashed to observe the formation of yield lines, and the remaining instrumentation was installed and zeroed.

The actuators were operated manually in stroke-control with an air-driven hydraulic pump. Specimens with both end rotation and horizontal load were tested by first rotating the beam counter-clockwise (Figure 3-5 or Figure 3-7) to 0.03 radians—as discussed in Section 2.2.1—using Actuator 2. The vertical and horizontal loads were held constant at or near zero using Actuators 1 and 3, respectively. Once the rotation was achieved, horizontal load was applied using Actuator 3, while maintaining the end rotation. Finally, upward vertical load was applied to the specimen by Actuator 1 until failure, adjusting Actuators 2 and 3 as needed to maintain the desired rotation and axial load. Although this testing sequence may be considered unrealistic because the beam end rotation would tend to increase concurrently with the addition of vertical load on the beam, it was chosen to bracket the possible upper and lower bounds of likely beam end rotations. Ductile behaviour of the coped beam will mitigate the effect of the testing sequence.

The order of applied rotation and loads for specimens without end rotation or horizontal load (or both) was the same, with those steps removed. During the test, if a local event caused end rotation or horizontal load to deviate from the specified value, they were restored in the original order, i.e., end rotation, horizontal load, and then vertical load. If the horizontal load could not be maintained, i.e., if increasing the stroke of Actuator 3 resulted in a decrease in horizontal load, it was abandoned and the remainder of the test was completed by maintaining the end rotation only and applying vertical load. Failure of a test specimen was defined either by a sudden and significant decrease in vertical load or the development of significant deformation in the connection at a point where further displacement revealed no additional load-carrying capability.

3.7 Summary

A total of 29 double-coped beams were tested under the combined action of axial and shear forces. The strength and behaviour of double-coped connections were investigated by varying the test specimen geometry—beam section and cope

length—and the testing conditions—end-support, end rotation, and axial load. Test specimens were selected to have relatively low cope-length-to-reduced-beam-depth ratios—between 0.29 and 1.19—to cover more typical geometries not covered by previous investigations. Different end-supports provided upper and lower bounds for the in-plane rotational restraint of the test specimens, and axial loads were included to investigate stabilizing effects, for tensile loads, and destabilizing effects for compressive loads. As-built properties, including coped region dimensions and material properties, were measured and used with the Fabricator's procedure to predict the capacity and failure mode of each test specimen.

CHAPTER 4: RESULTS AND DISCUSSION

4.1 Introduction

In this chapter, the results of the 29 double-coped beam tests are presented and discussed. First, the test results—peak vertical load, vertical displacement, and failure mode—are shown for each specimen. Next, the observed test behaviour and failure modes are described. The distribution of moment in the coped region is examined, and the resulting location of the point of inflection is estimated to establish an effective load eccentricity. Finally, the effects of the tested variables are discussed and the currently-used design procedures are assessed based on the test results.

4.2 Test Results

Table 4-1 summarizes the peak vertical load, the corresponding vertical displacement, and the critical failure mode, defined in Section 4.3, for all of the double-coped beam tests. The reported vertical displacements have been adjusted to account for the initial vertical displacement of the specimen resulting from the rotation phase. During rotation, vertical displacement was imposed at the measurement location, immediately adjacent to the cope, while the vertical load was kept at or near zero. Therefore, vertical displacements reported in Table 4-1 and other tables in the remainder of this document have been adjusted by subtracting the initial vertical displacement following the rotation phase from the displacement at the peak vertical load (load versus displacement curves have not been adjusted). In all cases, the initial vertical displacement from the rotation phase was less than 5 mm. The effect of rotation is shown in Figure 4-1 for specimens 2A-1-0-R and 2A-1-0-NR. From the graph, the vertical displacements at the peak vertical load are 18.6 mm and 26.8 mm for specimens 2A-1-0-R and 2A-1-0-NR, respectively; however, specimen 2A-1-0-R experienced 3.3 mm of vertical displacement prior to the addition of vertical load, and therefore the reported vertical displacement at the peak vertical load for 2A-1-0-R is 15.3 mm.

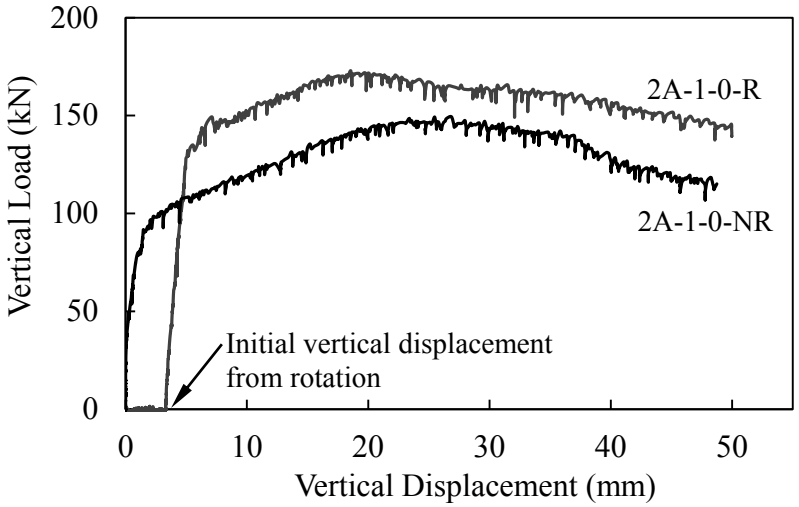

Figure 4-1: Load versus displacement for specimens 2A-1-0-R and 2A-1-0-NR

Of the five specimens that could not maintain the specified horizontal load, four had additional vertical load carrying capacity and were loaded further vertically until a secondary peak load was reached, and one only had a single peak vertical load. In all tables in this chapter, tabulated values for the four specimens with additional capacity are shown at both the primary (immediately prior to the horizontal load decrease) and secondary (immediately prior to the vertical load decrease; horizontal load uncontrolled) peak vertical loads as x / y, where x and y are the values associated with the primary and secondary peak vertical loads, respectively. Horizontal load failure is discussed further in Section 4.3.2.4.

Load–vertical displacement curves for all specimens can be found in Appendix C. For specimens tested in shear only, the vertical load is shown, and for specimens tested with horizontal load, both vertical and horizontal load relationships are shown. For ease of comparison, axis limits are constant within a group of specimen depths.

Table 4-1: Test results at peak vertical load

Specimen ID	Peak Vertical Load (kN)	Vertical Displacement (mm)	Critical Failure Mode†
2A-1-0-R	173	15.3	OPD
2A-1-0-NR	149	26.8	OPD
2A-1-100C-R	133	7.4	OPD
2A-1-100C-NR	83 / 112	1.2 / 29.8	HL
2A-2-0-R	111	19.6	OPD
2A-2-0-NR	110	29.4	OPD
2A-3-0-R	89	20.7	OPD
2A-3-0-NR	99	34.4	OPD
2B-1-100T-R	186	16.8	T
2B-1-100C-R	162	8.2	OPD
2B-3-0-R	138	5.8	OPD
2C-1-100T-R	208	21.0	T
2C-1-100C-R	114 / 166	1.3 / 10.0	HL
2D-2-0-NR	105	6.8	OPD
3A-1-100C-NR	260	5.7	OPD
3A-2-100T-NR	242	10.1	OPD
3A-2-0-NR	207	4.5	OPD
3A-2-100C-NR	191	2.0	OPD
3A-3-0-NR	199	5.4	OPD
3A-3-100C-NR	182	3.5	OPD
3B-1-200C-R	363	8.6	OPD
3C-1-200C-R	254 / 372	2.0 / 10.1	HL
3D-2-0-NR	235	5.6	OPD
4A-3-100T-NR	446	8.6	B
4A-3-0-NR	443	6.9	B
4B-1-300C-R	311 / 453	2.9 / 7.6	HL
4B-2-200C-R	479	9.4	B
4B-2-300C-R	428	4.8	HL
4B-3-300C-R	360	5.7	B

† Failure modes: OPD – Out-of-plane deformation
B – Buckling
T – Tearing
HL – Horizontal load failure

4.3 Failures Modes

4.3.1 Observed Behaviour

Yielding, out-of-plane deformation, buckling, and tearing were all observed in the testing program. Generally, the double-coped beams tested were ductile, and yielding was evident at early stages of loading from both the nonlinear load–displacement relationships and flaking whitewash in all test specimens. The coped regions of all specimens deformed out-of-plane in various shapes, and many specimens developed localized tears at the re-entrant corners or near the connection to the support. In the following sections, the deformed shapes of the test specimens are described in reference to the direction and magnitude of the free edge displacements in the coped region. All figures and descriptions relate to the as-tested orientation of the specimens (Figure 3-5 and Figure 3-7). Because the test specimens were loaded upwards, the upper and lower free edges of the coped region correspond to the bottom and top of a beam, respectively, in typical building construction. Unless indicated otherwise, specimen photographs were taken following the test after large vertical displacements and out-of-plane deformations had occurred and may not represent the specimen deformation at the peak vertical load.

4.3.2 Critical Failure Modes

The critical failure modes for the double-coped beams tested, considered to be that which caused the initial post-peak decrease in load, were: out-of-plane deformation (OPD), buckling (B), tearing at the re-entrant corner (T), or horizontal load failure (HL), as indicated in Table 4-1. Often, the critical failure mode and the final deformed shape of the specimen depended on the state of the coped region following the rotation and horizontal load phases, if present. Due to the different end supports used and the testing hierarchy (rotation, horizontal load, then vertical load), it was not uncommon for the coped region to yield locally and deform out-of-plane prior to the application of either horizontal or vertical load.

For specimens tested with end-support B or C (high rotational stiffness), local yielding was always present during the rotation phase because the end rotation was

achieved through the bending of the coped region and the end-plate, if present. Compressive stresses at the upper free edge of the coped region adjacent to the support and stress concentration at the upper re-entrant corner both caused local yielding during the rotation phase, shown in Figure 4-2 for 2C-1-100C-R.

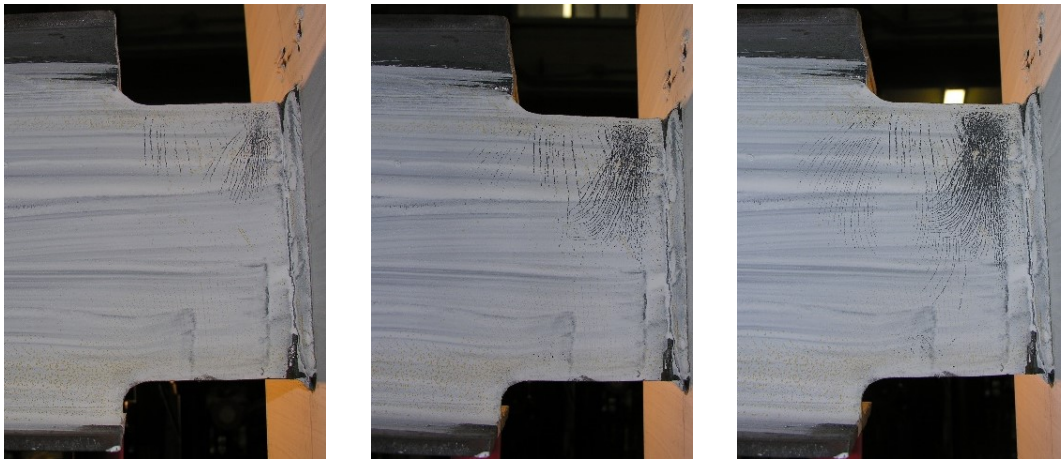

(a) (b) (c)

Figure 4-2: Specimen 2C-1-100C-R at (a) 0.01 radians, (b) 0.02 radians, and (c) 0.03 radians

The observed onset of out-of-plane deformation of the coped region also largely depended on the rotational stiffness of the end-support. Local yielding at the upper free edge was typically associated with out-of-plane deformation, the magnitude of which depended on the length of the coped region. Under a given rotation, specimens with short cope lengths had higher curvature over the coped region than specimens with longer cope lengths, resulting in higher strains and therefore larger out-of-plane deformations.

Conversely, specimens with end-supports A or D (low rotational stiffness) did not show evidence of local yielding in the coped region during the rotation of the beam because the rotation was easily accommodated by the girder—either through local deformation of the web for end-support A, because the girder depth was large compared to the depth of the specimen (deformation of the end plate in these specimens was typically small), or by global twisting of the girder for end-support D, because the girder and beam depths were approximately equal. As

such, the coped region typically remained in-plane prior to the application of vertical load.

4.3.2.1 Out-of-plane Deformation

Out-of-plane deformation is a ductile failure mode associated with the gradual deformation (as distinguished from abrupt buckling) of the coped region out of the plane of the beam web. The deformed shapes investigated after each test typically showed features of several modes, making it impractical to group the failure modes based on each specimen's deformed shape. Therefore, out-of-plane deformation is described by the gradual deformation of the coped region and is not dependent on the final shape of the test specimen. Specimens that failed by out-of-plane deformation generally had significant post-peak strength.

With the exception of specimen 3B-1-200C-R, all specimens that failed by out-of-plane deformation can be separated into two primary mode shapes, depending on the deformation at the upper free edge of the coped region. Specimens in the first mode shape deformed out-of-plane at both the upper and lower free edges of the coped region, but in opposite directions, as shown in Figure 4-3 for specimen 2A-3-0-NR. The coped region displaced laterally and twisted—a mode that could be considered similar in shape to lateral–torsional buckling of a beam under reverse in-plane curvature. The magnitude of out-of-plane deformation at the lower edge was always greater (see Figure 4-3(c)) due to high compressive stresses that caused the lower re-entrant corner to close. For specimens tested without rotation and for those that remained in-plane during the rotation phase, out-of-plane deformation of the coped region began at the lower free edge, with the greatest displacement occurring near the re-entrant corner, following the linear elastic portion of the vertical load–vertical displacement response. The upper free edge began to move out-of-plane at or near the peak load, and the deformation at both edges progressed gradually throughout the remainder of the test. The cross-section twisted, but generally did not distort.

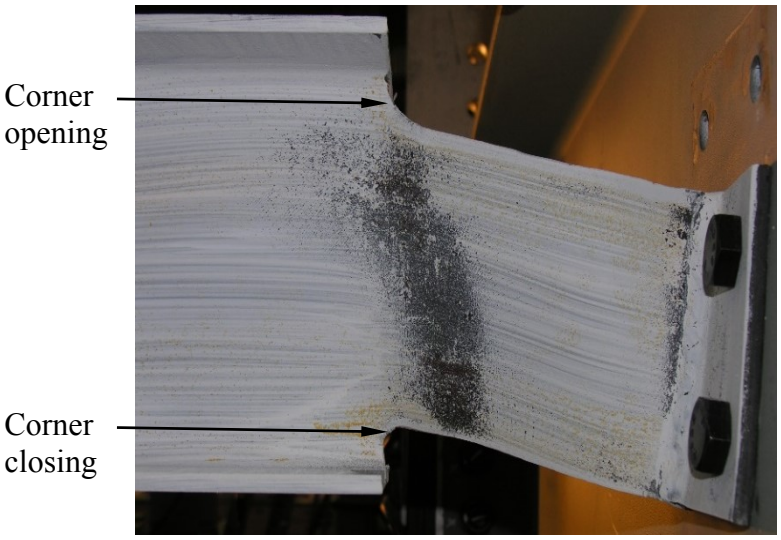

(a)

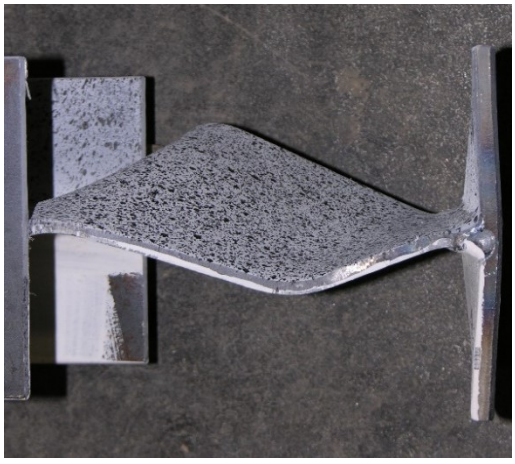

(b)

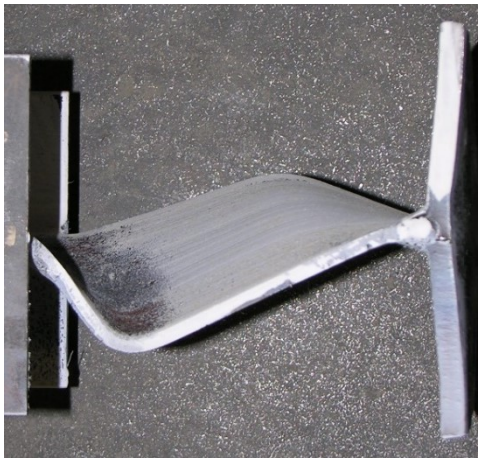

(c)

Figure 4-3: Specimen 2A-3-0-NR deformed shape from (a) side, (b) above, and (c) below

For specimens in the second mode shape, out-of-plane deformation occurred mainly at the lower free edge, with the greatest displacement occurring near the re-entrant corner, as shown in Figure 4-4 for specimen 3A-2-100T-NR. Because the upper edge remained in-plane, some cross-sectional distortion was observed.

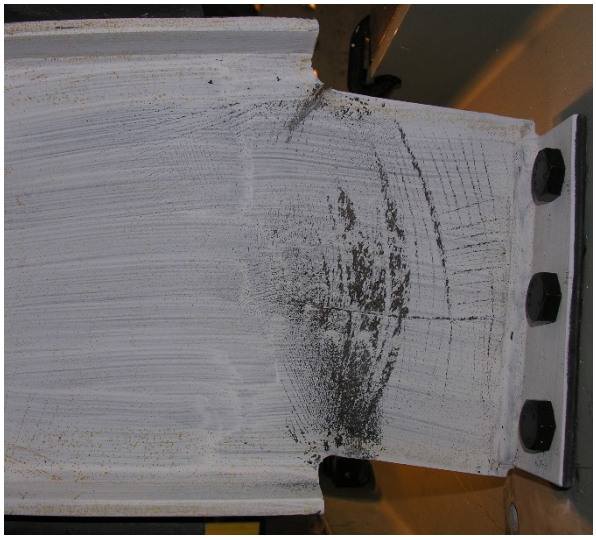

(a)

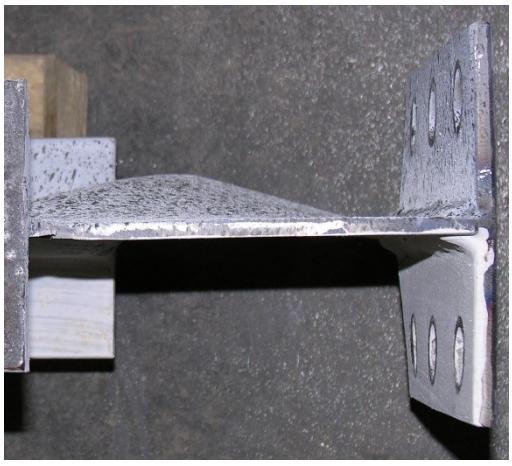

(b)

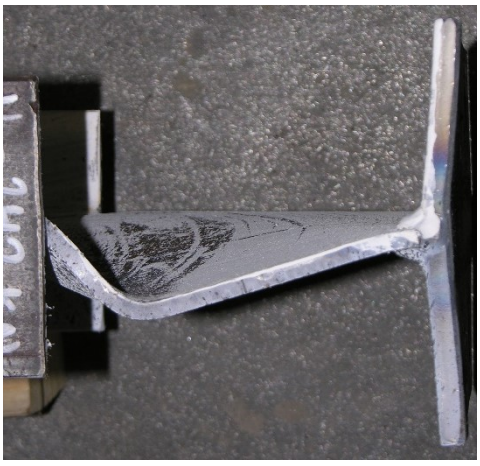

(c)

Figure 4-4: Specimen 3A-2-100T-NR deformed shape from (a) side, (b) above, and (c) below

Specimen 3B-1-200C-R failed by out-of-plane deformation, but the deformed shape could not be characterized by the two distinct mode shapes previously described due to significant distortion of the cross-section in the coped region. The upper and lower free edges of the coped region deformed out-of-plane in the same direction, but the centreline moved in the opposite direction. Some cross-sectional distortion was observed in specimens with other failure modes, but generally occurred after the peak load and more so for specimens with high in-plane restraint.

4.3.2.2 Buckling

In four specimens, two with and two without an applied rotation, the failure was sudden and resulted in large out-of-plane deformation of the cross-section and significant vertical displacement following the peak load. The coped region generally remained planar until the peak load was reached, followed by buckling. The typical response, shown for 4A-3-100T-NR, can be seen in Figure 4-5. Just following the peak, at a vertical load of 436 kN, buckling occurred and the vertical load decreased by 104 kN, or 24%, and the specimen displaced vertically an additional 3.6 mm.

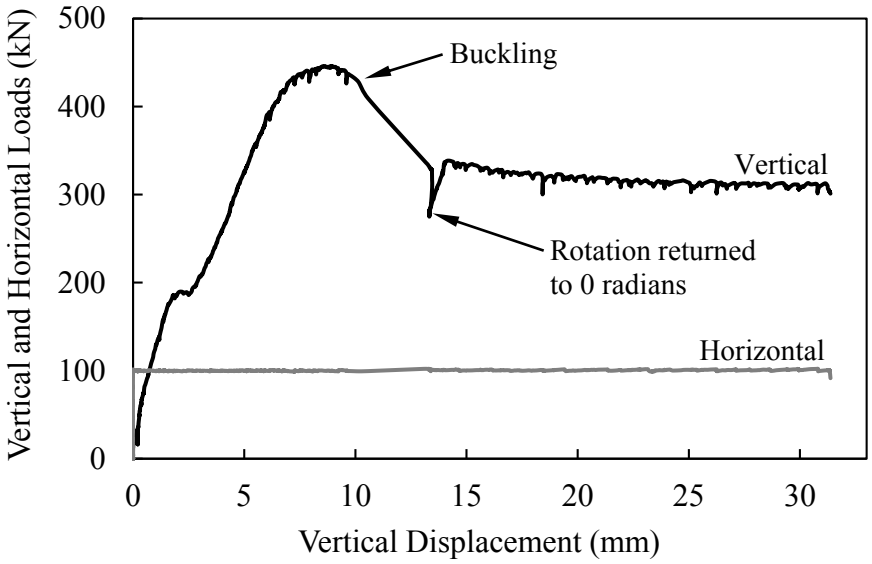

Figure 4-5: Load versus displacement for specimen 4A-3-100T-NR

The buckling failure caused the rotation of the beam to change significantly from the specified value. Following the buckling event, the rotation was returned to the specified value by reducing the vertical load on the specimen, as noted in Figure 4-5. Thereafter, vertical load was reapplied. Specimen 4A-3-100T-NR continued to displace vertically for the remainder of the test with significant post-buckling strength, and the test was stopped following a vertical displacement of 30 mm because there was no evidence that the vertical load would increase. Throughout the vertical loading phase, the buckling failure, and the post-buckling phase, the horizontal load of 100 kN was maintained. The deformed shape of the

coped region, shown in Figure 4-6, was similar to that of 3A-2-100T-NR (Figure 4-4): the upper free edge remained in-plane, and the lower free edge deformed out-of-plane.

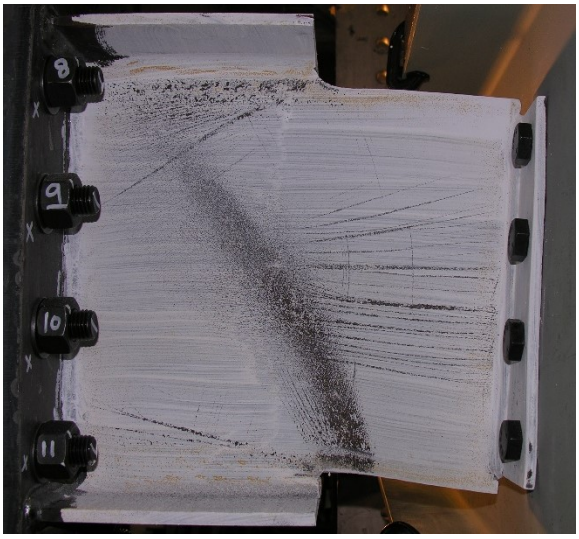

(a)

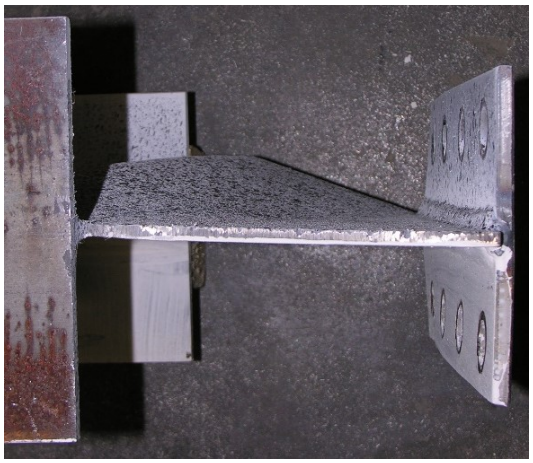

(b)

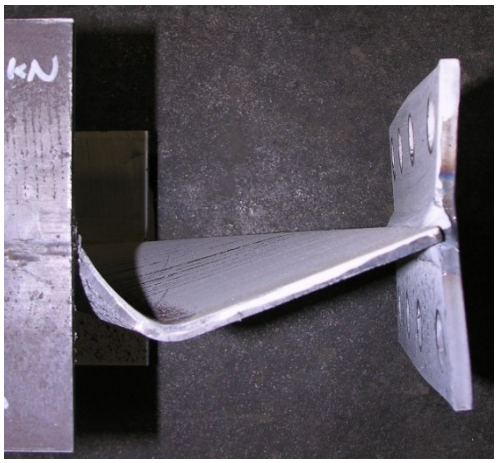

(c)

Figure 4-6: Specimen 4A-3-100T-NR deformed shape from (a) side, (b) above, and (c) below

Buckling failure only occurred in W410×54 specimens, suggesting the larger reduced beam depth and thicker web resisted out-of-plane deformation until a critical limit state was reached. Of the four specimens that buckled, two were subjected to compressive loads, one was subjected to shear only, and one was subjected to tensile load, suggesting that although the horizontal load affected the

magnitude of the peak vertical load, the high shear force or bending demand at the face of the cope were likely the cause of the failure.

4.3.2.3 Tearing

Tearing was eventually observed in more than half of the tests, but was the critical failure mode for specimens 2B-1-100T-R and 2C-1-100T-R only. Tears were observed at up to four locations on each test specimen: at the upper re-entrant corner (either in-plane or out-of-plane tearing, as discussed below), at the lower re-entrant corner (out-of-plane tearing), in the end-plate for end-support B tests, or at the lower free edge of the coped region near the support for end-support C tests.

Tears contributing to the failure of specimens 2B-1-100T-R and 2C-1-100T-R, were at the upper re-entrant corner and occurred in-plane. In-plane tearing only occurred at the upper re-entrant corner due to a 'corner opening' effect, shown in Figure 4-3(a), that resulted in a high tensile stress at this location. The addition of axial tension on the specimen resulted in high localized strains that reached the ultimate tensile strain and caused a sudden rupture that propagated into the uncoped web of the specimen in increments after load had built-up at an angle of approximately 45°. With the exception of specimens 2B-1-100T-R and 2C-1-100T-R, in-plane tears formed following the peak vertical load. An in-plane tear at the upper re-entrant corner of 3A-2-100T-NR is shown in Figure 4-7.

Figure 4-7: In-plane tear in specimen 3A-2-100T-NR

Out-of-plane tears, such as the one shown in Figure 4-8, formed at the upper or lower (or both) re-entrant corners due to the relative out-of-plane deformations of the coped region and the beam flanges, and always formed after the peak vertical load when the out-of-plane displacement of the coped region was large. Tearing from out-of-plane deformation always began at the re-entrant corners and remained parallel to the flange as it propagated into the uncoped web. The tear propagation was always proportional to the rate of out-of-plane deformation of the section, i.e., as vertical displacement was added to the specimen, the out-of-plane deformation of the coped region would increase, resulting in a small increase in the tear length. The formation of this type of tearing was due to the relative out-of-plane stiffness of the flanges and the coped region. As the coped region deformed out-of-plane, the beam flanges resisted this movement due to their high out-of-plane stiffness, resulting in a tear at this location.

Figure 4-8: Out-of-plane tear in specimen 4B-3-300C-R

In addition to tearing at the re-entrant corners, tearing was also observed at the connection to the support, either in the end-plate or in the coped region adjacent to the weld. Tearing at the connection to the support was only observed for specimens with end-support B or C because of the effect of in-plane restraint on the behaviour of the specimen during rotation. As discussed previously, the end rotation of specimens with a rotationally flexible support (end-support A or D) largely comes from the girder, where the end-plate, if present, remains mostly in contact with the

girder web. In comparison, end rotation of specimens with a rigid support (end-support B or C) is achieved through bending and yielding of the coped region, and bending of the end-plate. Because the lower free edge of the coped region at the support was subjected to tension when moment developed at the support, the end-plate is pulled away from the column flange. During the vertical load phase, large vertical displacements of the specimen caused further tensile demand on the end-plate at this location. Resulting vertical tears that formed in the end-plate at the weld toe, as shown in Figure 4-9(a) for specimen 4B-3-300C-R, were not uncommon. Specimens without end-plates that could not accommodate this deformation began to tear at the lower free edge of the coped region at the weld toe, as shown in Figure 4-9(b) for specimen 2C-1-100C-R. Both of these types of tearing occurred well after the peak load under high vertical displacements, and are therefore not the critical failure mode.

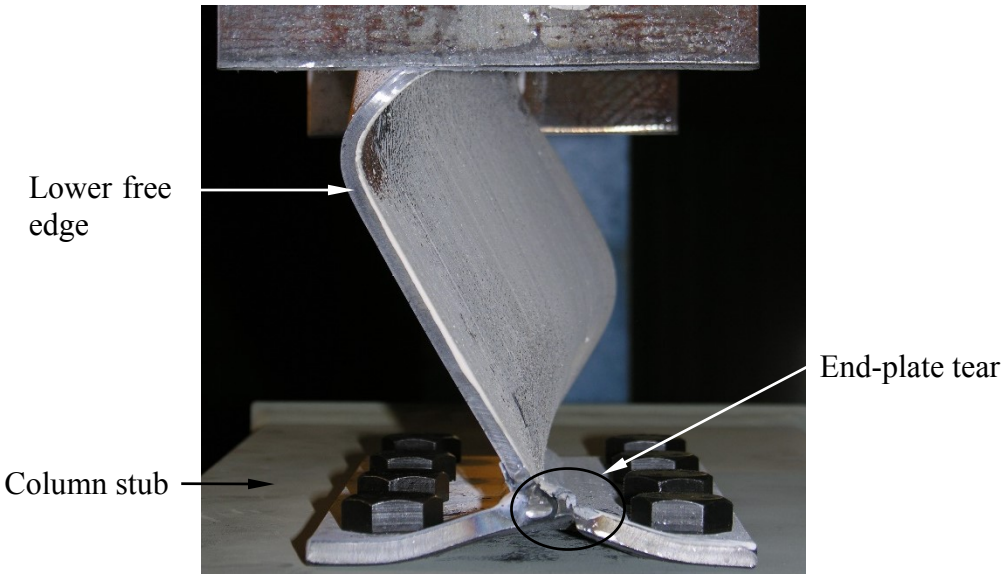

(a)

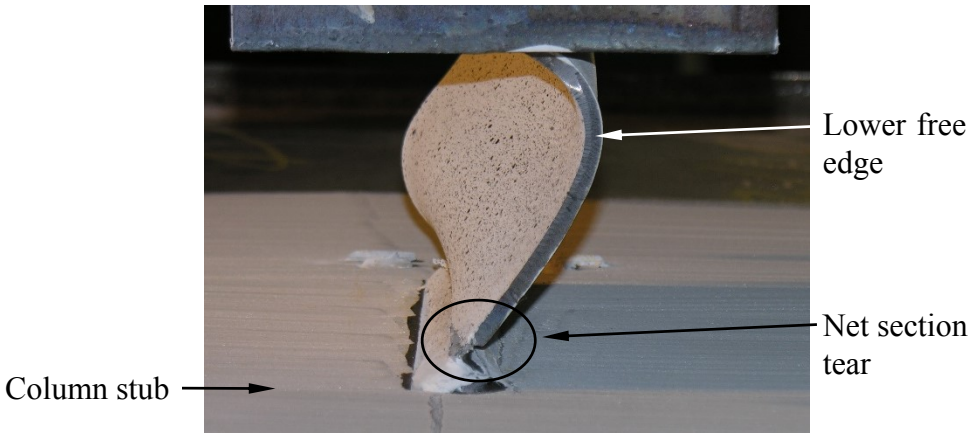

(b)

Figure 4-9: Tears at support for specimens (a) 4B-3-300C-R and (b) 2C-1-100C-R

4.3.2.4 Horizontal Load Failure

In contrast to the other critical failure modes characterized by a decrease in the vertical load carrying capacity, five specimens failed due to their inability to maintain the specified compressive load. As discussed at the beginning of Section 4.3.2, coped regions of specimens tested with rotation that were connected to rotationally stiff supports showed signs of local yielding and out-of-plane deformation at the upper free edge prior to the application of horizontal or vertical loads. The application of horizontal loads caused the coped region to deform further out-of-plane due to a second-order effect. One specimen, 4B-2-300C-R, was unable to maintain the specified 300 kN compressive load and it continued to deform axially under an unsuccessful attempt to re-establish the target load. The remainder of the test was completed at a compressive load of 275 kN, which could be maintained. The other four specimens that failed due to the horizontal loading (2A-1-100C-NR, 2C-1-100C-R, 3C-1-200C-R, and 4B-1-300C-R) could resist the specified load when the vertical load was zero; however, the specimens were unable to carry this load in combination with significant vertical loads. For these four cases, the vertical load–vertical displacement response was approximately linear until the specimen deformed out-of-plane without warning and lost its ability to resist horizontal load. At this point, the horizontal load control was abandoned and the remainder of the test was completed by maintaining the rotation and increasing the vertical load.

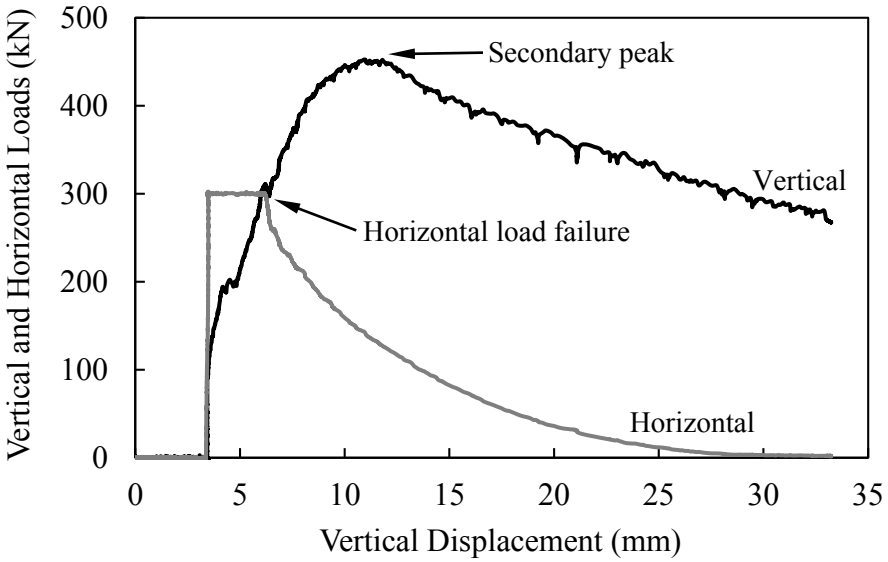

Figure 4-10: Load versus displacement for specimen 4B-1-300C-R

The horizontal load failure of specimen 4B-1-300C-R is shown in the load–displacement relationship in Figure 4-10. At a vertical load of 311 kN, the specified horizontal load of 300 kN decreased and could not be maintained. After the horizontal load control was abandoned, the vertical load was increased to a secondary peak of 453 kN, after which the load decreased gradually until the test was ended. The deformed shape for specimen 4B-1-300C-R is shown in Figure 4-11. Significant yielding is present along a vertical line adjacent to the end-plate, and the cross-section is heavily distorted.

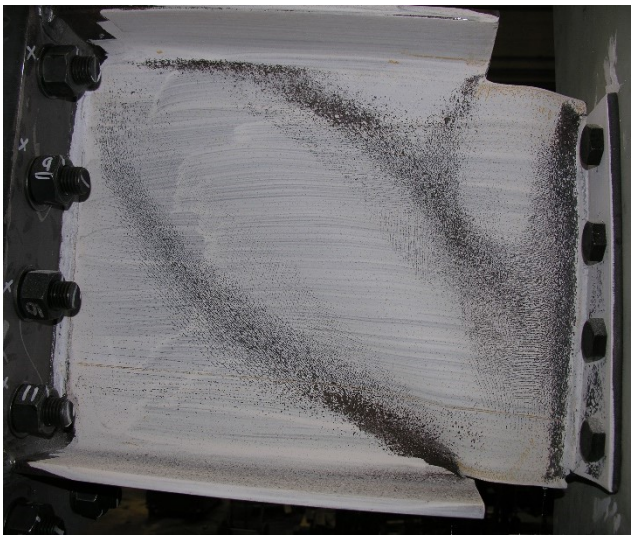

(a)

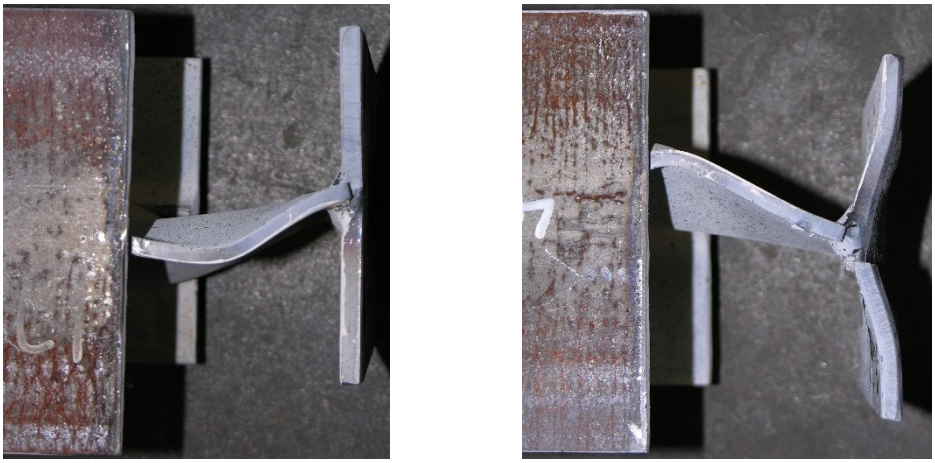

(b) (c)

Figure 4-11: Specimen 4B-1-300C-R deformed shape from (a) side, (b) above, and (c) below

Specimens with the same geometry and testing conditions as 4B-1-300C-R but longer cope lengths, namely, 4B-2-300C-R and 4B-3-300C-R, were able to resist a compressive load much greater than 4B-1-300C-R (4B-2-300C-R resisted 275 kN horizontal load until a peak load of 428 kN, and 4B-3-300C-R resisted the specified 300 kN). High curvature present in specimens with shorter cope lengths caused greater out-of-plane deformations during the rotation phase, so those specimens were more susceptible to second-order effects.

4.4 Moment Distribution

Using the orthogonal components of the force measured from each actuator, and their respective moment arms, the moment at the face of the support was calculated at each load step. By adjusting the moment arms to account for the geometric eccentricity, the moment at the face of the cope (which typically is the location where stresses for buckling are checked) was also calculated. Because shear force is constant over the length of the coped region, the moments at the support and at the cope face create a linear moment distribution, shown in Figure 2-2 for the as-tested orientation of a double-coped beam. The moment sign convention for this research follows the convention typically used for beams by designers: positive moments cause tension in the bottom flange; however, because the test specimen was loaded upwards, this corresponds to the upper free edge of the specimen.

Moments developed at the support during the tests always caused the upper free edge to be under compression, so are considered negative. Moments at the face of the cope may exist in either direction depending on the phase of testing, as described in Section 4.4.1. If the moments at the ends of the coped region have opposite signs, the region is in double curvature and the moments with the greatest magnitudes will be located at the face of the cope ($M_{cope\ face}$) and at the support ($M_{support}$). In the design methods described in Chapter 2, the strength of a coped beam is evaluated at the net section, away from the re-entrant corners, but the moment demand is typically calculated at the face of the cope. Neglecting the material at the re-entrant corners contributes to the conservatism in the methods currently used to design coped beams.

The yield and plastic moments (Equations 2-39 and 2-40), used commonly to evaluate the strength of the cross-section in the coped region, are proportional to $h_0^2 t_w$ and therefore are more sensitive to changes in the reduced beam depth than the web thickness. The radii of the re-entrant corners cause h_0 to increase sharply as the section considered moves from the coped region towards the cope face. For a W310×33 beam with 30 mm cope depths at the top and bottom flanges and 12.7 mm (½ in) re-entrant corner radii, the reduced beam depth, h_0, increases from 253 mm to 278.4 mm, or 10%, between the beginning of the re-entrant corner radius and the face of the cope, while h_0^2 increases by 21%. For similar W200×27 and W410×54 beams, h_0^2 increases by 38% and 15%, respectively. The material at the re-entrant corners contributes significantly to the strength of the cross-section. To assess the strength of the coped region accurately, the moments applied on the net section at the beginning of the re-entrant corner radius should be used.

Similarly, comparing the moment developed at the support, which can be greater than that at the cope face if the rotational stiffness of the support is high, to a moment resistance calculated using the material properties and dimensions of the coped region can be overly conservative. Current design procedures generally assume this moment to be zero; however, the moment at the support is considered explicitly in this research project.

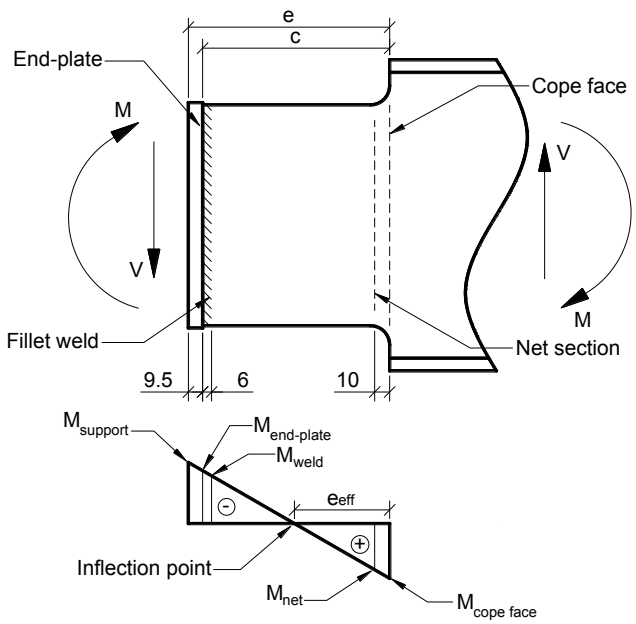

Figure 4-12: Double-coped beam moment distribution (as-tested orientation)

Because the moment distribution in the coped region is linear, the largest moments that act on the true net section (between the end-plate weld toe and the beginning of the re-entrant corners) can be calculated using $M_{support}$ and $M_{cope\ face}$ and the geometric eccentricity, e. As such, the moment at the support was adjusted by 9.5 mm (⅜ in) to account for the thickness of the end-plate, if present, which was the same for all such specimens. $M_{end\text{-}plate}$ was then adjusted further to account for the fillet weld leg size, resulting in M_{weld}. Because the fillet weld leg sizes were not measured, the nominal dimension of 6 mm was chosen because it was observed that the welds were at least equal to this value. At the opposite end, $M_{cope\ face}$ was adjusted to account for the re-entrant corner radii, resulting in M_{net}. The re-entrant radii were not measured, but were observed to have higher variability than the weld sizes. Bearing in mind that smaller adjustment values are conservative from a design perspective, 10 mm was selected as the adjustment dimension for M_{net}.

The various moment–vertical displacement relationships for specimen 3A-2-100T-NR are shown in Figure 4-13. At the peak vertical load, $M_{cope\ face}$, M_{net}, M_{weld}, $M_{end\text{-}plate}$, and $M_{support}$ were equal to 28.3 kN·m, 25.8 kN·m, -6.4 kN·m, -7.9 kN·m, and -10.1 kN·m, respectively, corresponding to

moment reductions between the support and the weld toe of 36.6% and between the cope face and the net section of 8.8%.

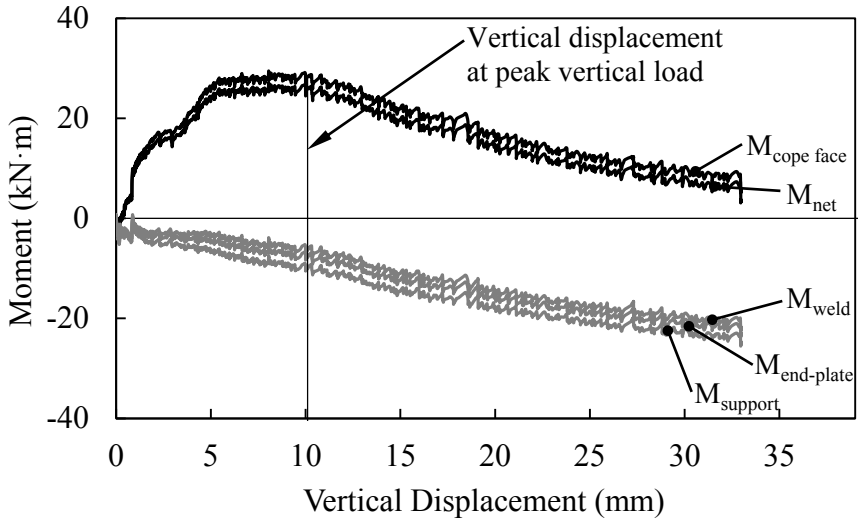

Figure 4-13: Moment versus displacement for specimen 3A-2-100T-NR

As the vertical displacement increases, the moments at the ends of the coped region redistribute. Except for the four specimens tested with applied tensile load (e.g., Figure 4-13), the magnitudes of M_{net} and M_{weld} never increase at the same time (see Figure 4-14 for a typical case). Typically, if the moment magnitude at one end of the coped region is increasing, the magnitude at the opposite end is decreasing. Note that the point when either M_{net} or M_{weld} reaches its maximum magnitude does not necessarily correspond to the peak vertical load, and the maximum magnitudes of M_{net} and M_{weld} don't occur at the same time. Moment versus displacement curves for all tests can be found in Appendix C.

4.4.1 Effect of Rotation on Moment Distribution

The development of moment at the support, and therefore at the weld toe, is directly related to the end-support condition and the applied rotation. For specimens tested without rotation, moment at the support developed gradually during the application of vertical load (see Figure 4-13). In the beginning of the vertical load phase, the magnitude of M_{weld} often remained relatively low, and depended on the relative stiffnesses of the coped region, the supporting girder, and the connection to the support. After the maximum value of M_{net} had been reached, the magnitude of M_{weld}

would increase. At high vertical displacements, the coped region of the specimen would be steeply inclined relative to the beam flanges (see Figure 4-3(a)). As the bottom row of bolts pulled on the girder web, M_{weld} would increase until the test was ended. For specimens tested with rotation, the moment distribution was very different, as shown in Figure 4-14 for specimen 2B-3-0-R.

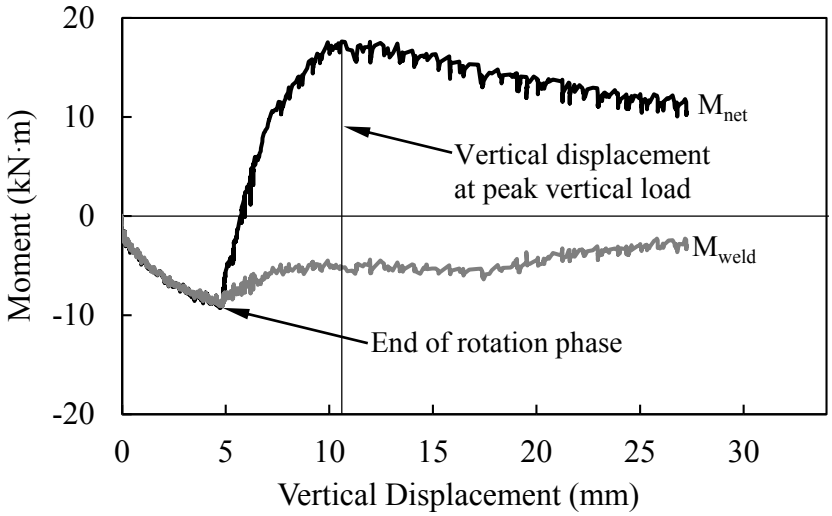

Figure 4-14: Moment versus displacement for specimen 2B-3-0-R

To achieve the specified rotation, moment was applied to the test specimen while the vertical and horizontal loads were kept at or near zero, resulting in a near-constant moment over the coped region, which was therefore in single curvature with the upper and lower free edges in compression and tension, respectively. The magnitude of moment at the end of the rotation phase depended on the geometry of the coped region and the rotational stiffness of the support. It was not uncommon for the largest moments during the entire test to occur at the end of the rotation phase. The application of horizontal load had only a small effect on the moment distribution in the coped region because the line of action of Actuator 3 passed approximately through the centerline of the beam. Following the rotation and horizontal loading phases, the application of vertical load typically caused M_{net} to reduce to zero, change direction, and increase to put the coped region into double curvature (see Figure 4-14).

4.4.2 Effective Eccentricity

The linear moment distribution was also used to determine the effective eccentricity, e_{eff}, which is defined as the distance from the face of the cope to the point of inflection (see Figure 2-2). The redistribution of moments in the coped region during the application of vertical load means the location of the inflection point moves, and therefore the effective eccentricity is not a single value; rather, it varies continuously throughout the loading history.

The evolution of the ratio of the effective eccentricity, e_{eff}, to the geometric eccentricity, e, is shown in Figure 4-15 for specimen 2B-3-0-R. During the rotation phase, the moment in the coped region is constant, and therefore the effective eccentricity has no meaningful value. At the completion of the rotation phase and the beginning of the vertical load phase, while M_{net} is still negative (Figure 4-14), e_{eff}/e is also negative, i.e., the point of inflection is located in the uncoped section of the beam. Once M_{net} becomes positive and the coped region is in double curvature, the inflection point moves quickly into the coped region where it remains for the remainder of the test. At the peak vertical load, $e_{eff}/e = 0.72$ for specimen 2B-3-0-R.

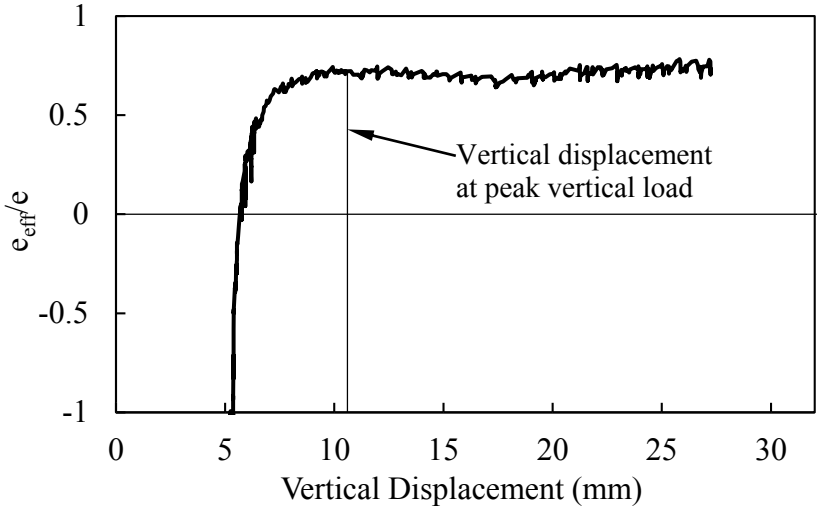

Figure 4-15: Ratio of e_{eff}/e versus displacement for specimen 2B-3-0-R

All specimens tested with rotation had e_{eff}/e less than zero during the rotation phase and at the initiation of vertical load. Specimens tested without rotation typically

began with high positive e_{eff}/e values due to the early increase in M_{net} compared to M_{weld}. Curves showing the ratio of e_{eff}/e versus vertical displacement for all tests can be found in Appendix C.

4.5 Discussion of Results

4.5.1 Cross-sectional Strength

Table 4-2 shows a summary of strength ratios for the 29 full-scale double-coped beam tests at the peak vertical load. The peak shear is compared to the elastic and plastic shear strengths (Equations 2-37 and 2-38) using 0.6 instead of the 0.577 factor obtained from the von Mises yield criterion, in accordance with the AISC *Specification* (AISC 2010), and the values of M_{net} and M_{weld} are compared to both the yield, M_y, and plastic, M_p, moments (Equations 2-39 and 2-40). All strength calculations used the as-built specimen dimensions and material properties. For specimens that failed due to horizontal load, values for both the peak vertical load with the specified horizontal force present and the secondary peak load are shown.

At the peak vertical load, the elastic shear strength, V_y, was exceeded by 14 specimens—typically with shorter cope lengths. With the exception of 2A-1-100C-NR, all specimens that failed due to horizontal load reached the elastic shear strength at the secondary peak load. The plastic shear strength, V_p, was only exceeded by 2C-1-100T-R. It is likely that although the ratio of c/h_0 was low for many specimens, the bending effect still dominates the strength for the geometries tested. However, all specimens except 2A-1-100C-NR reached at least 73% of V_y (49% of V_p), suggesting that although the coped regions were dominated by bending, they were also under high shear stress that could have affected the ability of the cross-section to reach its plastic moment.

At the net section, the moment at the peak vertical load exceeded the yield moment in 15 specimens, typically with long cope lengths, and the plastic moment was reached in only three specimens. At the weld, the moments at the peak load were highly variable due to the different end-support stiffnesses. Six specimens reached their yield moment, but no specimens reached the plastic moment. No specimen for

which M_{weld}/M_y exceeded 1.0 also had M_{net}/M_y greater than 1.0 at the peak vertical load.

Table 4-2: Summary of shear and moment ratios at peak vertical load

Specimen ID	V/V_y	V/V_p	M_{net}/M_y	M_{net}/M_p	M_{weld}/M_y	M_{weld}/M_p
2A-1-0-R	1.39	0.92	0.98	0.66	0.92	0.62
2A-1-0-NR	1.19	0.79	1.05	0.70	0.57	0.38
2A-1-100C-R	1.02	0.68	1.13	0.76	0.32	0.22
2A-1-100C-NR	0.64 / 0.86	0.43 / 0.57	0.89 / 0.57	0.59 / 0.38	0.02 / 0.65	0.01 / 0.43
2A-2-0-R	0.92	0.61	0.75	0.50	1.22	0.81
2A-2-0-NR	0.83	0.55	0.65	0.44	1.20	0.80
2A-3-0-R	0.73	0.49	0.56	0.37	1.32	0.88
2A-3-0-NR	0.76	0.51	0.70	0.47	1.31	0.87
2B-1-100T-R	1.46	0.98	1.66	1.11	0.28	0.19
2B-1-100C-R	1.29	0.86	1.40	0.93	0.32	0.22
2B-3-0-R	1.09	0.73	2.20	1.46	0.65	0.43
2C-1-100T-R	1.65	1.10	1.02	0.68	1.12	0.75
2C-1-100C-R	0.91 / 1.32	0.61 / 0.88	0.89 / 1.79	0.59 / 1.19	0.29 / 0.08	0.19 / 0.05
2D-2-0-NR	0.88	0.59	1.94	1.29	0.05	0.04
3A-1-100C-NR	1.13	0.75	1.13	0.76	0.20	0.14
3A-2-100T-NR	1.04	0.70	1.05	0.70	0.26	0.17
3A-2-0-NR	0.92	0.61	1.29	0.86	0.14	0.09
3A-2-100C-NR	0.82	0.55	1.14	0.76	0.08	0.05
3A-3-0-NR	0.87	0.58	1.47	0.98	0.13	0.09
3A-3-100C-NR	0.79	0.53	1.19	0.79	0.03	0.02
3B-1-200C-R	1.27	0.85	0.03	0.02	1.05	0.70
3C-1-200C-R	0.90 / 1.31	0.60 / 0.88	0.28 / 0.20	0.19 / 0.14	0.99 / 0.83	0.66 / 0.56
3D-2-0-NR	0.98	0.65	0.91	0.61	0.15	0.10
4A-3-100T-NR	1.13	0.75	1.16	0.77	0.11	0.07
4A-3-0-NR	1.09	0.72	1.38	0.92	0.16	0.11
4B-1-300C-R	0.80 / 1.17	0.53 / 0.78	0.39 / 0.61	0.26 / 0.40	0.08 / 0.08	0.05 / 0.06
4B-2-200C-R	1.25	0.83	0.54	0.36	0.62	0.42
4B-2-300C-R†	1.09	0.73	0.18	0.12	0.83	0.55
4B-3-300C-R	0.95	0.63	0.12	0.08	0.95	0.63

† Peak vertical load reached at 275 kN horizontal load (refer to Section 4.3.2.4)

As stated previously, M_{net} and M_{weld} at the peak vertical load were not necessarily the maximum moments experienced by the net section due to the moment

redistribution in the coped region. For specimens tested with rotation, the moments developed at 0.03 radians may have been the maxima. For other specimens, the maximum moments may have occurred sometime during the vertical load phase, and not necessarily at the peak vertical load. Table 4-3 summarizes the maximum ratios of M_{net} and M_{weld} to the plastic moment of the net section both at the end of the rotation phase (at 0.03 radians) and during the vertical loading. For specimens that failed under horizontal load, the first value is the maximum during the phase of vertical loading up to the horizontal load failure, and the second value is the maximum value during the phase of vertical loading after the horizontal load control had been abandoned.

The moments developed in the coped region during the rotation phase were significant. Two specimens (3B-1-200C-R and 4B-3-300C-R) exceeded their plastic moment during rotation, prior to the addition of any horizontal or vertical load to the specimen, and four specimens (2B-1-100C-R, 2C-1-100T-R, 3C-1-200C-R, and 4B-2-300C-R) experienced moments within 10% of the plastic moment. Of the 15 specimens tested with rotation, only six developed moments at the end of the rotation phase that were less than $M_y = 0.67M_p$ at both the net section and the weld, meaning nine specimens had yielded during rotation. All four specimens with end-support A, which was rotationally flexible, developed moments less than $0.67M_p$ during rotation at both locations.

During the vertical load phase, 11 specimens reached moments within 5% of M_p (or greater) at either the net section or at the weld location. Because the specimens were loaded upwards, the rotation phase always subjected the entire coped region to negative moments; however, under vertical load, moment at the net section at the beginning of the re-entrant corners was typically positive. Four specimens (2B-1-100T-R, 2B-1-100C-R, 2B-3-0-R, and 2C-1-100T-R) reached $M_{net} \geq 0.67M_p$ at the end of the rotation phase under negative bending, and then reached $M_{net} \geq 0.72M_p$ during the vertical load phase under positive bending, exhibiting a complete reversal of inelastic bending.

Table 4-3: Summary of moment ratios after rotation and during vertical load

	At 0.03 radians		During vertical load	
Specimen ID	M_{net}/M_p	M_{weld}/M_p	$M_{net,max}/M_p$	$M_{weld,max}/M_p$
2A-1-0-R	0.66	0.66	0.80	0.89
2A-1-0-NR	–	–	1.06	0.53
2A-1-100C-R	0.45	0.45	0.85	0.94
2A-1-100C-NR	–	–	0.62 / 0.44	0.84 / 1.00
2A-2-0-R	0.38	0.38	0.93	0.99
2A-2-0-NR	–	–	0.90	0.97
2A-3-0-R	0.36	0.37	0.91	0.96
2A-3-0-NR	–	–	0.97	0.95
2B-1-100T-R	0.68	0.66	1.22	0.39
2B-1-100C-R	0.90	0.88	0.97	0.69
2B-3-0-R	0.76	0.75	1.46	0.53
2C-1-100T-R	0.90	0.89	0.72	0.86
2C-1-100C-R	0.57	0.57	0.83 / 1.32	0.33 / 0.29
2D-2-0-NR	–	–	1.33	0.43
3A-1-100C-NR	–	–	0.77	0.30
3A-2-100T-NR	–	–	0.74	0.61
3A-2-0-NR	–	–	0.86	0.50
3A-2-100C-NR	–	–	0.77	0.40
3A-3-0-NR	–	–	1.01	0.38
3A-3-100C-NR	–	–	0.80	0.41
3B-1-200C-R	1.10	1.09	0.04	1.07
3C-1-200C-R	0.98	0.98	0.01 / 0.16	0.74 / 0.66
3D-2-0-NR	–	–	0.62	0.13
4A-3-0-NR	–	–	0.80	0.27
4A-3-100T-NR	–	–	0.92	0.15
4B-1-300C-R	0.47	0.47	0.39 / 0.45	0.15 / 0.19
4B-2-200C-R	0.85	0.85	0.37	0.68
4B-2-300C-R	0.93	0.93	0.12	0.61
4B-3-300C-R	1.05	1.05	0.08	0.80

The presence of yielding observed in all tests due to flaking whitewash was affirmed by the shear and moment ratios. Except specimens 3D-2-0-NR and 4B-3-300C-R, all of the test specimens that failed due to vertical load reached either V_y or M_y, or both, in the coped region at the peak vertical load. Specimen

3D-2-0-NR reached 98% of V_y at the peak vertical load, which could be considered within an appropriate margin of error for the measured dimensions and material properties, and 4B-3-300C-R reached the plastic moment during the rotation phase. Of the five specimens that failed due to horizontal load, three specimens (2A-1-100C-NR, 2C-1-100C-R, and 3C-1-200C-R) reached M_y at one end of the coped region during the phase of vertical loading in which the primary peak load was reached. Specimen 4B-2-300C-R, which was able to maintain 275 kN horizontal load until the peak vertical load, reached M_y during the rotation phase, and V_y at the peak vertical load, and specimen 4B-1-300C-R only reached V_y after the primary peak vertical load had been reached, during the phase of the test that horizontal load was uncontrolled.

4.5.2 Effects of Variables

The 29 double-coped beam specimens varied by section depth (and web thickness), cope length, axial load, end rotation, and end-support, as discussed in Chapter 3. The effects of these key variables on the specimen capacity, ductility, and effective eccentricity at the peak vertical load are discussed in the following sections. Several direct comparisons are made for each variable, wherein all other variables are unchanged. Because the specimens were not all fabricated from the same material, the measured beam web yield strengths are also reported for reference.

4.5.2.1 Section Depth

The depth of the section determined two parameters in the coped region geometry: the reduced beam depth and the web thickness. Three sections were tested: W200×27, W310×33, and W410×54, which correspond to reduced beam depths of 147 mm, 253 mm, and 343 mm, respectively. Four comparisons, shown in Table 4-4, are made between the tested specimens to study the effect of the section depth.

Table 4-4: Effect of section depth at peak vertical load

Specimen ID	Yield Strength (MPa)	Peak Vertical Load (kN)	Vertical Displacement (mm)	e_{eff}/e
2A-2-0-NR	376	110	29.4	0.36
3A-2-0-NR	355	207	4.5	1.00
2D-2-0-NR	362	105	6.8	0.99
3D-2-0-NR	355	235	5.6	1.11
2A-3-0-NR	376	99	34.4	0.36
3A-3-0-NR	355	199	5.4	1.01
4A-3-0-NR	434	443	6.9	1.03
2A-1-100C-NR	376	83 / 112	1.2 / 29.8	0.85 / 0.45
3A-1-100C-NR	355	260	5.7	1.04

As expected, heavier sections increased the strength of the connection due to the greater cross-sectional depth and thickness: specimens 3A-2-0-NR and 3A-3-0-NR had peak vertical loads 97 kN, or 88%, and 100 kN, or 102%, greater than specimens 2A-2-0-NR and 2A-3-0-NR, respectively, noting that in both cases the specimen with greater depth had a slightly lower yield strength. This effect was amplified for end-support D: 3D-2-0-NR had a peak vertical load 129 kN, or 123% greater than 2D-2-0-NR. The vertical displacement at the peak vertical load tended to decrease for deeper specimens, and in some cases substantially; however, 4A-3-0-NR had slightly greater vertical displacement compared to the specimen one beam section shallower. The trend of the ratio e_{eff}/e was the same as that of the peak vertical load—deeper specimens always had higher effective eccentricities. All of the W310×33 and W410×54 specimens in this comparison had e_{eff}/e approximately equal to 1.0, meaning that the moment at the support was near zero at the peak vertical load. The W200×27 in this comparison that had end-support D also had e_{eff}/e approximately equal to 1.0, whereas the others had values much lower, indicating the strong influence on this ratio of the rotational stiffness at the support.

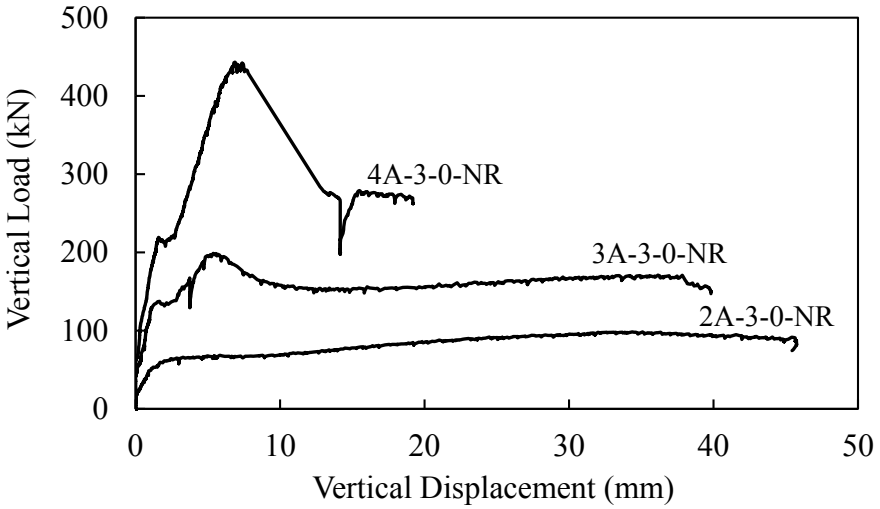

Figure 4-16: Effect of section depth on connection behaviour

Figure 4-16 shows the effect of section depth on the connection behaviour for three specimens with 175 mm cope lengths, connected to the reusable girder by means of an end-plate, and tested without axial load or rotation. The behaviours of specimens 2A-3-0-NR, 3A-3-0-NR, and 4A-3-0-NR are notably different due to the cope-length-to-reduced-beam-depth ratios, c/h_0, which were 1.21, 0.70, and 0.51, respectively. Specimen 4A-3-0-NR was 123% stronger than 3A-3-0-NR, which was in turn 102% stronger than 2A-3-0-NR, but the vertical displacement at the peak vertical load of specimen 3A-3-0-NR was 84% less than that of 2A-3-0-NR.

4.5.2.2 Cope Length

Three cope lengths were tested: 100 mm, 150 mm, and 175 mm. The cope length dictates the distance between the support and the face of the cope, and therefore the moment demand on the net section. Additionally, the cope length is a key parameter in determining the connection behaviour, which is influenced by the ratio of c/h_0. Five groups of specimens, each with varying cope lengths, are compared in Table 4-5.

Table 4-5: Effect of cope length at peak vertical load

Specimen ID	Yield Strength (MPa)	Peak Vertical Load (kN)	Vertical Displacement (mm)	e_{eff}/e
2A-1-0-R	362	173	15.3	0.49
2A-2-0-R	362	111	19.6	0.38
2A-3-0-R	362	89	20.7	0.31
2A-1-0-NR	362	149	26.8	0.59
2A-2-0-NR	376	110	29.4	0.36
2A-3-0-NR	376	99	34.4	0.36
3A-2-0-NR	355	242	10.1	0.74
3A-3-0-NR	355	199	5.4	1.01
3A-1-100C-NR	355	260	5.7	1.04
3A-2-100C-NR	355	191	2.0	0.96
3A-3-100C-NR	355	182	3.5	0.90
4B-1-300C-R	396	311 / 453	2.9 / 7.6	0.73 / 0.77
4B-2-300C-R	396	428	4.8	0.21
4B-3-300C-R	396	360	5.7	0.15

As expected, specimens with longer cope lengths had lower capacities than specimens with shorter cope lengths, except 4B-1-300C-R, which failed due to horizontal load. For the six W200×27 specimens shown in Table 4-5, longer cope lengths also resulted in greater vertical displacements and lower e_{eff}/e ratios at the peak vertical load. Specimen 2A-1-0-R had a peak vertical load that was 62 kN, or 56%, greater than 2A-2-0-R and 84 kN, or 95%, greater than 2A-3-0-R; however, this effect was reduced when a similar group was tested without rotation. Specimen 2A-1-0-NR had a peak vertical load that was 36% and 52% greater than those for 2A-2-0-NR and 2A-3-0-NR, respectively.

Figure 4-17 shows the effect of cope length on the specimen behaviour for 2A-1-0-R, 2A-2-0-R, and 2A-3-0-R. The effect of the increased capacity for specimens with short cope lengths also reduced as the specimen depth increased. The capacity of specimen 3A-2-0-NR was 43 kN, or 22%, greater than that of 3A-3-0-NR, and 3A-2-0-NR had greater displacement at the peak vertical load.

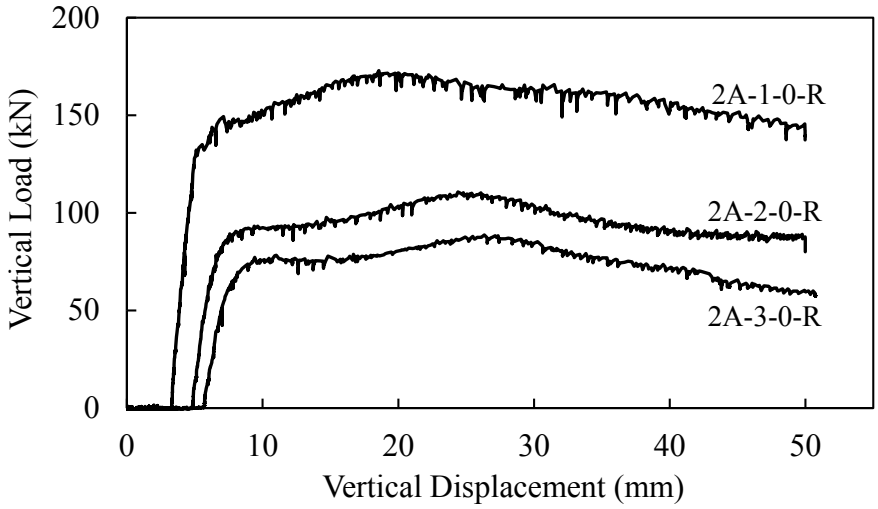

Figure 4-17: Effect of cope length on connection behaviour

Under compressive loads, the peak vertical load of 3A-2-100C-NR was only 5% greater than that of 3A-3-100C-NR, and the displacement at the peak vertical load for both specimens was low compared to similar specimens tested without compression. Generally, shorter cope lengths produced greater e_{eff}/e ratios: specimens 2A-1-0-R and 2A-1-0-NR had ratios of e_{eff}/e 29% and 64% greater, respectively, than that of the specimen with the next longer cope length (2A-2). This effect decreased for longer cope lengths: specimen 2A-2-0-R had an e_{eff}/e ratio 23% greater than that of 2A-3-0-R, and specimens 2A-2-0-NR and 2A-3-0-NR had the same e_{eff}/e ratio at the peak vertical load.

4.5.2.3 Axial Load

Test specimens were subjected to axial loads between 100 kN in tension and 300 kN in compression. Specimens tested in shear only provide a comparison to determine possible stabilizing effects for specimens loaded in tension, or destabilizing effects for those loaded in compression. Eight comparisons on the effect of axial load are made in Table 4-6.

Table 4-6: Effect of axial load at peak vertical load

Specimen ID	Yield Strength (MPa)	Peak Vertical Load (kN)	Vertical Displacement (mm)	e_{eff}/e
2B-1-100T-R	359	186	16.8	0.79
2B-1-100C-R	359	162	8.2	0.71
2C-1-100T-R	359	208	21.0	0.50
2C-1-100C-R	359	114 / 166	1.3 / 10.0	0.73 / 0.98
2A-1-0-R	362	173	15.3	0.49
2A-1-100C-R	376	133	7.4	0.69
2A-1-0-NR	362	149	26.8	0.59
2A-1-100C-NR	376	83 / 112	1.2 / 29.8	0.85 / 0.45
3A-2-100T-NR	355	242	10.1	0.74
3A-2-0-NR	355	207	4.5	1.00
3A-2-100C-NR	355	191	2.0	0.96
3A-3-0-NR	355	199	5.4	1.01
3A-3-100C-NR	355	182	3.5	0.90
4B-2-200C-R	396	479	9.4	0.45
4B-2-300C-R	396	428	4.8	0.21
4A-3-100T-NR	434	446	8.6	0.84
4A-3-0-NR	434	443	6.9	1.03

Specimens loaded in tension always had higher peak vertical loads than specimens loaded in shear only or in compression. Similarly, specimens loaded in compression always had lower peak vertical loads than specimens loaded in shear only. The effect of axial load depended on the axial resistance ratio (P/P_y): specimen 2A-1-0-R had a peak vertical load 40 kN, or 30%, greater than that of specimen 2A-1-100C-R, which had $P/P_y = 0.31$, whereas specimen 3A-3-0-NR was only 17 kN, or 9%, stronger than specimen 3A-3-100C-NR ($P/P_y = 0.17$). Similarly, specimen 3A-2-100T-NR ($P/P_y = 0.17$) had a peak vertical load 36 kN, or 17%, greater than that of 3A-2-0-NR, while the peak vertical load for 4A-3-100T-NR ($P/P_y = 0.10$) was only 1% greater than that of 4A-3-0-NR. The effect of tensile load increasing the vertical load capacity appears to reduce for deeper sections (shown above); however, the cope lengths for these specimens are also different, so the effect is somewhat unclear. The effect of compression on the two longer cope

lengths—seen by comparing specimens 3A-2-0-NR and 3A-2-100C-NR to specimens 3A-3-0-NR and 3A-3-100C-NR—was small. The specimen tested without compression was 8% stronger when the specified cope length was 150 mm, and 9% stronger when the specified cope length was 175 mm. Contrary to the effects of section depth and cope length, increased vertical load capacity from applied tensile loads (or shear only compared to compressive loads) resulted in greater vertical displacement at the peak load.

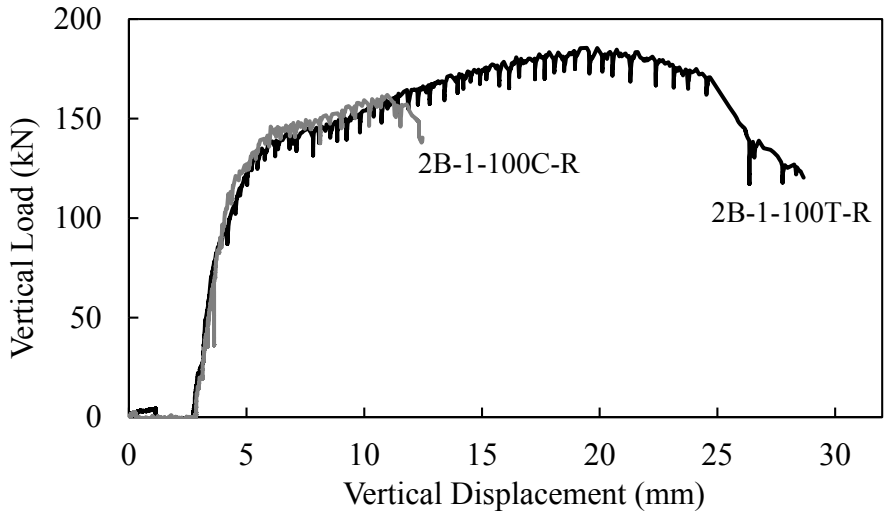

Figure 4-18: Effect of axial load on connection behaviour

The stabilizing and destabilizing effects from tension and compression, respectively, can be seen in Figure 4-18 for specimens 2B-1-100C-R and 2B-1-100T-R. The vertical load–vertical displacement relationships for the two specimens match closely until the failure of specimen 2B-1-100C-R at a peak vertical load of 162 kN and an adjusted vertical displacement of 8.2 mm. Specimen 2B-1-100T-R, stabilized by the applied tensile load, had a 24 kN, or 15%, greater peak vertical load and a 104% greater vertical displacement compared to specimen 2B-1-100C-R.

4.5.2.4 End Rotation

Specimens were tested at either 0 radians (NR) or 0.03 radians (R) to investigate the effect of end rotation. The rotations selected were considered to be reasonable

lower and upper bounds for typical beam end conditions. The effect of end rotation at the peak vertical load is shown in Table 4-7 for four specimen pairings.

Table 4-7: Effect of end rotation at peak vertical load

Specimen ID	Yield Strength (MPa)	Peak Vertical Load (kN)	Vertical Displacement (mm)	e_{eff}/e
2A-1-0-R	362	173	15.3	0.49
2A-1-0-NR	362	149	26.8	0.59
2A-2-0-R	362	111	19.6	0.38
2A-2-0-NR	376	110	29.4	0.36
2A-3-0-R	362	89	20.7	0.31
2A-3-0-NR	376	99	34.4	0.36
2A-1-100C-R	376	133	7.4	0.69
2A-1-100C-NR	376	83 / 112	1.2 / 29.8	0.85 / 0.45

In general, specimens tested without rotation had lower peak vertical loads than specimens tested with rotation. For the comparisons made in Table 4-7, which all have end-support A, the out-of-plane deformation of the coped region always began at the lower free edge due to compressive stresses at the re-entrant corner. By forcing the beam flanges to remain at zero rotation, compressive stresses at this critical location were increased and the specimen capacity was reduced. The two specimens with 150 mm cope lengths had peak vertical loads within 1 kN, but also had different material properties, so the effect of the end rotation may have actually been slightly greater. Contrary to this trend, 2A-3-0-NR had a peak vertical load 10 kN or 11% greater than 2A-3-0-R, but this difference may actually be lower based on the different material yield strengths. In any case, it would appear that the effect of end rotation on the peak vertical load is greatest for shorter copes, and for these, the case of no rotation is more severe. Specimens tested without rotation always had greater vertical displacements at the peak vertical load than specimens tested with rotation, except for 2A-1-100C-NR, which failed due to horizontal load in the linear region of the vertical load–vertical displacement relationship. Figure 4-1 shows the effects of end rotation on the behaviour of 2A-1-0-R and 2A-1-0-NR. The peak vertical load of 2A-1-0-NR was 14% less than that of 2A-1-0-R, but the vertical displacement was 75% greater. End rotation generally

had little effect on the ratio of e_{eff}/e, which mainly depends on the relative stiffnesses of the coped region and the supporting girder (similar for all specimens in Table 4-7). Specimen groups with longer cope lengths (2A-2 and 2A-3) had markedly lower e_{eff}/e ratios than those with shorter cope lengths (2A-1) at the peak vertical load, and the greatest effect of rotation on the e_{eff}/e ratio was approximately 20% for specimens 2A-1-0-R and 2A-1-0-NR, and for specimens 2A-1-100C-R and 2A-1-100C-NR.

4.5.2.5 End-support

Four end-supports were used in this research program to represent support types with different rotational stiffness. End-supports A and D were rotationally flexible girders, and end-supports B and C were rotationally stiff column flanges. End-plates were provided for end-supports A and B, and specimens with end-support C or D were welded directly to their supporting member. End-support A tests used a W530×92 girder, and end-support D tests used girders approximately equal in depth to the specimen being tested (W200×36 for 2D-2-0-NR, and W310×39 for 3D-2-0-NR). Six groups of specimens comparing the effect of end-support at the peak vertical load are shown in Table 4-8.

The rotational stiffness of the end-support has a significant effect on the strength of a double-coped beam. If the support has low stiffness and low or no moment develops, the moment at the face of the cope will be high. If the support is rotationally stiff, the moment that develops decreases the magnitude of the moment at the face of the cope (at the same vertical load) and the capacity of the specimen is thereby increased. This is reflected in the test results twice: for specimens 2A-3-0-R and 2B-3-0-R, and for specimens 2A-1-100C-R and 2B-1-100C-R. In both cases, the specimen with end-support B had a significantly higher peak vertical load, with the differences in material strengths indicating that the true influence is slightly greater yet. However, in both cases e_{eff}/e was also greater for the specimens with end-support B. This is likely due to the relative stiffnesses of the W530×92 girder and the W200×27 specimens for end-support A.

Table 4-8: Effect of end-support at peak vertical load

Specimen ID	Yield Strength (MPa)	Peak Vertical Load (kN)	Vertical Displacement (mm)	e_{eff}/e
2B-1-100T-R	359	186	16.8	0.79
2C-1-100T-R	359	208	21.0	0.50
2A-1-100C-R	376	133	7.4	0.69
2B-1-100C-R	359	162	8.2	0.71
2C-1-100C-R	359	114 / 166	1.3 / 10.0	0.73 / 0.98
2A-2-0-NR	376	110	29.4	0.36
2D-2-0-NR	362	105	6.8	0.99
2A-3-0-R	362	89	20.7	0.31
2B-3-0-R	359	138	5.8	0.72
3B-1-200C-R	396	363	8.6	0.07
3C-1-200C-R	396	254 / 372	2.0 / 10.1	-0.23 / 0.26
3A-2-0-NR	355	207	4.5	1.00
3D-2-0-NR	355	235	5.6	1.11

That is, for the six W200×27 specimens tested in shear only with end-support A, the ratio of e_{eff}/e at the peak vertical load was between 0.31 and 0.59, with an average of 0.41, meaning significant moment developed at the support, even though it is considered to be rotationally flexible. In comparison, the ratio of e_{eff}/e for specimen 2D-2-0-NR, which had similar coped region geometry to the six 2A specimens but a torsionally flexible girder support, was 0.99 at the peak vertical load, meaning the difference in behaviour was due to the end-support condition. For the eight other specimens that were tested with end-support A (six W310×33 and two W410×54), the ratio of e_{eff}/e at the peak vertical load was between 0.74 and 1.04 with an average of 0.94; i.e., the moment that developed at the support was low due to its flexibility. Specimen 3D-2-0-NR had a ratio of e_{eff}/e of 1.11 at the peak load, meaning the W310×39 girder was rotationally flexible, and behaved similarly to the W530×92 girder (end-support A). The relative stiffnesses of the coped region, the supporting girder, and the connection to the support govern the inflection point location, and therefore the effective eccentricity. The 2A specimens developed moment at the support because the stiffness of the girder to an applied

vertical load was large in comparison to that of the coped region of the beam. When the depths of the girder and coped region were similar, such as those for the 2D, 3A, 3D, and 4A specimens, low or no moment developed at the support, and the assumption that a rotationally flexible support results in an e_{eff}/e ratio close to 1.0 was affirmed.

When comparing rotationally flexible end-supports (A and D), the effect is somewhat unclear because the results capture differences in the specimen behaviour and capacity due to the presence of end-plates and due to the different girders that were used. For specimens 3A-2-0-NR and 3D-2-0-NR, for example, the more flexible end-support D resulted in higher effective eccentricity, higher vertical displacement at the peak vertical load, and higher peak vertical load (by 28 kN, or 13%). However, for specimens 2A-2-0-NR and 2D-2-0-NR, the effect of the W530×92 girder on the eccentricity, discussed above, resulted in 2A-2-0-NR having a 5 kN, or 4%, greater capacity. Nevertheless, the capacity differences in both comparisons are relatively small. When the support is rotationally flexible, the ductility provided by the end-plate is less critical.

In comparing the rotationally stiff supports (B and C), the support that develops higher moments will be associated with specimens with higher peak vertical loads because the moment at the face of the cope will be decreased. This is affirmed for specimens 2B-1-100T-R and 2C-1-100T-R, where specimen 2C-1-100T-R attained a peak vertical load 22 kN, or 12%, higher than specimen 2B-1-100T-R. Specimen 2C-1-100T-R developed high moment at the support, and therefore the effective eccentricity was lower than for 2B-1-100T-R. Two other comparisons between end-support B and C were made (2B-1-100C-R to 2C-1-100C-R and 3B-1-200C-R to 3C-1-200C-R); however, specimens 2C-1-100C-R and 3C-1-200C-R failed due to horizontal load following the rotation phase. The end-plate present in specimens 2B-1-100C-R and 3B-1-200C-R provided sufficient rotational ductility to the connection to withstand the specified rotation without excessively deforming the coped region out-of-plane, and therefore allowed these specimens to resist the specified horizontal load and significant vertical load. The secondary peak vertical

loads for specimens 2C-1-100C-R and 3C-1-200C-R were both 3% greater than those of specimens 2B-1-100C-R and 3B-1-200C-R, respectively, although the compressive load had diminished considerably.

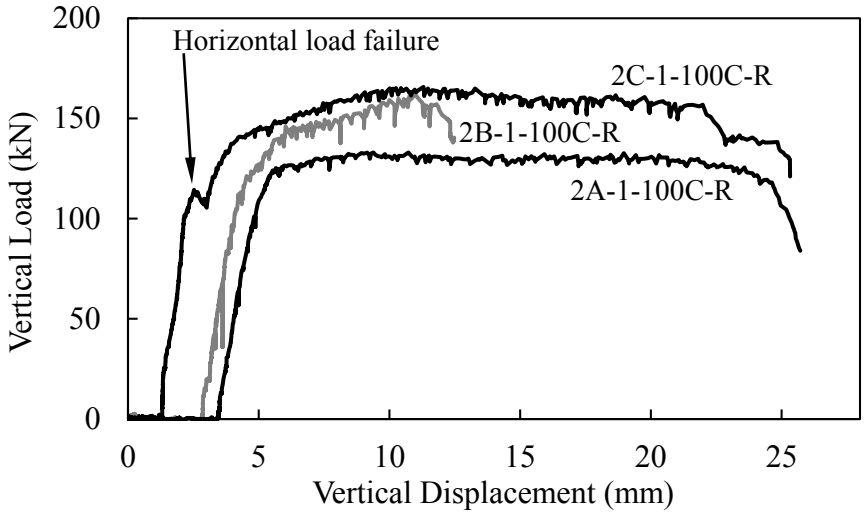

Figure 4-19: Effect of end-support on connection behaviour

The effect of end-support on the connection behaviour is shown in Figure 4-19 for three W200×27 specimens. In general, the behaviour of the three specimens shown is similar. Even after specimen 2C-1-100C-R failed to resist the specified horizontal load, it still had sufficient ductility and strength to reach a secondary peak higher than both specimens 2A-1-100C-R and 2B-1-100C-R.

4.6 Current Design Procedures

The currently-used design procedures for double-coped beams typically assume that the connection acts as a pinned support and therefore does not transfer moment to the supporting member. The test results have shown that in general this assumption is not correct, even if the beam is connected to a flexible support. In fact, it was not uncommon for test specimens to be subjected to greater moments at the support than at the net section, either at the peak vertical load or at a point of maximum moment.

The ratio of the effective eccentricity to the geometric eccentricity, which can be considered a ratio of the moments at the cope face and the support, was highly

variable due to the different end-supports tested. The W310×33 and W410×54 specimens connected to end-support A had e_{eff}/e near 1.0 at the peak vertical load because the rotational (torsional) stiffness of the girder was relatively low compared to the stiffness of the coped region. For specimens connected to end-supports B or C, the effective eccentricities, and therefore the tested capacities, depended largely on the coped region's ability to resist the first two phases of the testing sequence (rotation and horizontal load) without losing strength. Only two specimens (2C-1-100C-R and 4B-1-300C-R) remained at moments less than their yield moment during rotation, and others failed due to horizontal load early in the application of vertical load. Because the effective eccentricity at the peak load is affected by many factors, conservative assumptions may be required in practical design provisions for double-coped beams.

Four design procedures have been used to calculate the shear strengths of the double-coped beam specimens. In all cases, the material resistance factors have been omitted, and the measured specimen dimensions and material properties used. The strengths resulting from the procedures given by the Fabricator, the AISC *Manual* (AISC 2011), the AISC *Specification* (AISC 2010), and Dowswell and Whyte (2014) are compared to the peak vertical loads observed during testing in Table 4-9. Note that only the procedure given by the Fabricator accounts for axial load in assessing the stability of the coped region—the two AISC methods neglect axial load altogether, and although the procedure given by Dowswell and Whyte (2014) also neglects axial load, the authors suggest that the interaction equation by Neal (1961), given in Equation 2-34, be used to account for the combination of normal and shear stresses. Even though they do not explicitly state that axial load should be included if it is present, when calculating the reduced plastic moment capacity, the predicted capacities for Dowswell and Whyte's (2014) procedure in the following tables include axial load in the interaction equation, but only when the cross-sectional strength governs the design. Because the described methods assume the inflection point is at the face of the support, the geometric eccentricity is used when calculating all predicted capacities in Table 4-9. The

design procedures for each of the four methods are discussed in Chapter 2, and a sample calculation for each can be found in Appendix A.

In the sections below, specimens with horizontal load as the critical failure mode are omitted because it is likely that the testing sequence influenced the failure. In-plane restraint provided by the column flange was high, and the beam end rotation of 0.03 radians was applied without vertical or horizontal load present, resulting in an unrealistic second-order effect due to the large out-of-plane deformation present prior to the application of any load. In actual structures, the beam end rotation would develop as vertical load increased on the beam. For the 24 specimens that did not fail due to the prescribed compressive horizontal load, the peak vertical load attained is considered to be a reasonable, but conservative, estimate of the strength that would be observed under a more likely loading sequence.

The design of steel shear connections does not typically account explicitly for end-support type or the degree of beam end-rotation likely to occur at the ultimate limit state, even if detailing recommendations are available to help ensure a ductile response. Therefore, to group the specimens by their design parameters only, a three–variable generalized specimen ID was given to each group of specimens containing the same coped region geometry and the same applied axial load. For example, specimens 2A-1-100C-R and 2B-1-100C-R are both assigned to the group 2-1-100C. For all specimens shown in the tables below, the general ID and specimen ID are both shown. In each group, the specimen with the lowest tested capacity is considered the critical specimen that conservatively incorporates the effects of end rotation and end-support, and is shown in bold. In Table 4-9, the predicted capacities that are not governed by a cross-sectional strength limit are italicized.

Table 4-9: Comparison of design procedures (using the geometric eccentricity) and experimental capacities

General ID	Specimen ID	Test Capacity (kN)	Fabricator Capacity (kN)	AISC *Manual* Capacity† (kN)	AISC *Specification* Capacity† (kN)	Dowswell and Whyte Capacity†† (kN)
2-1-100T	**2B-1-100T-R**	**186**	75	73	110	92
	2C-1-100T-R	208	83	81	122	99
2-1-0	2A-1-0-R	173	105	70	105	97
	2A-1-0-NR	**149**	106	71	106	99
2-1-100C	**2A-1-100C-R**	**133**	*58*	70	105	90
	2B-1-100C-R	162	*57*	72	108	91
2-2-0	2A-2-0-R	111	*69*	47	71	69
	2A-2-0-NR	110	75	50	75	74
	2D-2-0-NR	**105**	71	50	75	73
2-3-0	**2A-3-0-R**	**89**	*53*	41	61	60
	2A-3-0-NR	99	*61*	42	63	63
	2B-3-0-R	138	*55*	42	63	62
3-1-100C	3A-1-100C-NR	260	*212*	216	324	239
3-1-200C	3B-1-200C-R	363	*233*	272	409	286
3-2-100T	3A-2-100T-NR	242	*187*	155	232	200
3-2-0	**3A-2-0-NR**	**207**	*174*	150	225	198
	3D-2-0-NR	235	*208*	168	252	218
3-2-100C	3A-2-100C-NR	191	*113*	152	228	197
3-3-0	3A-3-0-NR	199	*132*	128	192	178
3-3-100C	3A-3-100C-NR	182	*79*	129	194	175
4-2-200C	4B-2-200C-R	479	*219*	344	517	385
4-3-100T	4A-3-100T-NR	446	*204*	304	*324*	377
4-3-0	4A-3-0-NR	443	*225*	314	*357*	392
4-3-300C	4B-3-300C-R	360	*73*	291	*381*	335

† Neglects axial load
†† Only includes axial load in cross-sectional strength check
Italicized capacities indicate where no cross-sectional strength limit is reached

The Fabricator's method predicted that each specimen fails in one of four modes: flexural yielding, lateral–torsional buckling, bending and tension interaction, and bending and compression interaction, as discussed in Section 3.2.3 and summarized in Table 3-3. All 13 specimens subjected to axial compression were predicted to be

governed by the interaction of bending and compression. Of the four specimens subjected to axial tension, two (2B-1-100T-R and 2C-1-100T-R) were predicted to fail by the cross-sectional strength interaction of tension and bending, and two (3A-2-100T-NR and 4A-3-100T-NR) by lateral–torsional buckling. Three specimens tested without axial load (2A-1-0-R, 2A-1-0-NR, and 2A-2-0-NR) were predicted to reach the plastic moment at the face of the cope, and the remaining nine were predicted to fail by lateral–torsional buckling.

The failure mode predicted by the AISC *Manual* (AISC 2011) is flexural yielding at the yield moment for all specimens. Because both the d/t_w and c/d ratios for the test specimens are relatively low, the critical stress (Equation 2-16) is always limited by the yield stress of the beam, as discussed in Section 2.2.4.2. The result is that the strength of the specimen is predicted by Equation 2-4, where F_{cr} is equal to F_y.

The procedure in the AISC *Specification* (AISC 2010) predicted the test specimens would fail either by elastic lateral–torsional buckling or flexural yielding at the plastic moment, which is used as the strength limit for the nominal moment. The lateral–torsional buckling modification factor, C_b, given in section F1 of the AISC *Specification* (AISC 2010), was taken as 1.67 following the assumption that no moment is resisted by the support. Of the four test specimens that failed by buckling, three (4A-3-100T-NR, 4A-3-0-NR, and 4B-3-300C-R) were predicted to fail by elastic lateral–torsional buckling, and for 4B-2-200C-R the elastic lateral–torsional buckling moment capacity (Equations 2-23 and 2-24) was only 2% greater than M_p. The remainder of the specimens were governed by the plastic moment capacity. The ratio of the capacity predicted by the AISC *Specification* (AISC 2010) to that predicted by the AISC *Manual* (AISC 2011) for specimens that were predicted to be governed by the plastic and yield moments, respectively, is the shape factor for a rectangular cross-section: 1.5. Neither of these procedures includes provisions for axial load.

The design capacity obtained by the method of Dowswell and Whyte (2014) is also limited by the cross-sectional strength; however, they suggest that plastic moment

capacity be reduced with the interaction equation proposed by Neal (1961), given in Equation 2-34. The lateral–torsional buckling factor, C_b, derived by Dowswell and Whyte (2014) specifically for use with double-coped beams, increases the critical moment and causes the resulting capacities of all specimens to be governed by cross-sectional strength. If present, axial load was included in the interaction equation; however, axial load is not mentioned in the given procedure, and it is only assumed to be included because the method always resulted in the cross-sectional capacity governing the test specimens.

In Table 4-10, the peak vertical loads are shown as a ratio of the calculated strengths given in Table 4-9 to facilitate an assessment of the design procedures. Mean test-to-predicted ratios and the associated coefficients of variation (COV) are given for each design procedure for three different specimen sets. The first set includes all 24 of the specimens listed in Table 4-10, the second set includes only the 12 specimens tested without axial load, and the third set includes only the critical specimens: the six bolded specimens (lowest capacity from each group), and the ten specimens that had unique geometry.

The procedure given by the Fabricator under-predicted the capacity of all specimens, resulting in a mean test-to-predicted ratio and coefficient of variation of 1.94 and 40%, respectively. Although these values are the highest of the four procedures (considering all specimens), the Fabricator's method is the only one that attempts to assess the stability of the coped region accounting for axial compressive force by considering the coped region to act as a beam-column. Considering only specimens without axial load, the Fabricator's method gives a markedly reduced mean test-to-predicted ratio and coefficient of variation—1.60 and 21%, respectively—suggesting that the treatment of the coped region as a beam-column is overly conservative (especially so for specimen 4B-3-300C-R). The method correctly predicts specimens 2B-1-100T-R and 2C-1-100T-R to fail by the interaction of bending and tension (specimens failed by in-plane tearing at the upper re-entrant corner); however, their capacities were significantly under-predicted, contributing to the conservatism for specimens with axial load.

Table 4-10: Test-to-predicted strength ratios using the geometric eccentricity

General ID	Specimen ID		Fabricator Capacity	AISC *Manual* Capacity†	AISC *Specification* Capacity†	Dowswell and Whyte Capacity††
2-1-100T	**2B-1-100T-R**		2.47	2.53	1.69	2.01
	2C-1-100T-R		2.50	2.56	1.71	2.09
2-1-0	2A-1-0-R		1.65	2.48	1.65	1.78
	2A-1-0-NR		1.40	2.11	1.40	1.52
2-1-100C	**2A-1-100C-R**		2.31	1.90	1.26	1.47
	2B-1-100C-R		2.84	2.25	1.50	1.79
2-2-0	2A-2-0-R		1.60	2.35	1.56	1.60
	2A-2-0-NR		1.47	2.20	1.47	1.50
	2D-2-0-NR		1.48	2.11	1.40	1.44
2-3-0	**2A-3-0-R**		1.66	2.18	1.45	1.47
	2A-3-0-NR		1.62	2.34	1.56	1.58
	2B-3-0-R		2.48	3.28	2.19	2.21
3-1-100C	3A-1-100C-NR		1.23	1.20	0.80	1.09
3-1-200C	3B-1-200C-R		1.56	1.33	0.89	1.27
3-2-100T	3A-2-100T-NR		1.30	1.57	1.04	1.21
3-2-0	**3A-2-0-NR**		1.18	1.38	0.92	1.04
	3D-2-0-NR		1.13	1.40	0.93	1.08
3-2-100C	3A-2-100C-NR		1.69	1.26	0.84	0.97
3-3-0	3A-3-0-NR		1.51	1.55	1.03	1.12
3-3-100C	3A-3-100C-NR		2.30	1.41	0.94	1.04
4-2-200C	4B-2-200C-R		2.19	1.39	0.93	1.24
4-3-100T	4A-3-100T-NR		2.18	1.47	1.38	1.18
4-3-0	4A-3-0-NR		1.97	1.41	1.24	1.13
4-3-300C	4B-3-300C-R		4.92	1.24	0.95	1.07
All listed specimens		Mean:	1.94	1.87	1.28	1.41
		COV:	40%	29%	27%	25%
Specimens without axial load		Mean:	1.60	2.06	1.40	1.46
		COV:	21%	26%	24%	22%
Critical specimens from each group		Mean:	1.96	1.63	1.14	1.27
		COV:	44%	24%	23%	20%

† Neglects axial load

†† Only includes axial load in cross-sectional strength check

In the Fabricator's procedure, specimens without axial load were predicted to fail by either flexural yielding or lateral–torsional buckling; however, the method

incorrectly predicted which specimens would be governed by strength and which would be limited by stability. None of the three specimens (2A-1-0-R, 2A-1-0-NR, and 2A-2-0-NR) predicted to reach M_p at the face of the cope at the peak vertical load did so; however, specimen 2A-1-0-NR reached M_p at the face of the cope later in the test. The Fabricator's method was the least accurate and most variable when only the critical specimens are considered because many of the critical specimens have axial compression.

The AISC *Manual* (AISC 2011) also underestimated the specimen capacity for all the test specimens; however, it was slightly more accurate than the Fabricator's method (mean test-to-predicted ratio of 1.87) when all of the specimens are considered. The method, which uses the yield moment as the strength limit, gives notably conservative results for the W200×27 specimens, even when considering specimens without axial load. In fact, the mean test-to-predicted ratio increases to 2.06, the largest of the four procedures, if the set of shear only tests is considered. The mean test-to-predicted ratio for the critical specimens predicted by the AISC *Manual* (AISC 2011) is the lowest of the three data sets for this method (1.63) because the specimen set is largely made up of W310×33 and W410×54 specimens, which had reasonable test-to-predicted ratios.

The AISC *Specification* (AISC 2010) method over-predicted the capacities of eight specimens by up to 25%, resulting in the lowest mean test-to-predicted ratio—1.28—of the four procedures assessed, when considering all test specimens. The method, which does not account for the presence of axial load, over-predicted the capacities of only two such specimens by up to 9%. Moreover, it correctly predicted the elastic buckling failure for specimens 4A-3-100T-NR, 4A-3-0-NR, 4B-3-300C-R, and 4B-2-200C-R, suggesting that the procedure's ability to predict the critical failure mode is not greatly affected if the axial resistance ratio ($P/P_y = 0.10$, 0.21, and 0.32 for specimens 4A-3-100T-NR, 4B-2-200C-R, and 4B-3-300C-R, respectively) is relatively low. The remaining specimens were predicted to reach the plastic moment at the peak vertical load; however, it was observed that not all test specimens reached the plastic moment at the face of the

cope. The AISC *Specification* (AISC 2010) procedure had a slightly greater mean test-to-predicted ratio (1.40) when only specimens without axial load are considered, and when considering only the critical specimens the method provided a mean test-to-predicted ratio of 1.14 and a coefficient of variation of 23%. Of the specimen sets investigated, the AISC *Specification* (AISC 2010) procedure always produced the mean test-to-predicted ratio closest to 1.0.

Mean test-to-predicted ratios resulting from the method proposed by Dowswell and Whyte (2014) were always slightly greater than those obtained using the AISC *Specification* (AISC 2010) because the strength of the cross-section was reduced to account for the interaction of bending, shear and axial loads. The capacity of one specimen (3A-2-100C-NR) was over-predicted by approximately 4%. This method accounts for the interaction of stresses on the cross-section, but it did not identify the sudden buckling failures. Axial load is assumed to be taken into account, but only when calculating the strength of the cross-section. The stability of the coped region, subjected to moment and shear only, is accounted for with the lateral–torsional buckling modification factor, C_b; however, because all of the specimens in this testing program were predicted to be governed by their cross-sectional strength, it could not be assessed. The method proposed by Dowswell and Whyte (2014) consistently produced relatively low coefficients of variation due to the inclusion of axial load.

The main source of inaccuracy in all methods is that the moment at the support is unknown, and therefore the effective eccentricity cannot be determined and the geometric eccentricity is assumed when calculating the moment demand at the face of the cope. The methods generally give reasonable results for 3A, 3D, and 4A specimens (deeper with flexible support), and more conservative results when rotationally stiff end-supports increase the specimen capacity by reducing the moment at the face of the cope. Specimens within each of groups 2-1-100T, 2-2-0, and 3-2-0 generally had similar capacities; however, others, such as 2-1-100C and 2-3-0, had significantly different results due to different end-supports. To eliminate the inaccuracy in all methods specifically due the assumption of the inflection point location, the capacities predicted by the four design procedures were recalculated

using the effective eccentricity in the test at the peak vertical load in place of the geometric eccentricity, and are compared to the peak vertical loads observed during testing in Table 4-11.

Table 4-11: Comparison of design procedures (using the effective eccentricity) and experimental capacities

General ID	Specimen ID	Test Capacity (kN)	Fabricator Capacity (kN)	AISC *Manual* Capacity† (kN)	AISC *Specification* Capacity† (kN)	Dowswell and Whyte Capacity†† (kN)
2-1-100T	**2B-1-100T-R**	**186**	96	93	140	109
	2C-1-100T-R	208	139	161	189	139
2-1-0	2A-1-0-R	173	137	143	187	142
	2A-1-0-NR	**149**	138	121	181	134
2-1-100C	**2A-1-100C-R**	**133**	*90*	102	154	118
	2B-1-100C-R	162	*85*	101	151	114
2-2-0	2A-2-0-R	111	133	123	181	132
	2A-2-0-NR	110	146	140	199	147
	2D-2-0-NR	**105**	72	51	76	74
2-3-0	**2A-3-0-R**	**89**	134	131	183	136
	2A-3-0-NR	99	142	118	177	135
	2B-3-0-R	138	*77*	58	87	84
3-1-100C	3A-1-100C-NR	260	*201*	208	312	235
3-1-200C	3B-1-200C-R	363	313	427	427	401
3-2-100T	3A-2-100T-NR	242	*254*	210	315	237
3-2-0	**3A-2-0-NR**	**207**	*175*	150	225	198
	3D-2-0-NR	235	*187*	152	227	204
3-2-100C	3A-2-100C-NR	191	*121*	158	237	202
3-3-0	3A-3-0-NR	199	*131*	128	191	177
3-3-100C	3A-3-100C-NR	182	*95*	144	215	189
4-2-200C	4B-2-200C-R	479	420	575	575	485
4-3-100T	4A-3-100T-NR	446	*242*	361	*439*	411
4-3-0	4A-3-0-NR	443	*218*	304	*353*	385
4-3-300C	4B-3-300C-R	360	419	571	571	514

† Neglects axial load

†† Only includes axial load in cross-sectional strength check

Italicized capacities indicate where no cross-sectional strength limit is reached

Because the effective eccentricities were generally less than the geometric eccentricities, the resulting capacities using the true inflection point location were generally greater than those using the assumed location at the face of the support. Additionally, the greater shear capacities may have resulted in a change in the failure mode predicted by the different methods, as described below.

The Fabricator's method still predicted that each specimen fails in one of four modes; however, unlike when the geometric eccentricity is used, elastic shear strength (Equation 2-37) was predicted to govern for all specimens with the exception of eight (2B-3-0-R, 2D-2-0-NR, 3A-2-100T-NR, 3A-2-0-NR, 3A-3-0-NR, 3D-2-0-NR, 4A-3-100T-NR, and 4A-3-0-NR) that were predicted to fail by lateral–torsional buckling, five (2A-1-100C-NR, 2B-1-100C-R, 3A-1-100C-NR, 3A-2-100C-NR, and 3A-3-100C-NR) that were predicted to fail by compression and bending interaction, and one (2B-1-100T-R) that was predicted to fail by tension and bending interaction.

When the geometric eccentricity was used, the shear capacities predicted by the two AISC methods were governed by the respective flexural strength limit: the yield moment or the plastic moment; however, low effective eccentricities resulted in shear capacities limited to the plastic shear strength, V_p, (Equation 2-38), where the 0.577 shear coefficient is increased to 0.6, in accordance with the AISC *Specification* (AISC 2010). The AISC *Manual* (AISC 2011) predicted that all specimens would fail by flexural yielding at the yield moment, except three (3B-1-200C-R, 4B-2-200C-R, and 4B-3-300C-R) that would reach the plastic shear strength. The procedure given in the AISC *Specification* (AISC 2010) predicted the majority of test specimens would fail by flexural yielding at the plastic moment, except for two specimens (4A-3-100T-NR and 4A-3-0-NR) that would fail by elastic lateral–torsional buckling, and eight (2A-1-0-R, 2A-2-0-R, 2A-2-0-NR, 2A-3-0-R, 2C-1-100T-R, 3B-1-200C-R, 4B-2-200C-R, and 4B-3-300C-R) that would reach the plastic shear strength. The lateral–torsional buckling factor, C_b, previously taken as 1.67 when the inflection point was assumed to be at the face of the support, was appropriately calculated for each specimen from the moments

acting on the coped region at the peak vertical load according to section F1 of the AISC *Specification* (AISC 2010).

The reduced plastic moment determined from the design procedure given by Dowswell and Whyte (2014) that includes the interaction of normal and shear stresses governs the cross-sectional strength limit for all specimens, and the lateral–torsional buckling factor, C_b, (Equation 2-25) was the same as for the specimens predicted by this method in Table 4-9.

In Table 4-12, the peak vertical loads are shown as a ratio of the calculated strengths using the effective eccentricities, as given in Table 4-11, to facilitate an assessment of the design procedures with the known inaccuracy of the assumed inflection point location removed. The resulting mean test-to-predicted ratios for all methods and all specimen sets are between 15% and 35% less when the effective eccentricities are used in place of the geometric eccentricities. Conversely, the coefficients of variation increased for all of the design methods and specimen sets except for the Fabricator's method for the sets of all specimens and critical specimens only, which both had lower coefficients of variation. This suggests that although the mean test-to-predicted ratios are considerably closer to 1.0, the behaviour of double-coped beams is not completely captured by any of the methods—the design procedures still over- and under-predict the capacities with large variation.

The design procedures given by the Fabricator and the AISC *Manual* (AISC 2011) are the most conservative, i.e., the mean test-to-predicted ratios for these methods for the sets considered were consistently greater than 1.0. The AISC *Specification* (AISC 2010) procedure over-predicted the capacity of more than half of the specimens, and some by over 100%, resulting in the lowest mean test-to-predicted ratios of the procedures assessed. Mean test-to-predicted ratios for the procedure proposed by Dowswell and Whyte (2014) were greater than those given by the AISC *Specification* (AISC 2010) due to the cross-sectional strength limit by Neal (1961), which governed all specimens, that includes the interaction of normal and shear stresses. Neal's (1961) interaction equation provided the best results of the assessed design procedures: when the set of critical specimens were considered,

it resulted in a mean test-to-predicted ratio of 1.07 with a coefficient of variation of 22%.

Table 4-12: Test-to-predicted strength ratios using the effective eccentricity

General ID	Specimen ID		Fabricator Capacity	AISC *Manual* Capacity†	AISC *Specification* Capacity†	Dowswell and Whyte Capacity††
2-1-100T	**2B-1-100T-R**		1.94	1.99	1.33	1.70
	2C-1-100T-R		1.50	1.29	1.10	1.49
2-1-0	2A-1-0-R		1.26	1.21	0.92	1.21
	2A-1-0-NR		1.08	1.24	0.83	1.11
2-1-100C	**2A-1-100C-R**		1.49	1.30	0.87	1.13
	2B-1-100C-R		1.90	1.61	1.07	1.43
2-2-0	2A-2-0-R		0.83	0.90	0.61	0.84
	2A-2-0-NR		0.75	0.79	0.55	0.75
	2D-2-0-NR		1.46	2.08	1.38	1.43
2-3-0	**2A-3-0-R**		0.66	0.68	0.49	0.65
	2A-3-0-NR		0.69	0.83	0.56	0.73
	2B-3-0-R		1.79	2.37	1.58	1.64
3-1-100C	3A-1-100C-NR		1.29	1.25	0.83	1.11
3-1-200C	3B-1-200C-R		1.16	0.85	0.85	0.90
3-2-100T	3A-2-100T-NR		0.95	1.15	0.77	1.02
3-2-0	**3A-2-0-NR**		1.18	1.38	0.92	1.04
	3D-2-0-NR		1.25	1.55	1.03	1.15
3-2-100C	3A-2-100C-NR		1.59	1.21	0.81	0.95
3-3-0	3A-3-0-NR		1.52	1.56	1.04	1.12
3-3-100C	3A-3-100C-NR		1.92	1.27	0.84	0.96
4-2-200C	4B-2-200C-R		1.14	0.83	0.83	0.99
4-3-100T	4A-3-100T-NR		1.84	1.24	1.02	1.09
4-3-0	4A-3-0-NR		2.03	1.46	1.26	1.15
4-3-300C	4B-3-300C-R		0.86	0.63	0.63	0.70
All listed specimens		Mean:	1.34	1.28	0.92	1.10
		COV:	31%	34%	29%	25%
Specimens without axial load		Mean:	1.21	1.34	0.93	1.07
		COV:	35%	37%	36%	26%
Critical specimens from each group		Mean:	1.38	1.26	0.92	1.07
		COV:	29%	31%	25%	22%

† Neglects axial load

†† Only includes axial load in cross-sectional strength check

4.7 Discussion

The accuracy of the design method proposed by Dowswell and Whyte (2014) could not be fully assessed because the cross-sectional strength governed the design of the double-coped beams for the geometries used in this testing program ($0.3 \leq c/h_0 \leq 1.2$). This suggests that proportioning copes close to their minimum geometries, i.e., smallest cope length and depth required when connecting to an equal depth girder (refer to Section 3.2.1), eliminated most stability issues. Test specimens with slender coped regions subjected to axial compression were thought to be prone to stability-based failures; however, the cross-sectional strength interaction equation by Neal (1961) was a conservative, but appropriate, method to estimate the strength of the connection even when the geometric eccentricity was used. Of the four design procedures investigated, the method proposed by Dowswell and Whyte (2014) is the most rational when the cross-sectional capacity governs the strength because the interaction between bending and shear stresses on the cross-section is accounted for. Although the AISC *Specification* (AISC 2010) method provided mean test-to-predicted ratios closer to 1.0 when using the geometric eccentricity, it neglects normal stresses from axial load, and the interaction of normal and shear stresses when determining the cross-sectional strength.

The location of the inflection point is critical to determining the strength of a double-coped beam accurately. Methods to evaluate the strength of a beam with a rectangular cross-section fall short if the applied moment at the face of the cope cannot be accurately estimated. Design guidelines have avoided this by assuming that the inflection point is at the face of the supporting member, and the coped region is designed using the full geometric eccentricity, which was shown to be conservative. The AISC *Manual* (AISC 2011) states that "… a lesser value [than the geometric eccentricity] of e may be justified, and the use of e [the geometric eccentricity]…is conservative." However, this is only true when only the coped region is considered—the assumption is unconservative for the design of the connection to the support and the support itself because moment, which can develop

in significant magnitudes even if the support is considered to be rotationally flexible, is neglected. This lack of conservatism increases for rotationally stiff supports that can in some cases impose greater moments than exist at the face of the cope.

The strength and behaviour of double-coped beam connections are also related to their ability to accommodate local deformations and provide rotational ductility to the beam end. The coped region must resist the applied load and have dimensions that ensure a ductile failure. Yielding in the coped region is the desired failure mode and, where possible, elastic buckling should be avoided. Engineering judgement should be used to assess the ability of the connection to provide rotational ductility to the beam end. Although it may be unfeasible to quantify the rotational restraint provided by the end-support accurately, some effort must be given by the connection designer to provide flexibility, such as the use of an end-plate. Alternatively, if the rotational stiffness of the support cannot be reduced, a different connection type that can provide rotational flexibility without compromising the connection strength may be more appropriate. For the connections included in this testing program, rotational ductility was provided by flexible end-supports, or by the coped region; however, in the latter case, the vertical load carrying capacity was affected when significant yielding and out-of-plane deformation were required to achieve that ductility. However, the loading sequence used to test the connections was likely more severe than that in an actual structure. The end rotation of 0.03 radians, considered a reasonable upper limit to the beam end rotation provided by the connection and the support, was added when no vertical load was present. In actual structures, it is more likely that the beam end rotation will approach its upper limit under shear load that is approaching the shear yield capacity of the connection. Additionally, requiring this end rotation with a stiff end-support that is also considered an upper limit to the in-plane rotational restraint was severe, and may have affected the capacity of many test specimens, e.g. the specimens that reached M_p during the rotation phase and the specimens that failed due to horizontal load.

4.8 Summary

The double-coped beams tested failed due to out-of-plane deformation, buckling, in-plane tearing, or horizontal load failure. Deformed shapes showed characteristics of multiple modes of failure, but a quantitative method to predict the failure mode reliably from the initial geometry of the specimen was not found. Moments at the beginning and end of the coped region were used to determine the location of the inflection point and its movement throughout the loading history. The moment distribution was greatly affected by the rotational restraint of the end-support used, and from the presence of beam end rotation. Load, moment and eccentricity versus displacement curves for all specimens are located in Appendix C. The results of the tests are discussed, including the effect of each variable on the specimen behaviour and peak vertical load capacity. Current design procedures, which neglect axial load, generally under-predict the connection capacity, even if axial load exists on the connection. For the double-coped beams tested in this research program, stability of the coped region did not impact the test specimen's ability to reach a strength limit. The interaction equation proposed by Neal (1961), provided a rational, reasonable, and conservative estimate of the specimen capacity when using the full geometric eccentricity.

CHAPTER 5: SUMMARY AND CONCLUSIONS

5.1 Summary

Coped beams are used commonly in shear connections to either a girder or column to avoid interferences between the beam flanges and the supporting member. Beams coped at both top and bottom flanges are typically used in beam-to-girder connections when the beam and girder have similar depths. Although they are relatively common, very few research programs have been completed on the local strength and behaviour of double-coped beams, and no published information exists on full-scale tests. Elastic finite element modelling by Cheng et al. (1984) provided the design equation currently in the AISC *Manual* (AISC 2010); however, the equation estimates the critical stress at the face of the cope using a curve-fit adjustment factor, and gives overly conservative results because it is limited by a first-yield criterion. Dowswell and Whyte (2014) proposed changes to the design guidelines in the AISC *Specification* (AISC 2010) for the design of rectangular bars bent about their major axis based on further elastic finite element modelling. A new lateral–torsional buckling modification factor, C_b, was derived to assess the stability of the coped region, and if the coped region is stocky, the cross-sectional strength is assessed using an interaction equation proposed by Neal (1961) that accounts for the presence of axial load. None of the current design guidelines addresses the presence of axial load when assessing the stability of the coped region.

To investigate the local strength and behaviour of double-coped beams and create a database of physical test results, 29 full-scale double-coped beams were tested. The test beam was braced laterally so that only local failures occurred (in the coped region), and was loaded with both horizontal and vertical loads to study the combined effect. Double-coped beam specimens varied by section depth and cope length, resulting in cope-length-to-reduced-beam-depth ratios (c/h_0) between 0.29 and 1.19, and were tested with different horizontal loads, end rotations, and end-supports. The testing sequence was: rotation, horizontal load, then vertical load until failure of the specimen, while maintaining the specified rotation and horizontal load.

The critical failure mode was identified for each test specimen. The majority of specimens failed by out-of-plane deformation, a ductile failure mode associated with yielding of the cross-section, gradual out-of-plane movement of the coped region, and significant post-peak strength. Four specimens failed by sudden buckling of the coped region, two failed by in-plane tearing at the upper re-entrant corner, and five failed due to their inability to maintain the specified horizontal load. Inelastic behaviour was present in all of the 29 tests, despite the design procedures predicting various failure modes including elastic and inelastic lateral–torsional buckling or flexural yielding.

Four design procedures were assessed to determine their ability to predict the failure mode and capacity of the test specimen. The test results were grouped in different sets to determine the accuracy of the design procedures. Generally, all four methods produced conservative results due to the assumption that no moment develops at the support, which was shown to be untrue, even when a flexible end-support is used. The design procedures were also assessed using the effective eccentricity observed during the test, and shown to be much more accurate at predicting the peak vertical load, although there was still significant scatter in the results. The design procedure in the AISC *Specification* (AISC 2010) provided the most accurate prediction of the shear capacity using the geometric eccentricity for all specimen sets investigated, despite the method neglecting axial load. The proposed method by Dowswell and Whyte (2014) was the most rational when the cross-sectional strength governs because it accounts for the interaction of stresses, and was therefore also more conservative.

5.2 Conclusions

The following conclusions from the current research can be made:

1. The capacity of a double-coped beam is significantly greater for heavier sections than lighter ones due to increased cross-sectional depth and thickness.
2. A longer cope length results in reduced capacity due to a greater moment at the face of the cope (for the same vertical load); however, higher vertical

displacements will exist at the peak vertical load compared to connections with a shorter cope length.

3. Tensile load up to 32% of the axial yield load, P_y, stabilizes the coped region and increases the connection capacity, and compressive load up to the same limit destabilizes the coped region and decreases the connection capacity. Axial loads less than 10% of P_y generally have little effect on the connection capacity.
4. Applied end rotation generally increases the capacity of double-coped beams with flexible end-supports; however, applying end rotation on connections with rotationally stiff supports results in local yielding and out-of-plane deformation.
5. The capacity of a double-coped beam is generally greater when it is connected to an end-support with higher rotational stiffness due to the more favourable resulting distribution of moments in the coped region. End-supports with high rotational stiffness compared to the coped region develop moment that decreases the moment at the face of the cope (at the same vertical load), and thereby increases the capacity. End-supports with low rotational stiffness compared to the coped region generally do not develop moments significant enough to affect the moment at the face of the cope.
6. Moments redistributing in the coped region during vertical loading results in movement of the inflection point. Generally, when the capacity of the double-coped beam is reached, the coped region is in double curvature and the inflection point could be present almost anywhere between the face of the cope and the support, depending on the support's rotational stiffness.
7. Assuming zero moment at the support (for all end-support types) is conservative for the design of the coped region, but is unconservative when designing the support, or the connection to the support, that may be subjected to significant moment not considered by the designer.
8. Rotational ductility of the beam end, provided by a flexible end-support or end-plate, or the coped region if needed, is very important to the strength

and behaviour of the coped region. When the ductility is exhausted, the strength of the connection is reduced.

5.3 Recommendations for Further Research

Although the test results from the current research have contributed significantly to the understanding of double-coped beams by examining their behaviour under the combined effects of bending, shear and axial loads, areas where further research is required are identified as follows:

1. To limit the number of tests, not all potential variables were studied. A parametric study is recommended to further investigate the behaviour of double-coped beams under combined loads. Additional geometric parameters may include the independent effects of the reduced beam depth in the coped region, the cope depth, and the web thickness. In the current study, the reduced beam depth and web thickness were coupled (the cope depth was constant), as dictated by the beam section.
2. Additional research may also be able to determine the range of double-coped beam behaviour that depends on the cope-length-to-reduced-beam-depth ratio, c/h_0. Specimens in this testing program, with $c/h_0 \leq 1.2$, generally behaved inelastically and their capacities could be predicted with reasonable accuracy by their cross-sectional strength; however, double-coped beam models investigated by Cheng et al. (1984) and Dowswell and Whyte (2014) had significantly greater values of c/h_0—up to 2.52 and 4.99, respectively—that underwent elastic buckling. This suggests that some ratio of c/h_0 may separate double-coped beams susceptible to stability failure from those that are not.
3. Further study is needed on the application of axial load to fully assess the stability of the coped region under combined loads. In this research, the applied axial load did not exceed 32% of the axial yield load, P_y; however, larger axial loads likely have a more significant effect on the cope region's stability.

4. Further investigation on the behaviour of double-coped beams connected to a more likely range of support stiffnesses is required. Rotational ductility at the beam end is important to the connection behaviour; however, the end-supports in this testing program were selected to act as upper and lower bounds for the rotational stiffnesses of typical end-supports. Additionally, it may be useful to determine if the connection ductility can be improved, even if the support stiffness is high, e.g., changing the end-plate dimensions or bolt group pattern so the coped region can deform without affecting the connection strength.

REFERENCES

Aalberg, A., and Larsen, P. K. (2001). "Local web buckling of coped beams." *Proceedings of Nordic Steel Construction Conference NSCC 2001,* Helsinki, Finland, 721-728.

Aalberg, A., and Larsen, P. K. (2000). "Strength and ductility of bolted connections in normal and high strength steels." *Proceedings of the Seventh International Symposium on Structural Failure and Plasticity,* Melbourne, Australia, 487-494.

Ahmed, S. R., Idris, A. B. M., and Uddin, M.,W. (1996). "Numerical solution of both ends fixed deep Beams." *Comp. & Struct.,* 61(1), 21-29.

AISC. (2011). *Steel Construction Manual, 14th Edition.* American Institute of Steel Construction, Chicago, IL.

AISC. (2010). "Specification for Structural Steel Buildings." ANSI/AISC 360-10 1-612.

AISC. (2005). *Steel Construction Manual, 13th Edition.* American Institute of Steel Construction, Chicago, IL.

Astaneh, A. (1998). "Seismic behavior and design of gusset plates." *Steel Tips,* December.

Astaneh, A. (1989). "Demand and supply of ductility in steel shear connections." *J. Constr. Steel. Res.,* 14(1), 1-19.

ASTM. (2014). *A370-14: Standard Test Methods and Definitions for Mechanical Testing of Steel Products.* ASTM International, West Conshohocken, PA.

Barry, J. E., and Ainso, H. (1983). "Single-span deep beams." *J. Struct. Eng.,* 109(3), 646-663.

Cheng, J. J. R., and Yura, J. A. (1986). "Local web buckling of coped beams." *J. Struct. Eng.,* 112(10), 2314-2331.

Cheng, J. J. R., Yura, J. A., and Johnson, C. P. (1988b). "Lateral buckling tests on coped steel beams." *Journal of Constructional Steel Research,* 114(1), 16-30.

Cheng, J. J. R., Yura, J. A., and Johnson, C. P. (1988a). "Lateral buckling of coped steel beams." *J. Struct. Eng.,* 114(1), 1-15.

Cheng, J. J. R., Yura, J. A., and Johnson, C. P. (1984). "Design and behavior of coped beam." University of Texas, Austin, TX.

CISC. (2012). *Handbook of Steel Construction, 10th Edition, Fourth Revised Printing 2012.* Canadian Institute of Steel Construction, Markham, ON.

CSA. (2014). *S16-14 Design of Steel Structures.* Canadian Standards Association, Mississagua, ON.

CSA. (2013). *CSA G40.21-13: General Requirements for Rolled of Welded Structural Quality Steel.* Canadian Standards Association, Mississagua, ON.

Dowswell, B. (2004). "Lateral-torsional buckling of wide flange cantilever beams." *Eng. J.,* 41(2), 135-147.

Dowswell, B., and Whyte, R. (2014). "Local stability of double-coped beams." *Eng. J.,* 43-52.

du Plessis, D. P. (1977). "Lateral-torsional buckling of end notched steel beams." *International Colloquium on Stability of Structures Under Static and Dynamic Loads,* Structural Stability Research Council, Washington, D.C., 563-572.

Fang, C., Lam, A. C. C., Yam, M. C. H., and Seak, K. S. (2013). "Block shear strength of coped beams with single-sided bolted connection." *J. Constr. Steel. Res.,* 86(1), 153-166.

Franchuk, C. R., Driver, R. G., and Grondin, G. Y. (2004). "Reliability analysis of block shear capacity of coped steel beams." *J. Struct. Eng.,* 130(12), 1904-1913.

Franchuk, C. R., Driver, R. G., and Grondin, G. Y. (2003). "Experimental investigation of block shear failure in coped steel beams." *Can. J. Civ. Eng.,* 30(5), 871-881.

Gerard, G., and Becker, H. (1957). *Handbook of Structural Stability Part 1 - Buckling of Flat Plates.* NACA, TN 3781.

Gupta, A. K. (1984). "Buckling of coped steel beams." *J. Struct. Eng.,* 110(9), 1977-1987.

Holden, T. A. (2012). "Fatigue rehabilitation of coped steel beams using carbon fibre reinforced polymers". Department of Civil and Environmental Engineering, University of Alberta, Edmonton, AB.

Lam, A. C. C., Yam, M. C. H., Iu, V. P., and Cheng, J. J. R. (2000). "Design for lateral-torsional buckling of coped I-beams." *J. Constr. Steel. Res.,* 54(1), 423-443.

Maljaars, J., Stark, J. W. B., Steenbergen, H. M. G. M., and Abspoel, R. (2005b). "Development and validation of a numerical model for buckling of coped beams." *J. Constr. Steel. Res.,* 61(11), 1576-1593.

Maljaars, J., Stark, J. W. B., Steenbergen, H. M. G. M., and Abspoel, R. (2005a). "Lateral-torsional buckling resistance of coped beams." *J. Constr. Steel. Res.,* 61(11), 1559-1575.

Muir, L. S., and Thornton, W. A. (2004). "A technical note: a direct method for obtaining the plate buckling coefficient for double-coped beams." *Eng. J.,* 41(3), 133-134.

Neal, B. G. (1977). *The Plastic Methods of Structural Analysis.* John Wiley and Sons, New York, NY.

Neal, B. G. (1961). "The effect of shear and normal forces on the fully plastic moment of a beam of rectangular cross section." *J. App. Mech.,* 28 269-274.

Shawki, S., and Hendry, A. W. (1961). "Stresses in a deep beam with a central concentrated load." *Exp. Mech.,* 192-198.

Topkaya, C. (2007). "Finite element modeling of block shear failure in coped steel beams." *J. Constr. Steel. Res.,* 63(4), 544-553.

Wei, F., Yam, M. C. H., Chung, K. F., and Grondin, G. Y. (2010). "Tests on block shear of coped beams with a welded end connection." *J. Constr. Steel. Res.,* 66(11), 1398-1410.

Yam, M. C. H., and Cheng, J. J. R. (1990). "Fatigue strength of coped steel beams." *J. Struct. Eng.,* 116(9), 2447-2463.

Yam, M. C. H., and Chung, K. F. (2013). "A numerical study of the strength and behaviour of reinforced coped beams." *J. Constr. Steel. Res.,* 80(1), 224-234.

Yam, M. C. H., Fang, C., Lam, A. C. C., and Cheng, J. J. R. (2014). "Local failures of coped steel beams - a state-of-the-art review." *J. Constr. Steel. Res.,* 102(1), 217-232.

Yam, M. C. H., Grondin, G. Y., Wei, F., and Chung, K. F. (2011). "Design for block shear of coped beams with a welded end connection." *J. Struct. Eng.,* 137(8), 811-821.

Yam, M. C. H., Lam, A. C. C., Iu, V. P., and Cheng, J. J. R. (2003). "Local web buckling strength of coped steel I-beams." *J. Struct. Eng.,* 129(1), 3-11.

Yam, M. C. H., Lam, A. C. C., Wei, F., and Chung, K. F. (2007a). "The local web buckling strength of stiffened coped steel I-beams." *Int. J. Steel Struct.,* 7(2), 129-138.

Yam, M. C. H., Ma, H. W., Lam, A. C. C., and Chung, K. F. (2011). "Experimental study of the strength and behaviour of reinforced coped beams." *J. Constr. Steel. Res.,* 67(1), 1749-1759.

Yam, M. C. H., Zhong, Y. C., Lam, A. C. C., and Iu, V. P. (2007b). "An investigation of the block shear strength of coped beams with a welded clip angle connection-part I: experimental study." *J. Constr. Steel. Res.,* 63(1), 96-115.

Yam, M. C. H., Zhong, Y. C., Lam, A. C. C., and Iu, V. P. (2007c). "An investigation of the block shear strength of coped beams with a welded clip angle connection-part II: numerical study." *J. Constr. Steel. Res.,* 63(1), 116-134.

APPENDIX A: SAMPLE CALCULATIONS

Table A-1: Test specimen as-built properties (from Table 3-3)

Specimen ID	d (mm)	c (mm)	d_{ct} (mm)	d_{cb} (mm)	h_0 (mm)	t_w (mm)	F_y (MPa)	E (MPa)
2A-3-0-NR	204	175.6	30.0	29.4	144.6	6.0	376	196 070
3A-2-100C-NR	313	150.5	31.3	30.5	251.2	6.5	355	196 324

Sample calculations for specimen 2A-3-0-NR:

Initial calculations:

1. Geometric eccentricity

$e = c + t_e = 175.6 \text{ mm} + 9.5 \text{ mm} = 185.1 \text{ mm}$

2. Cross-sectional properties

$$I_y = \frac{h_0 t_w^3}{12} = \frac{(144.6 \text{ mm})(6.0 \text{ mm})^3}{12} = 2603 \text{ mm}^4$$

$J = 4I_y = 4(2603 \text{ mm}^4) = 10\,412 \text{ mm}^4$

$$G = \frac{E}{2.6} = \frac{196\,070 \text{ MPa}}{2.6} = 75\,412 \text{ MPa}$$

3. Cross-sectional strength

$$M_y = \frac{h_0^2 t_w F_y}{6} = \frac{(144.6 \text{ mm})^2(6.0 \text{ mm})(376 \text{ MPa})}{6} = 7.8 \text{ kN·m}$$

$$M_p = \frac{h_0^2 t_w F_y}{4} = \frac{(144.6 \text{ mm})^2(6.0 \text{ mm})(376 \text{ MPa})}{4} = 11.7 \text{ kN·m}$$

$V_p = 0.6 h_0 t_w F_y = 0.6(144.6 \text{ mm})(6.0 \text{ mm})(376 \text{ MPa}) = 196 \text{ kN}$

Fabricator's Design Procedure (2A-3-0-NR):

1. Shear strength assuming elastic stress distribution

$$V_1 = \frac{0.66 h_0 t_w F_y}{1.5} = \frac{0.66(144.6 \text{ mm})(6.0 \text{ mm})(376 \text{ MPa})}{1.5} = 144 \text{ kN}$$

2. Lateral–torsional buckling of coped region

$$t_{w,min} = 0.877 \sqrt{\frac{c h_0}{\omega_2} \frac{F_y}{E}}$$

$$t_{w,min} = 0.877\sqrt{\frac{(175.6\text{ mm})(144.6\text{ mm})}{1.0}\ \frac{376\text{ MPa}}{196\,070\text{ MPa}}} = 6.1\text{ mm}$$

$t_w = 6.0$ mm $< t_{w,min} = 6.1$ mm, ∴ LTB prevents attainment of M_p

$$M_u = \frac{\omega_2\pi}{c}\sqrt{EI_yGJ}$$

$$M_u = \frac{(1.0)\pi}{175.6\text{ mm}}\sqrt{(196\,070\text{ MPa})(2603\text{ mm}^4)(75\,412\text{ MPa})(10\,411\text{ mm}^4)}$$

$M_u = 11.3$ kN·m

$$V_2 = \frac{M_u}{e} = \frac{11.3\text{ kN·m}}{185.1\text{ mm}} = 61\text{ kN}$$

3. Local web buckling (AISC 2011)

$$\frac{c}{d} = \frac{175.6\text{ mm}}{204\text{ mm}} = 0.86 < 2 \rightarrow \text{OK}$$

$$\frac{d_c}{d} = \frac{30\text{ mm}}{204\text{ mm}} = 0.15 < 0.2 \rightarrow \text{OK}$$

Geometry satisfied, therefore appropriate to use method

$$f_d = 3.5 - 7.5\left(\frac{d_{ct}}{d}\right) = 3.5 - 7.5\left(\frac{30\text{ mm}}{204\text{ mm}}\right) = 2.4$$

$$F_{cr} = 0.62\pi E\frac{{t_w}^2}{ch_0}f_d$$

$$F_{cr} = 0.62\pi(196\,070\text{ MPa})\frac{(6.0\text{ mm})^2}{(175.6\text{ mm})(144.6\text{ mm})}(2.4) = 1299\text{ MPa}$$

$F_{cr} = 1299$ MPa $\not< F_y = 376$ MPa, ∴ local buckling does not govern

$$V_{Fabricator} = \text{minimum of: } \left\{\begin{matrix} V_1 = 144\text{ kN} \\ V_2 = 61\text{ kN} \end{matrix}\right\} = 61\text{ kN}$$

<u>AISC *Manual* (AISC 2011) Design Procedure (2A-3-0-NR):</u>

1. Local web buckling (critical stress determined in Fabricator's method)

$F_{cr} = 1299$ MPa $\not< F_y = 376$ MPa, ∴ $F_{cr} = 376$ MPa

$M_n = S_{net}F_{cr} = S_{net}F_y = M_y = 7.8$ kN·m

$$V_{Manual} = \frac{M_n}{e} = \frac{7.8\text{ kN·m}}{185.1\text{ mm}} = 42\text{ kN}$$

AISC *Specification* (AISC 2010) Section F11 Design Procedure (2A-3-0-NR):

1. Nondimensional slenderness parameter

$$\frac{L_b d}{t^2} = \frac{c h_0}{t_w^2} = \frac{(175.6\text{ mm})(144.6\text{ mm})}{(6.0\text{ mm})^2} = 705$$

$$\frac{0.08E}{F_y} = \frac{0.08(196\,070\text{ MPa})}{(376\text{ MPa})} = 42$$

$$\frac{1.9E}{F_y} = \frac{1.9(196\,070\text{ MPa})}{(376\text{ MPa})} = 991$$

$$\frac{0.08E}{F_y} = 42 < \frac{L_b d}{t^2} = 705 < \frac{1.9E}{F_y} = 991 \therefore \text{inelastic lateral–torsional buckling}$$

2. Nominal flexural strength

$$M_n = C_b \left[1.52 - 0.274\left(\frac{L_b d}{t^2}\right)\frac{F_y}{E}\right] M_y \quad \Longrightarrow \quad M_n = C_b \left[1.52 - 0.274\left(\frac{c h_0}{t_w^2}\right)\frac{F_y}{E}\right] M_y$$

$$M_n = (1.67)\left[1.52 - 0.274(705)\frac{376\text{ MPa}}{196\,070\text{ MPa}}\right](7.8\text{ kN·m}) = 15.2\text{ kN·m}$$

$$M_n = 15.2\text{ kN·m} > M_p = 11.7\text{ kN·m} \therefore M_n = 11.7\text{ kN·m}$$

$$V_{Specification} = \frac{M_n}{e} = \frac{11.7\text{ kN·m}}{185.1\text{ mm}} = 63\text{ kN}$$

Dowswell and Whyte (2014) Design Procedure (2A-3-0-NR):

1. Slenderness parameter and slenderness limits (similar to AISC *Specification*)

$$\lambda = \frac{L_b h_0}{t_w^2} = \frac{(175.6\text{ mm})(144.6\text{ mm})}{(6.0\text{ mm})^2} = 705$$

$$\lambda_p = \frac{0.08E}{F_y} = \frac{0.08(196\,070\text{ MPa})}{(376\text{ MPa})} = 42$$

$$\lambda_r = \frac{1.9E}{F_y} = \frac{1.9(196\,070\text{ MPa})}{(376\text{ MPa})} = 991$$

$\lambda_p = 42 < \lambda = 705 < \lambda_r = 991 \therefore$ inelastic lateral–torsional buckling

2. Lateral–torsional buckling modification factor

$$C_b = \left[3 + \ln\left(\frac{L_b}{d}\right)\right]\left(1 - \frac{d_{ct}}{d}\right)$$

$$C_b = \left[3 + \ln\left(\frac{175.6\text{ mm}}{204\text{ mm}}\right)\right]\left(1 - \frac{30\text{ mm}}{204\text{ mm}}\right) = 2.43 > C_{b,min} = 1.84 \rightarrow \text{OK}$$

3. Nominal flexural strength

$$M_n = C_b\left[1.52 - 0.274\lambda\frac{F_y}{E}\right]M_y$$

$$M_n = (2.43)\left[1.52 - 0.274(705)\frac{376\text{ MPa}}{196\,070\text{ MPa}}\right](7.8\text{ kN·m}) = 21.8\text{ kN·m}$$

4. Cross-sectional strength

$$\frac{M}{M_p} + \left(\frac{P}{P_y}\right)^2 + \frac{\left(\frac{V}{V_p}\right)^4}{1-\left(\frac{P}{P_y}\right)^2} \le 1.0 \quad \overset{P = 0\text{ kN}}{\Longrightarrow} \quad M_{p,v} = M_p\left[1 - \left(\frac{V}{V_p}\right)^4\right]$$

$$M_{p,v} = 11.7\text{ kN·m}\left[1 - \left(\frac{V}{196\text{ kN}}\right)^4\right]$$

V is unknown, try $V = \frac{M_p}{e} = \frac{11.7\text{ kN·m}}{185.1\text{ mm}} = 63\text{ kN}$

$$M_{p,v} = 11.7\text{ kN·m}\left[1 - \left(\frac{63\text{ kN}}{196\text{ kN}}\right)^4\right] = 11.6\text{ kN·m}$$

$M_n = 21.8\text{ kN·m} > M_{p,v} = 11.6\text{ kN·m} \therefore M_n = 11.6\text{ kN·m}$

$$V_n = \frac{M_n}{e} = \frac{11.6\text{ kN·m}}{185.1\text{ mm}} = 63\text{ kN}$$

$V = V_n = 63\text{ kN}, \therefore V_{\text{Dowswell \& Whyte}} = 63\text{ kN}$

Sample calculations for specimen 3A-2-100C-NR:

Initial calculations:

1. Geometric eccentricity

$e = c + t_e = 150.5 \text{ mm} + 9.5 \text{ mm} = 160 \text{ mm}$

2. Cross-sectional properties

$$I_x = \frac{t_w h_0^3}{12} = \frac{(6.5 \text{ mm})(251.2 \text{ mm})^3}{12} = 8586 \cdot 10^3 \text{ mm}^4$$

$$I_y = \frac{h_0 t_w^3}{12} = \frac{(251.2 \text{ mm})(6.5 \text{ mm})^3}{12} = 5749 \text{ mm}^4$$

$J = 4I_y = 4(5749 \text{ mm}^4) = 22\,995 \text{ mm}^4$

$$G = \frac{E}{2.6} = \frac{196\,324 \text{ MPa}}{2.6} = 75\,509 \text{ MPa}$$

3. Cross-sectional strength

$$M_y = \frac{h_0^2 t_w F_y}{6} = \frac{(251.2 \text{ mm})^2 (6.5 \text{ mm})(355 \text{ MPa})}{6} = 24.3 \text{ kN·m}$$

$$M_p = \frac{h_0^2 t_w F_y}{4} = \frac{(251.2 \text{ mm})^2 (6.5 \text{ mm})(355 \text{ MPa})}{4} = 36.5 \text{ kN·m}$$

$P_y = h_0 t_w F_y = (251.2 \text{ mm})(6.5 \text{ mm})(355 \text{ MPa}) = 580 \text{ kN}$

$V_p = 0.6 h_0 t_w F_y = 0.6(251.2 \text{ mm})(6.5 \text{ mm})(355 \text{ MPa}) = 348 \text{ kN}$

Fabricator's Design Procedure (3A-2-100C-NR):

1. Shear strength assuming elastic stress distribution

$$V_1 = \frac{0.66 h_0 t_w F_y}{1.5} = \frac{0.66(251.2 \text{ mm})(6.5 \text{ mm})(355 \text{ MPa})}{1.5} = 255 \text{ kN}$$

2. Lateral–torsional buckling of net section

$$t_{w,min} = 0.877 \sqrt{\frac{c h_0}{\omega_2} \frac{F_y}{E}}$$

$$t_{w,min} = 0.877 \sqrt{\frac{(150.5 \text{ mm})(251.2 \text{ mm})}{1.0} \frac{355 \text{ MPa}}{196\,324 \text{ MPa}}} = 7.3 \text{ mm}$$

$t_w = 6.5 \text{ mm} < t_{w,min} = 7.3 \text{ mm}$, ∴ LTB prevents attainment of M_p

$$M_u = \frac{\omega_2 \pi}{c}\sqrt{EI_y GJ}$$

$$M_u = \frac{(1.0)\pi}{150.5\text{ mm}}\sqrt{(196\,324\text{ MPa})(5749\text{ mm}^4)(75\,509\text{ MPa})(22\,995\text{ mm}^4)}$$

$$M_u = 29.2\text{ kN·m}$$

$$V_2 = \frac{M_u}{e} = \frac{29.2\text{ kN·m}}{160\text{ mm}} = 183\text{ kN}$$

3. Local web buckling (AISC 2011)

$$\frac{c}{d} = \frac{150.5\text{ mm}}{313\text{ mm}} = 0.48 < 2 \rightarrow \text{OK}$$

$$\frac{d_c}{d} = \frac{31.3\text{ mm}}{313\text{ mm}} = 0.1 < 0.2 \rightarrow \text{OK}$$

Geometry satisfied, therefore appropriate to use method

$$f_d = 3.5 - 7.5\left(\frac{d_{ct}}{d}\right) = 3.5 - 7.5\left(\frac{31.3\text{ mm}}{313\text{ mm}}\right) = 2.75$$

$$F_{cr} = 0.62\pi E\frac{{t_w}^2}{ch_0}f_d$$

$$F_{cr} = 0.62\pi(196\,324\text{ MPa})\frac{(6.5\text{ mm})^2}{(150.5\text{ mm})(251.2\text{ mm})}(2.75) = 1175\text{ MPa}$$

$F_{cr} = 1175\text{ MPa} \not< F_y = 355\text{ MPa}$, ∴ local buckling does not govern

4. Cross-sectional strength

$P = 100\text{ kN} < P_y = 580\text{ kN}$, ∴ cross-section will not yield under pure compression

5. Axial and bending strength interaction

$$\frac{M}{M_p} + \left(\frac{P}{P_y}\right)^2 \le 1.0 \quad \Longrightarrow \quad V\cdot e = M_p\left[1.0 - \left(\frac{P}{P_y}\right)^2\right]$$

$$V_3 = \frac{M_p}{e}\left[1.0 - \left(\frac{P}{P_y}\right)^2\right] = \frac{36.4\text{ kN·m}}{160\text{ mm}}\left[1.0 - \left(\frac{100\text{ kN}}{580\text{ kN}}\right)^2\right] = 221\text{ kN}$$

6. Axial compression capacity (CSA 2014)

$$\lambda = \frac{KL}{r}\sqrt{\frac{F_y}{\pi^2 E}} = \frac{(1.0)(150.5\text{ mm})}{1.88\text{ mm}}\sqrt{\frac{355\text{ MPa}}{\pi^2(196\,324\text{ MPa})}} = 1.084$$

$$C_r = h_0 t_w F_y\left(1+\lambda^{2n}\right)^{-1/n} = (580\text{ kN})\left(1+(1.084)^{2(1.34)}\right)^{-1/1.34} = 317\text{ kN}$$

7. Axial compression and bending interaction (CSA 2014)

$$\frac{C_f}{C_r} + \frac{U_1 M_f}{M_r} \le 1.0 \quad \Longrightarrow \quad V\cdot e = \frac{M_r}{U_1}\left[1.0 - \frac{C_f}{C_r}\right]$$

$$C_e = \frac{\pi^2 E I_x}{L^2} = \frac{\pi^2(196\,324\text{ MPa})\left(8586\cdot 10^3\text{ mm}^4\right)}{(160\text{ mm})^2} = 649\,867\text{ kN}$$

$$\omega_1 = 0.6 - 0.4\kappa = 0.6 - 0.4(0) = 0.6$$

$$U_{1x} = \frac{\omega_1}{1 - \frac{C_f}{C_e}} = \frac{0.6}{1 - \frac{100\text{ kN}}{649\,867\text{ kN}}} = 0.6$$

Use $U_{1x} = 1.0$ assuming member is laterally braced

$$M_u = \frac{\omega_2 \pi}{e}\sqrt{EI_y GJ}$$

$$M_u = \frac{(1.0)\pi}{160\text{ mm}}\sqrt{(196\,324\text{ MPa})(5749\text{ mm}^4)(75\,509\text{ MPa})(22\,995\text{ mm}^4)}$$

$$M_u = 27.5\text{ kN}\cdot\text{m}$$

$$0.67M_p = 0.67(36.4\text{ kN}\cdot\text{m}) = 24.3\text{ kN}\cdot\text{m}$$

$$M_u = 27.5\text{ kN}\cdot\text{m} > 0.67M_p = 24.3\text{ kN}\cdot\text{m}, \therefore M_r = 1.15M_p\left[1 - \frac{0.28M_p}{M_u}\right] \le M_p$$

$$M_r = 1.15(36.4\text{ kN}\cdot\text{m})\left[1 - \frac{0.28(36.4\text{ kN}\cdot\text{m})}{(27.5\text{ kN}\cdot\text{m})}\right] = 26.3\text{ kN}\cdot\text{m}$$

$$M_r = 26.3\text{ kN}\cdot\text{m} < M_p = 36.4\text{ kN}\cdot\text{m} \rightarrow \text{OK}$$

$$V_4 = \frac{M_r}{e}\left[1.0 - \frac{C_f}{C_r}\right] = \frac{26.3\text{ kN}\cdot\text{m}}{(160\text{ mm})}\left[1.0 - \frac{100\text{ kN}}{317\text{ kN}}\right] = 113\text{ kN}$$

$$V_{Fabricator} = \text{minimum of: } \left\{ \begin{matrix} V_1 = 255 \text{ kN} \\ V_2 = 183 \text{ kN} \\ V_3 = 221 \text{ kN} \\ V_4 = 113 \text{ kN} \end{matrix} \right\} = 113 \text{ kN}$$

AISC *Manual* (AISC 2011) Design Procedure (3A-2-100C-NR):

1. Local web buckling (critical stress determined in Fabricator's method)

$F_{cr} = 1175 \text{ MPa} \not< F_y = 355 \text{ MPa}, \therefore F_{cr} = 355 \text{ MPa}$

$M_n = S_{net}F_{cr} = S_{net}F_y = M_y = 24.3 \text{ kN·m}$

$$V_{Manual} = \frac{M_n}{e} = \frac{24.3 \text{ kN·m}}{160 \text{ mm}} = 152 \text{ kN}$$

AISC *Specification* (AISC 2010) Section F11 Design Procedure (3A-2-100C-NR):

1. Nondimensional slenderness parameter

$$\frac{L_b d}{t^2} = \frac{ch_0}{{t_w}^2} = \frac{(150.5 \text{ mm})(251.2 \text{ mm})}{(6.5 \text{ mm})^2} = 895$$

$$\frac{0.08E}{F_y} = \frac{0.08(196\,324 \text{ MPa})}{(355 \text{ MPa})} = 44$$

$$\frac{1.9E}{F_y} = \frac{1.9(196\,324 \text{ MPa})}{(355 \text{ MPa})} = 1050$$

$$\frac{0.08E}{F_y} = 44 < \frac{L_b d}{t^2} = 895 < \frac{1.9E}{F_y} = 1050 \therefore \text{inelastic lateral–torsional buckling}$$

2. Nominal flexural strength

$$M_n = C_b \left[1.52 - 0.274 \left(\frac{L_b d}{t^2} \right) \frac{F_y}{E} \right] M_y \quad \Longrightarrow \quad M_n = C_b \left[1.52 - 0.274 \left(\frac{ch_0}{{t_w}^2} \right) \frac{F_y}{E} \right] M_y$$

$$M_n = (1.67) \left[1.52 - 0.274(895) \frac{355 \text{ MPa}}{196\,324 \text{ MPa}} \right] (24.3 \text{ kN·m}) = 43.7 \text{ kN·m}$$

$M_n = 43.7 \text{ kN·m} > M_p = 36.5 \text{ kN·m}, \therefore M_n = 36.5 \text{ kN·m}$

$$V_{Specification} = \frac{M_n}{e} = \frac{36.5 \text{ kN·m}}{160 \text{ mm}} = 228 \text{ kN}$$

Dowswell and Whyte (2014) Design Procedure (3A-2-100C-NR):

1. Slenderness parameter and slenderness limits (similar to AISC *Specification*)

$$\lambda = \frac{L_b h_0}{t_w^2} = \frac{(150.5\text{ mm})(251.2\text{ mm})}{(6.5\text{ mm})^2} = 895$$

$$\lambda_p = \frac{0.08E}{F_y} = \frac{0.08(196\,324\text{ MPa})}{(355\text{ MPa})} = 44$$

$$\lambda_r = \frac{1.9E}{F_y} = \frac{1.9(196\,324\text{ MPa})}{(355\text{ MPa})} = 1050$$

$\lambda_p = 44 < \lambda = 895 < \lambda_r = 1050 \therefore$ inelastic lateral–torsional buckling

2. Lateral–torsional buckling modification factor

$$C_b = \left[3 + \ln\left(\frac{L_b}{d}\right)\right]\left(1 - \frac{d_{ct}}{d}\right)$$

$$C_b = \left[3 + \ln\left(\frac{150.5\text{ mm}}{313\text{ mm}}\right)\right]\left(1 - \frac{31.3\text{ mm}}{313\text{ mm}}\right) = 2.04 > C_{b,min} = 1.84 \rightarrow \text{OK}$$

3. Nominal flexural strength

$$M_n = C_b\left[1.52 - 0.274\lambda\frac{F_y}{E}\right]M_y$$

$$M_n = (2.04)\left[1.52 - 0.274(895)\frac{355\text{ MPa}}{196\,324\text{ MPa}}\right](24.3\text{ kN·m}) = 53.4\text{ kN·m}$$

4. Cross-sectional strength

$$\frac{M}{M_p} + \left(\frac{P}{P_y}\right)^2 + \frac{\left(\frac{V}{V_p}\right)^4}{1 - \left(\frac{P}{P_y}\right)^2} \le 1.0 \quad \Longrightarrow \quad M_{p,vp} = M_p\left[1 - \left(\frac{P}{P_y}\right)^2 - \frac{\left(\frac{V}{V_p}\right)^4}{1 - \left(\frac{P}{P_y}\right)^2}\right]$$

$$M_{p,vp} = 36.5\text{ kN·m}\left[1 - \left(\frac{100\text{ kN}}{580\text{ kN}}\right)^2 - \frac{\left(\frac{V}{348\text{ kN}}\right)^4}{1 - \left(\frac{100\text{ kN}}{580\text{ kN}}\right)^2}\right]$$

V is unknown, try $V = \frac{M_p}{e} = \frac{36.5\text{ kN·m}}{160\text{ mm}} = 228\text{ kN}$

$$M_{p,vp} = 36.5\text{ kN·m}\left[1 - \left(\frac{100\text{ kN}}{580\text{ kN}}\right)^2 - \frac{\left(\frac{228\text{ kN}}{348\text{ kN}}\right)^4}{1 - \left(\frac{100\text{ kN}}{580\text{ kN}}\right)^2}\right] = 31.6\text{ kN·m}$$

$M_n = 53.4\text{ kN·m} > M_{p,vp} = 31.6\text{ kN·m} \therefore M_n = 31.6\text{ kN·m}$

$$V_n = \frac{M_n}{e} = \frac{31.6\ \text{kN·m}}{160\ \text{mm}} = 197\ \text{kN}$$

$V = 228\ \text{kN} \neq V_n = 197\ \text{kN}$, ∴ try $V = 197\ \text{kN}$

$$M_{p,vp} = 36.5\ \text{kN·m}\left[1 - \left(\frac{100\ \text{kN}}{580\ \text{kN}}\right)^2 - \frac{\left(\frac{197\ \text{kN}}{348\ \text{kN}}\right)^4}{1 - \left(\frac{100\ \text{kN}}{580\ \text{kN}}\right)^2}\right] = 31.6\ \text{kN·m}$$

$M_n = 53.4\ \text{kN·m} > M_{p,vp} = 31.6\ \text{kN·m}$ ∴ $M_n = 31.6\ \text{kN·m}$

$$V_n = \frac{M_n}{e} = \frac{31.6\ \text{kN·m}}{160\ \text{mm}} = 197\ \text{kN}$$

$V = V_n = 197\ \text{kN}$, ∴ $V_{\text{Dowswell \& Whyte}} = 197\ \text{kN}$

APPENDIX B: MATERIAL DATA

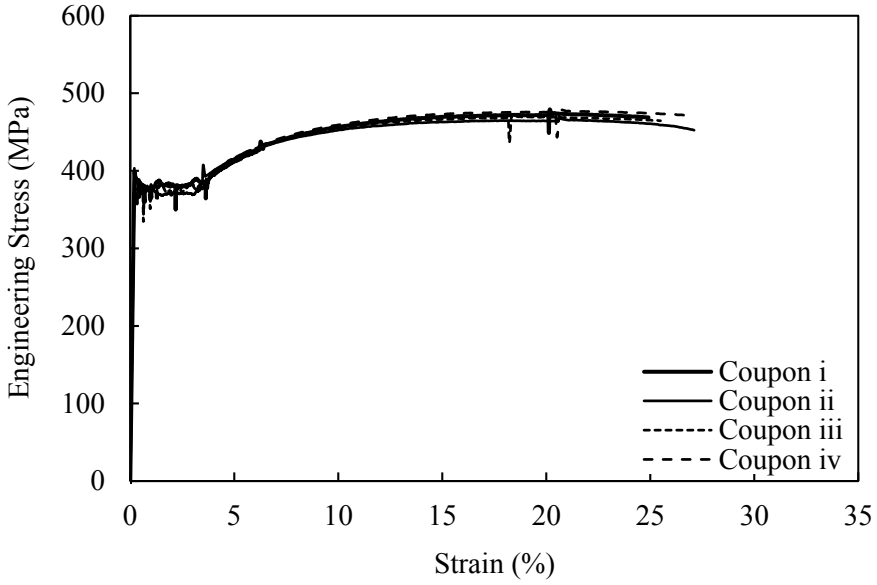

Figure B-1: Stress–strain curves for Beam I

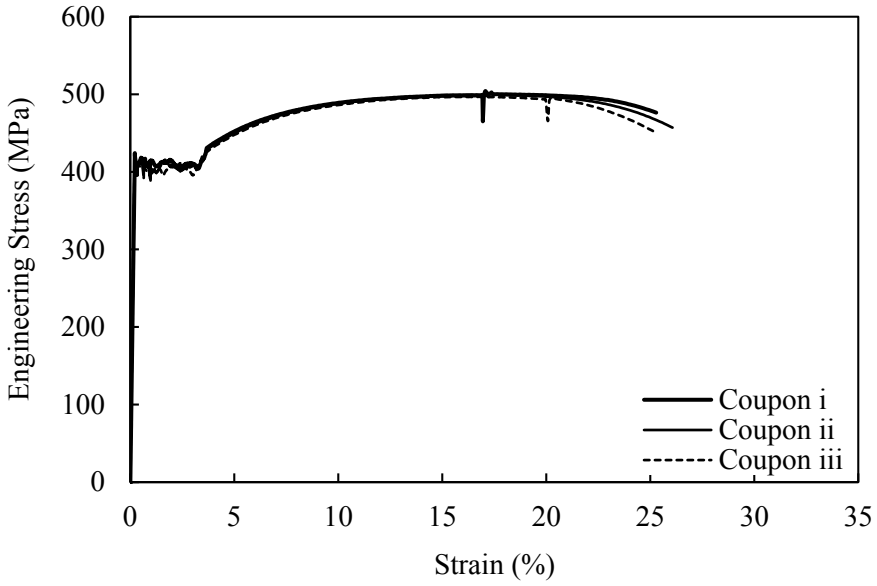

Figure B-2: Stress–strain curves for Beam II

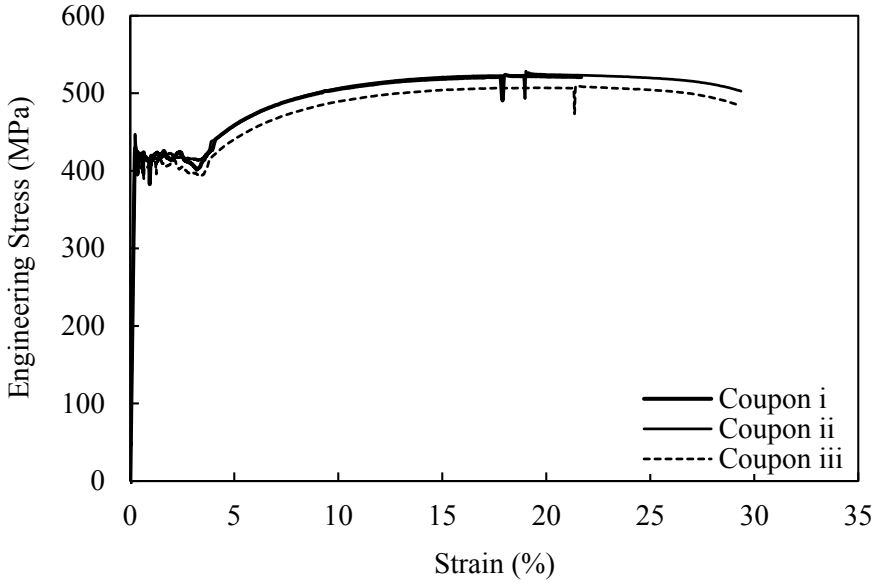

Figure B-3: Stress–strain curves for Beam III

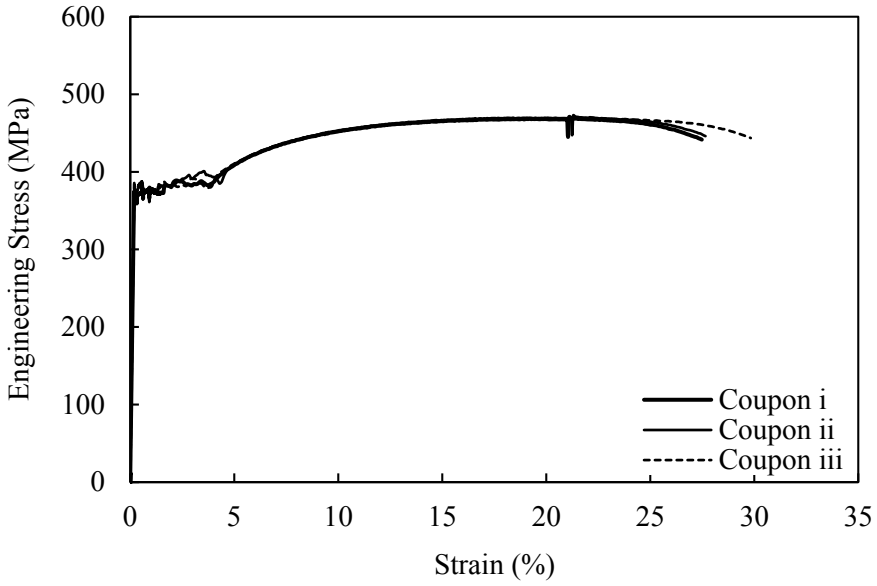

Figure B-4: Stress–strain curves for Beam IV

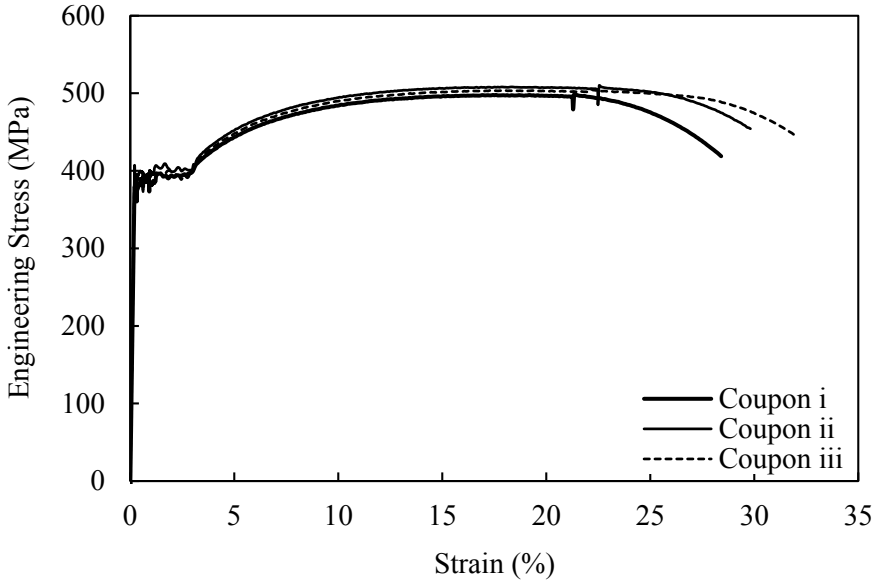

Figure B-5: Stress–strain curves for Beam V

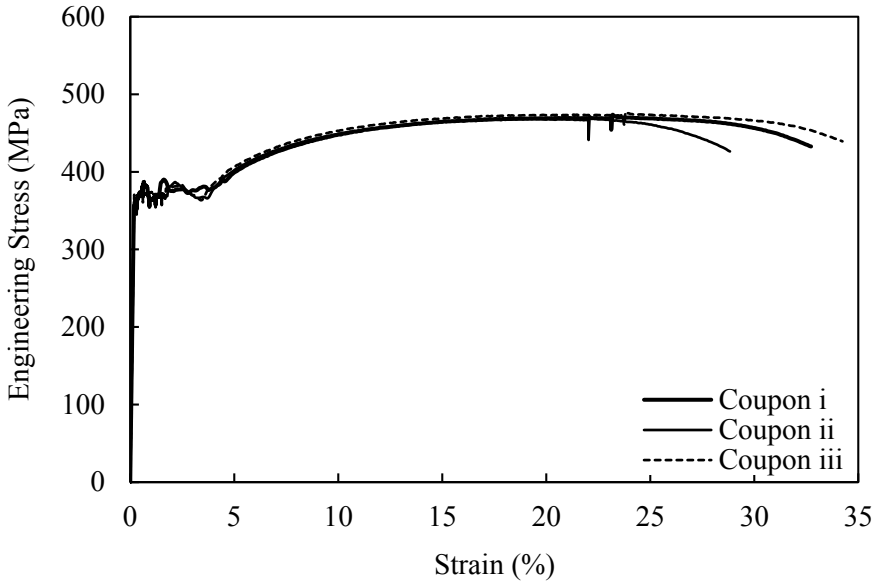

Figure B-6: Stress–strain curves for Beam VI

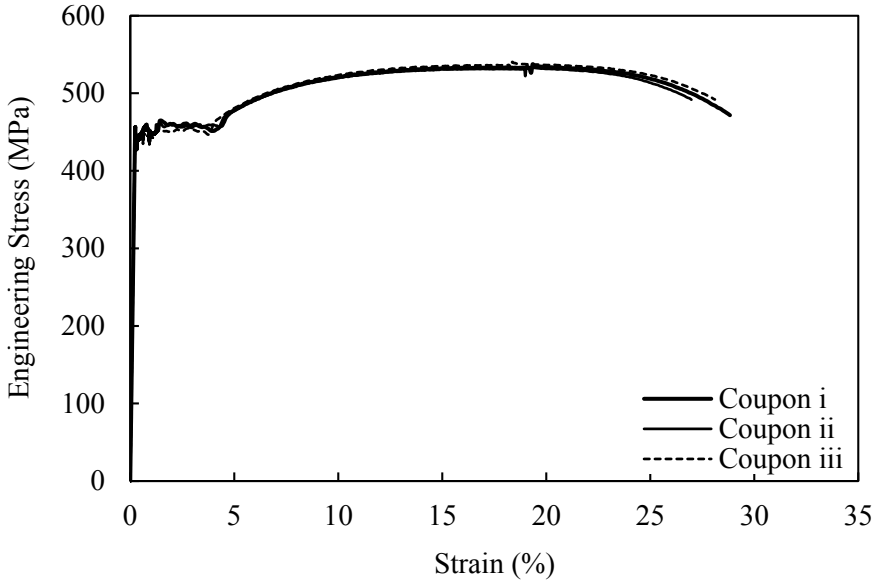

Figure B-7: Stress–strain curves for Beam VII

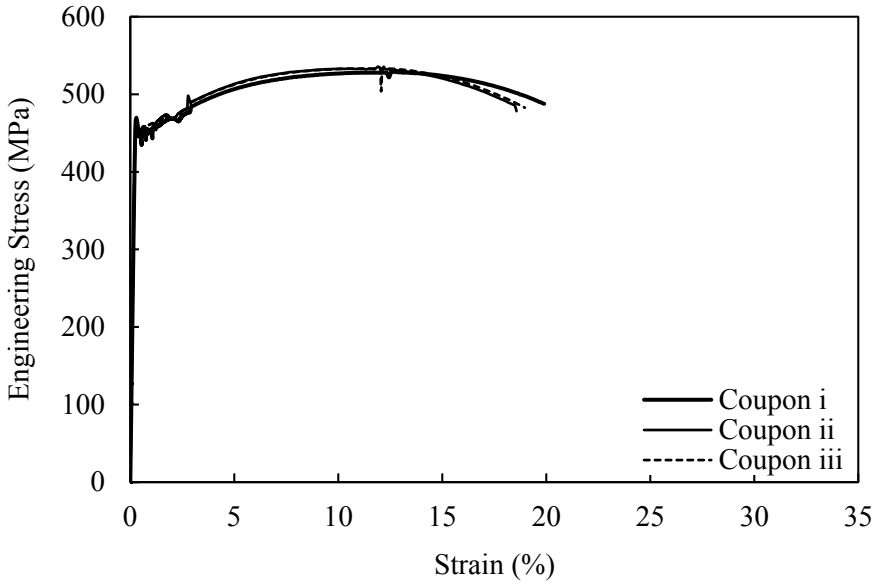

Figure B-8: Stress–strain curves for End-plate 1

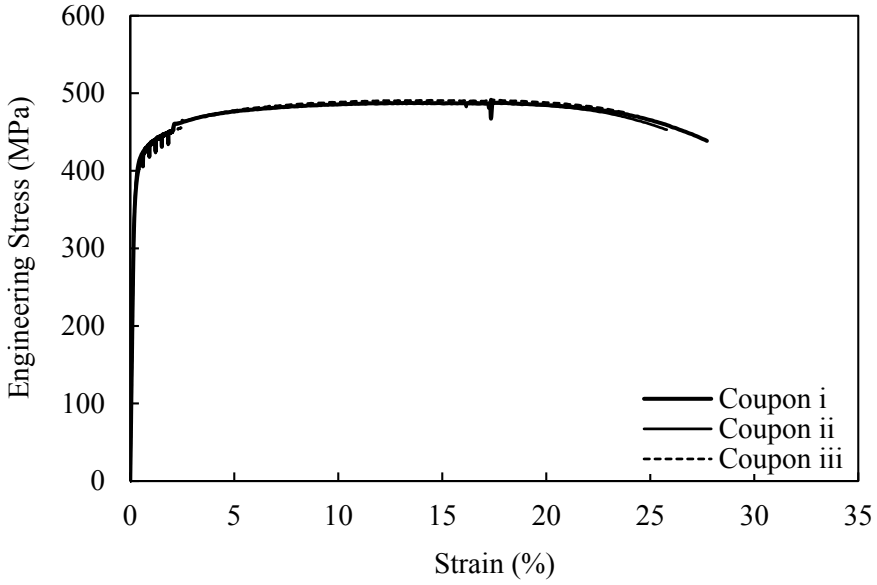

Figure B-9: Stress–strain curves for End-plate 2

APPENDIX C: RESPONSE CURVES

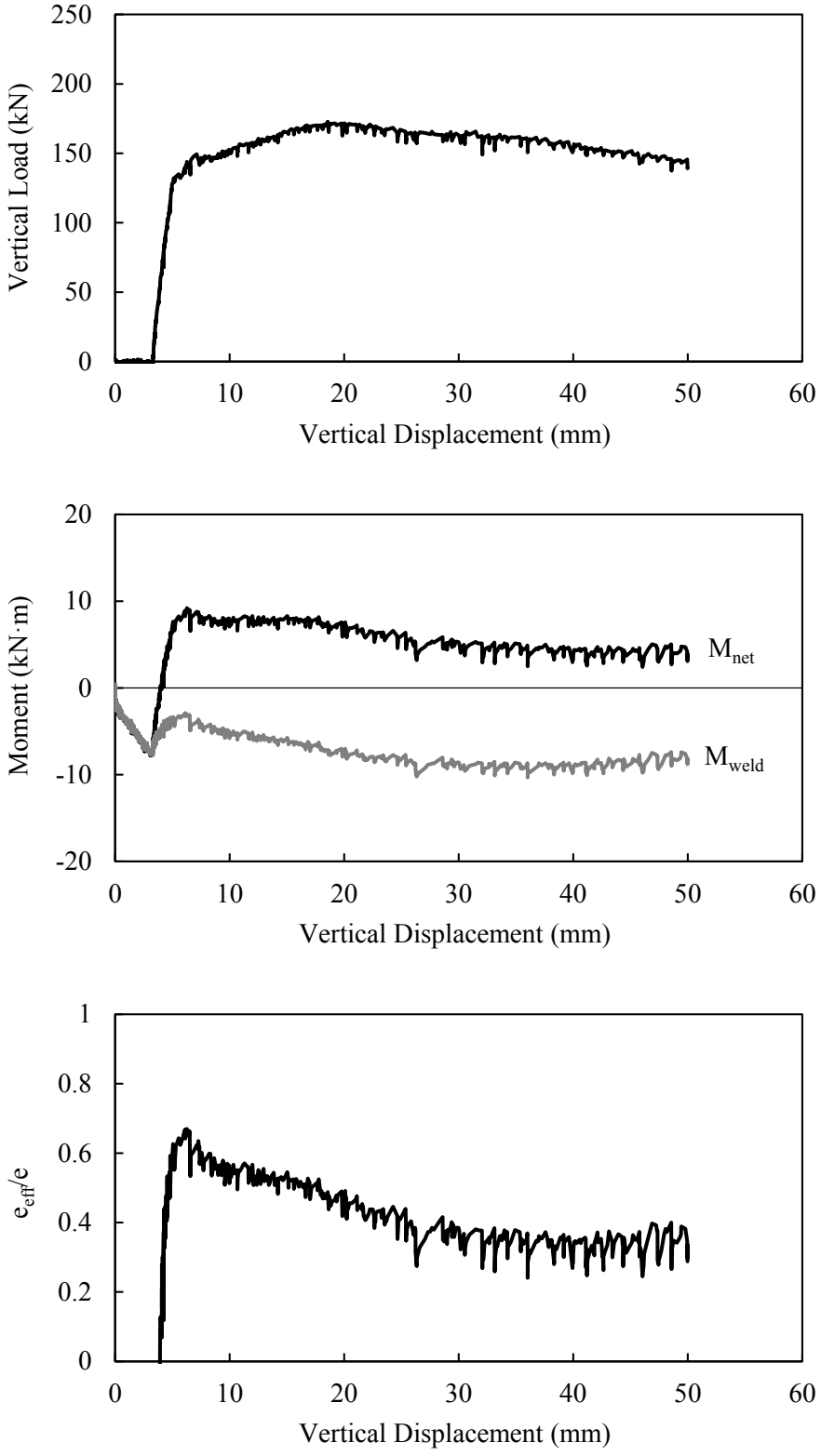

Figure C-1: Specimen 2A-1-0-R

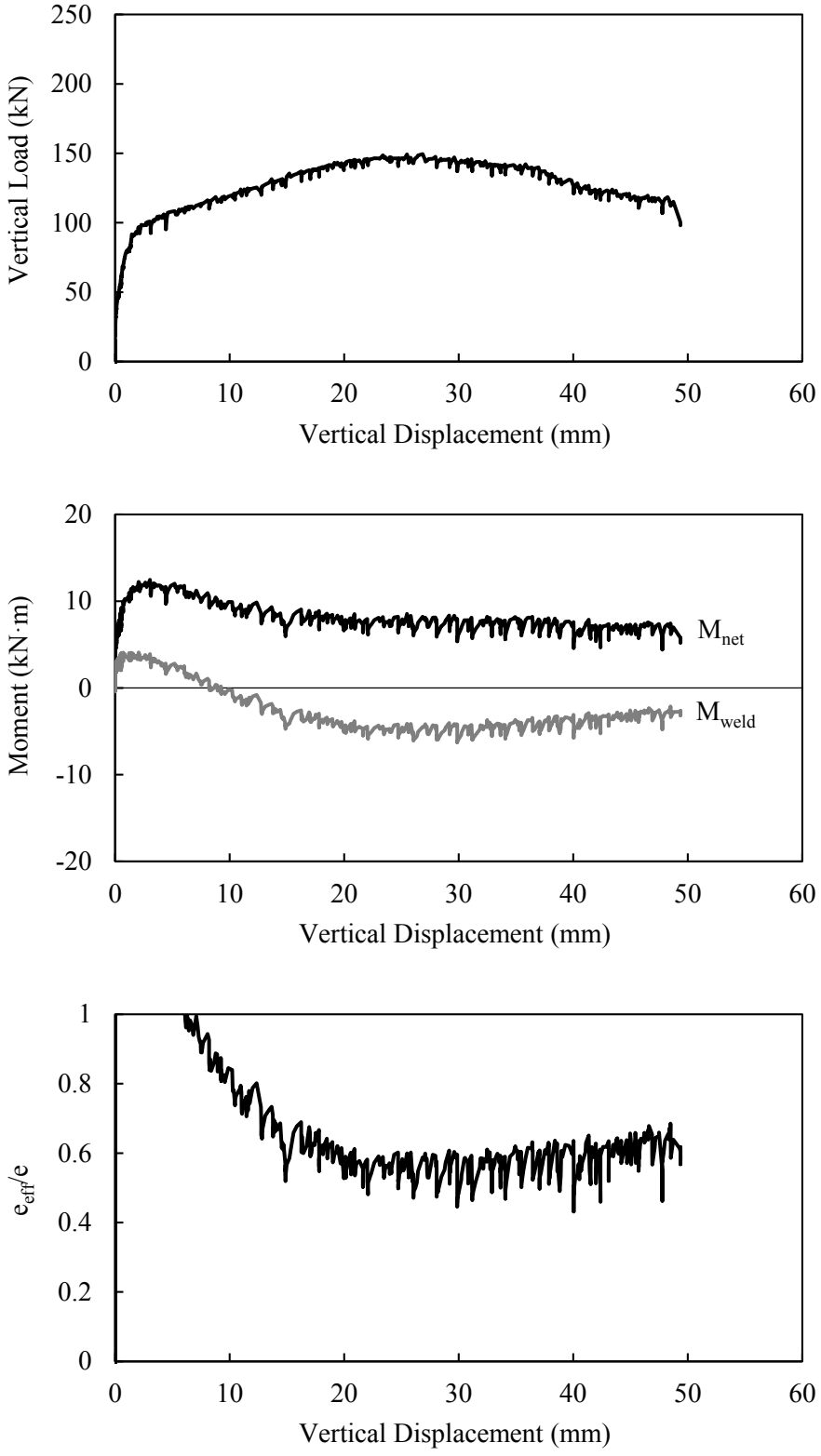

Figure C-2: Specimen 2A-1-0-NR

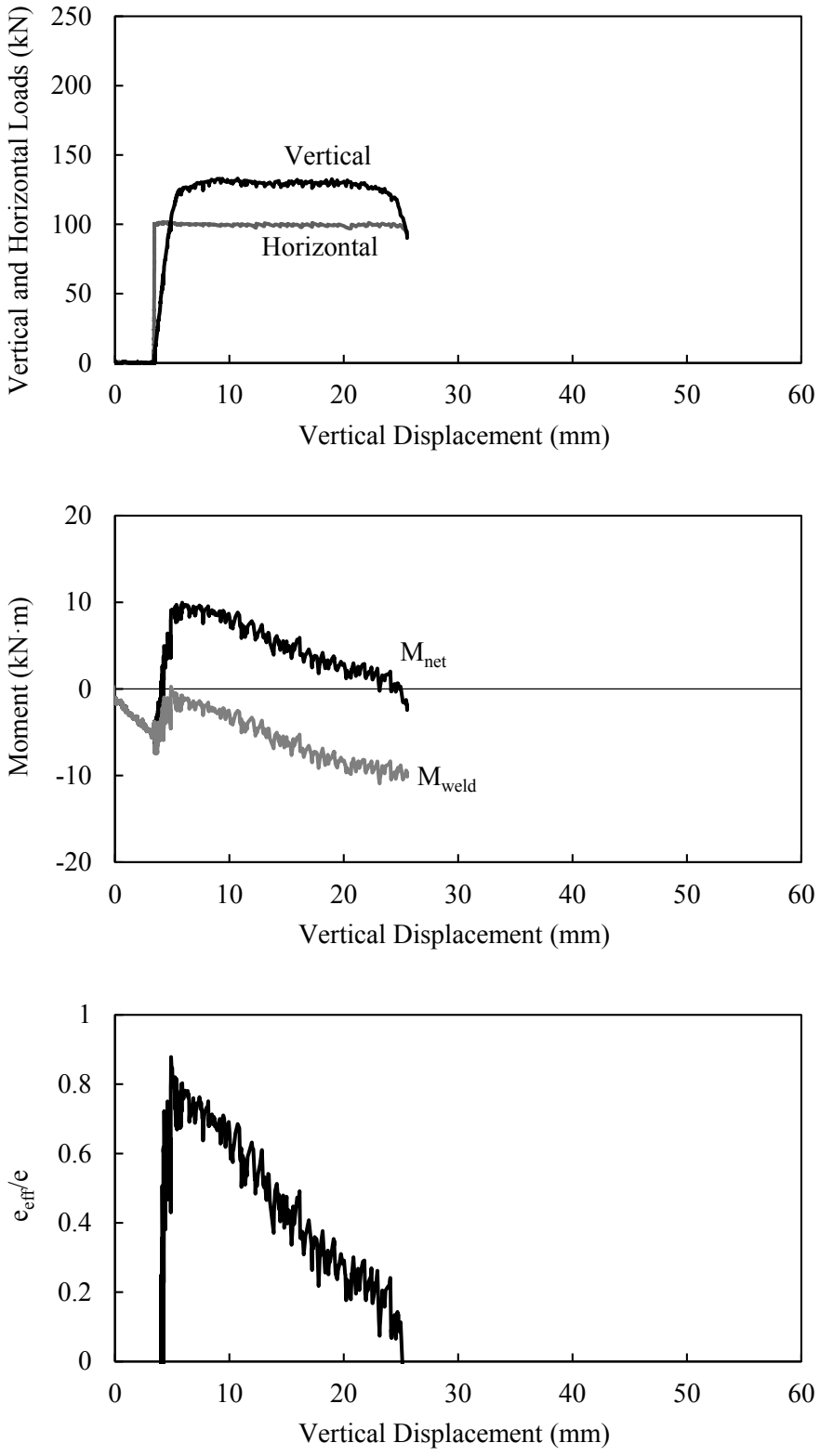

Figure C-3: Specimen 2A-1-100C-R

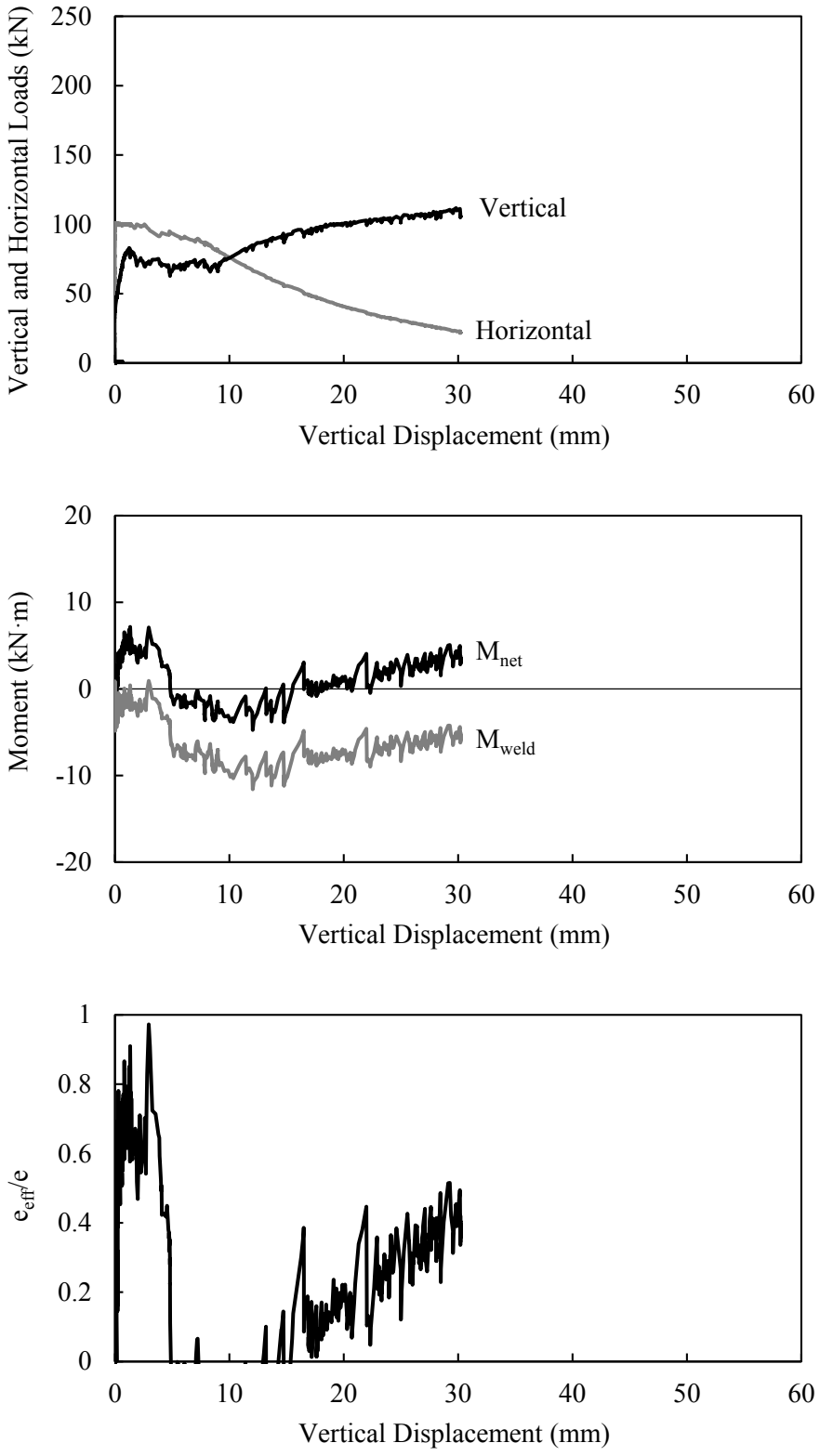

Figure C-4: Specimen 2A-1-100C-NR

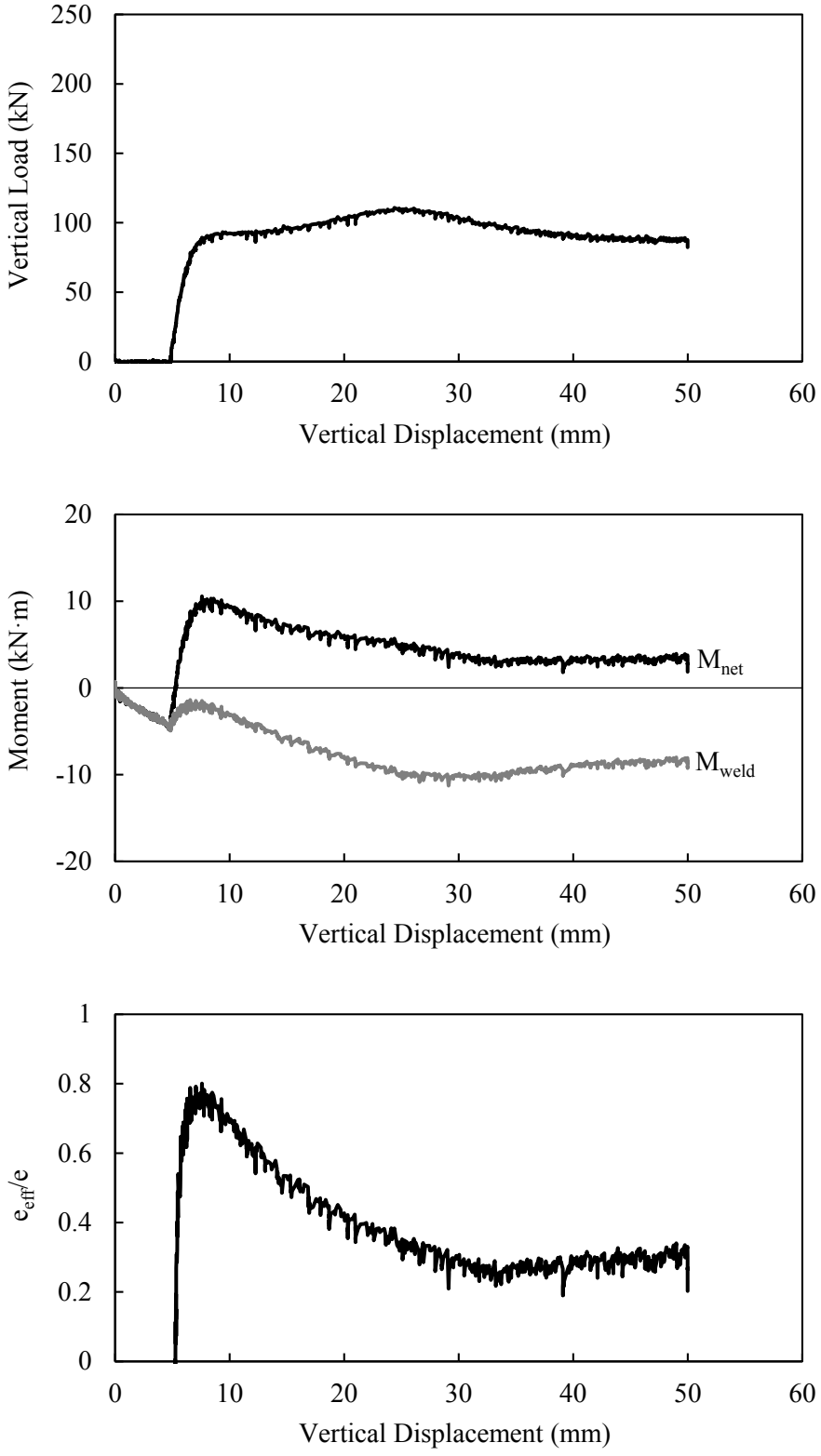

Figure C-5: Specimen 2A-2-0-R

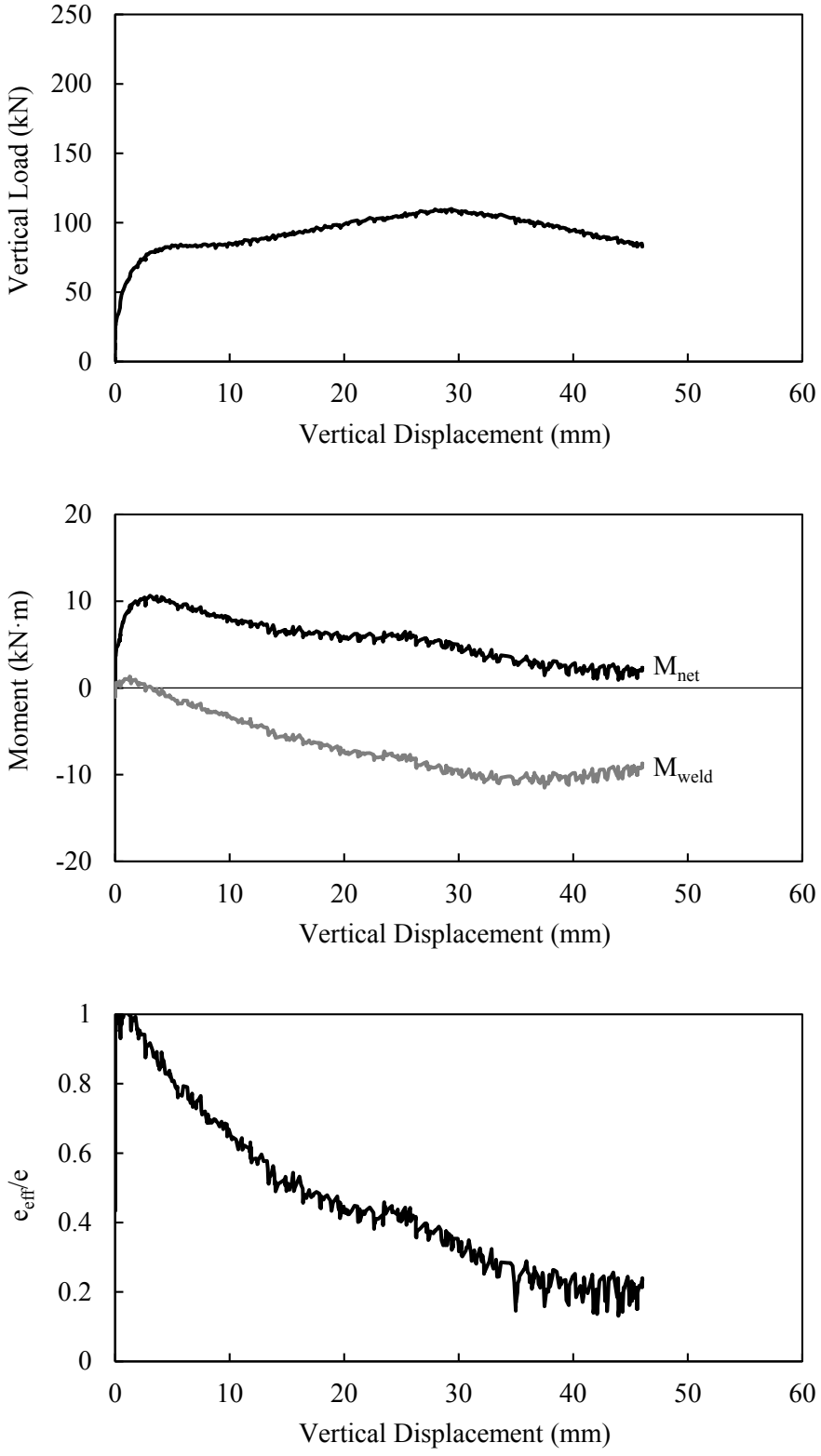

Figure C-6: Specimen 2A-2-0-NR

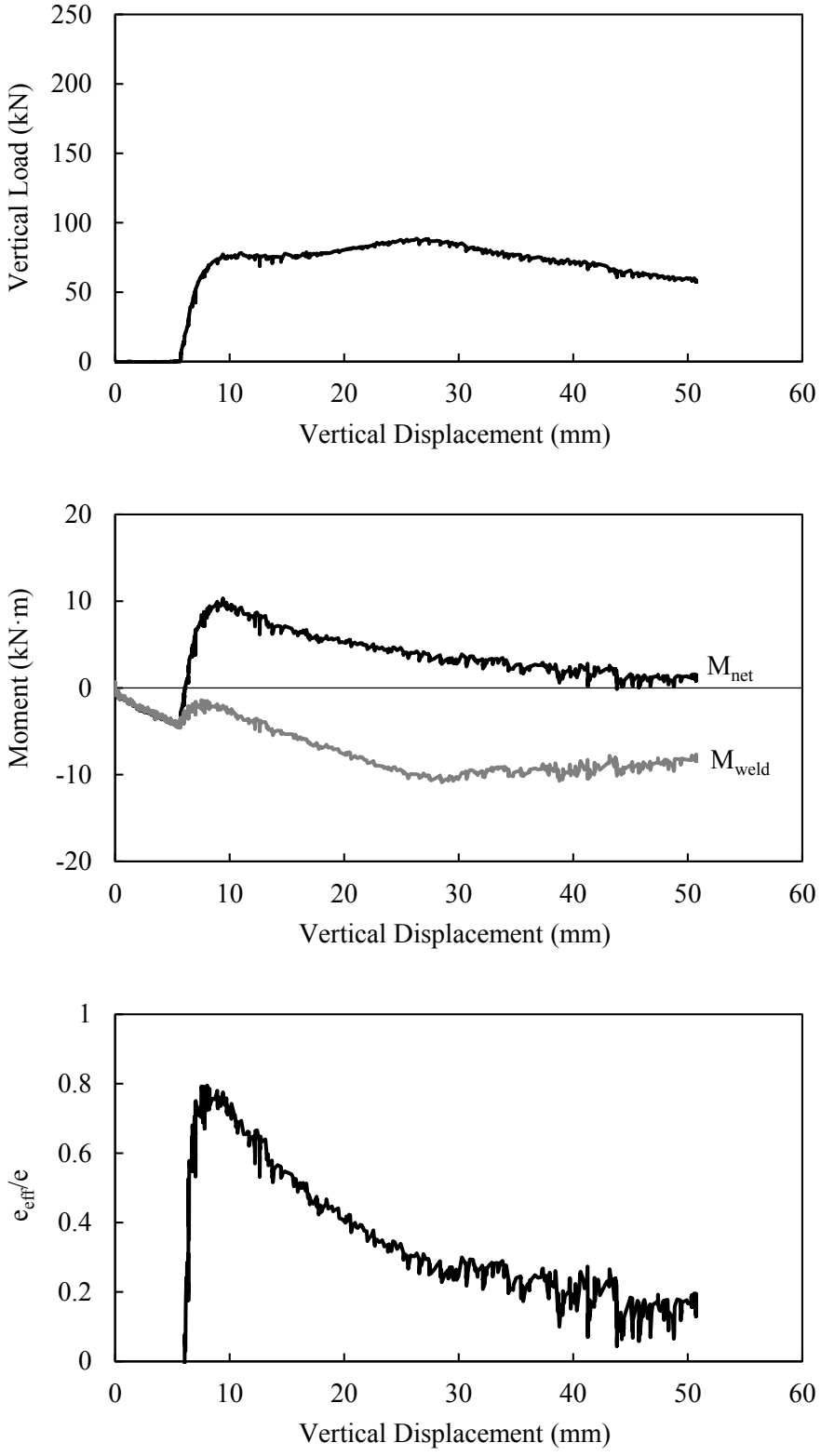

Figure C-7: Specimen 2A-3-0-R

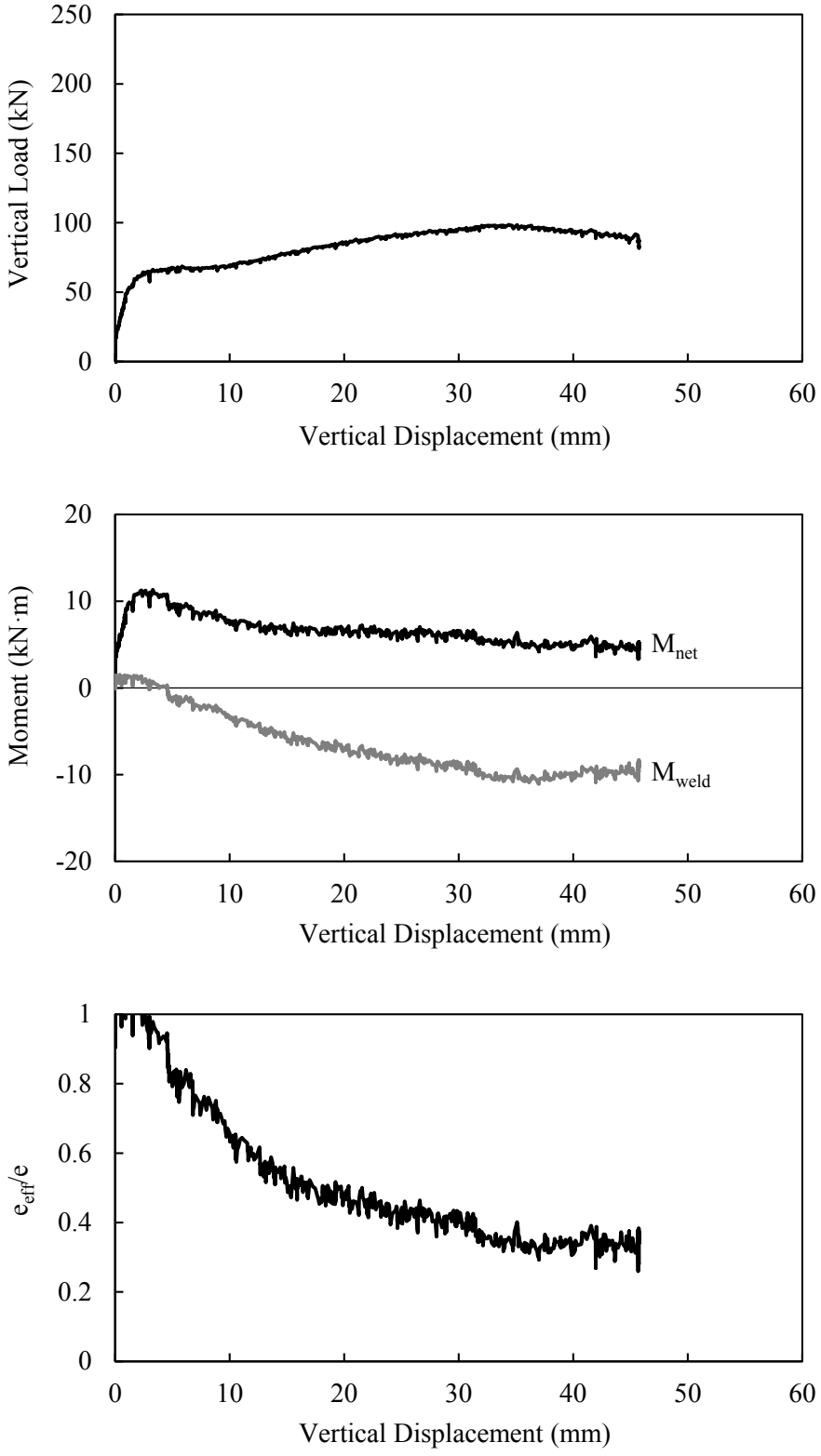

Figure C-8: Specimen 2A-3-0-NR

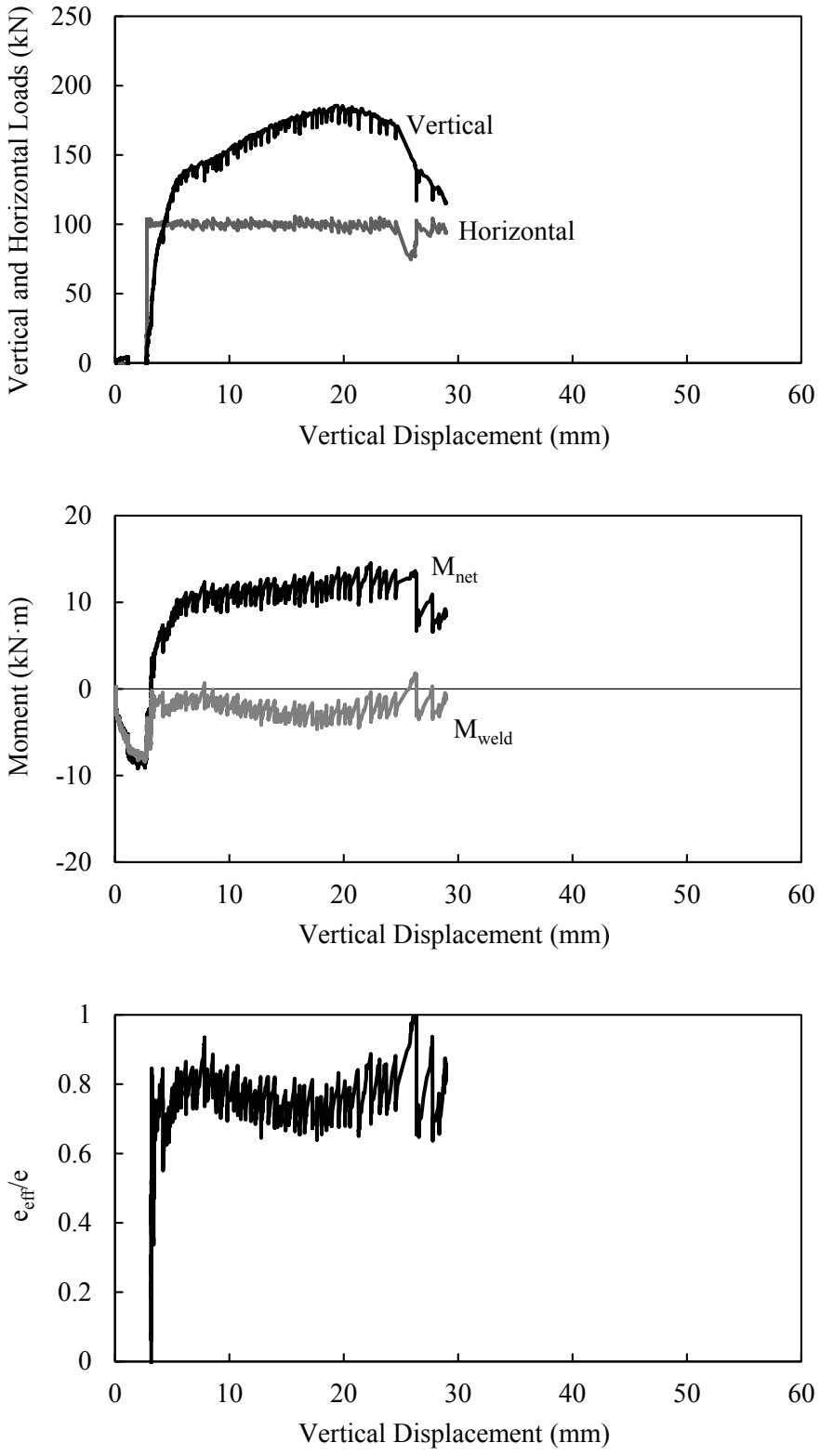

Figure C-9: Specimen 2B-1-100T-R

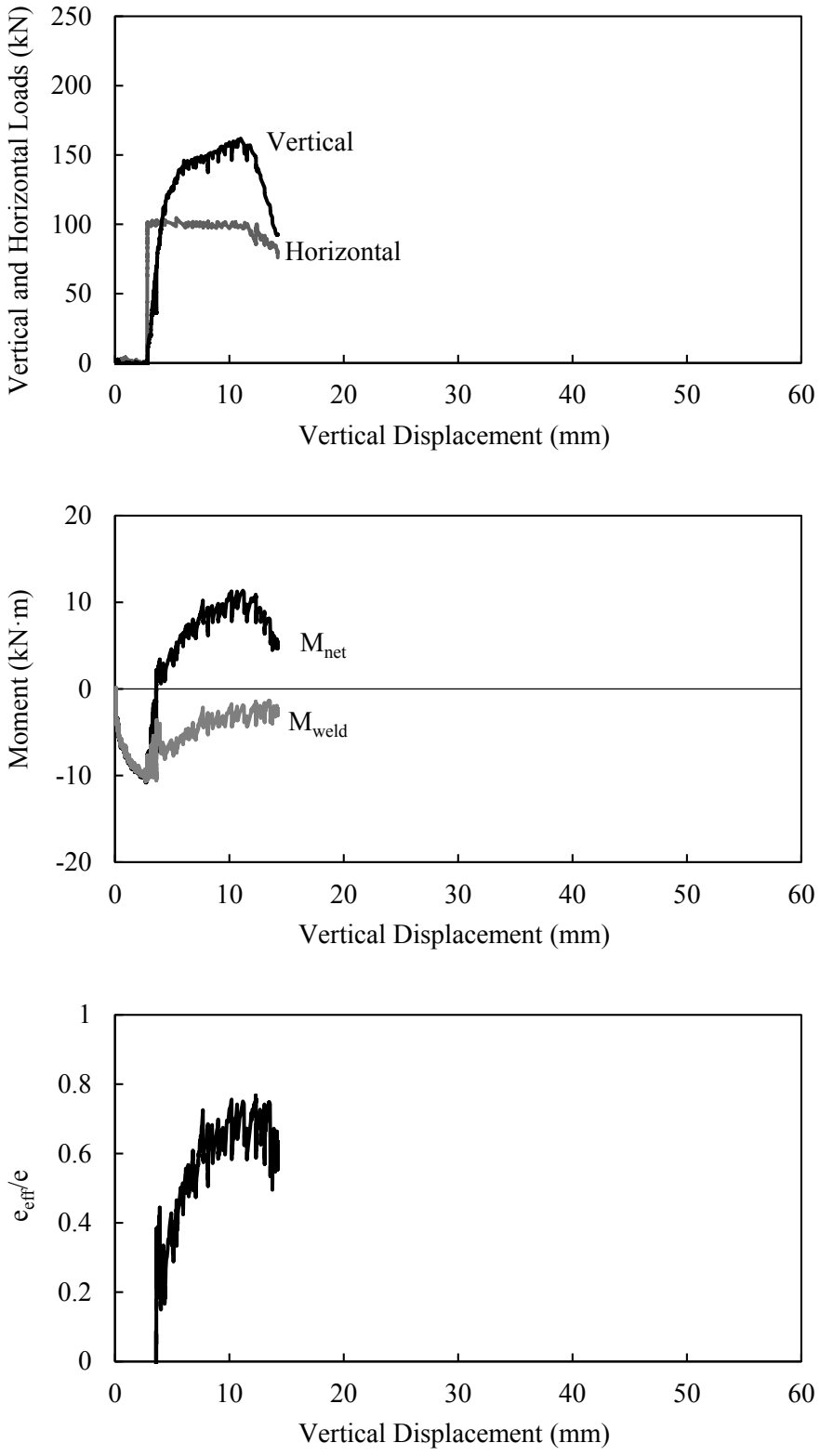

Figure C-10: Specimen 2B-1-100C-R

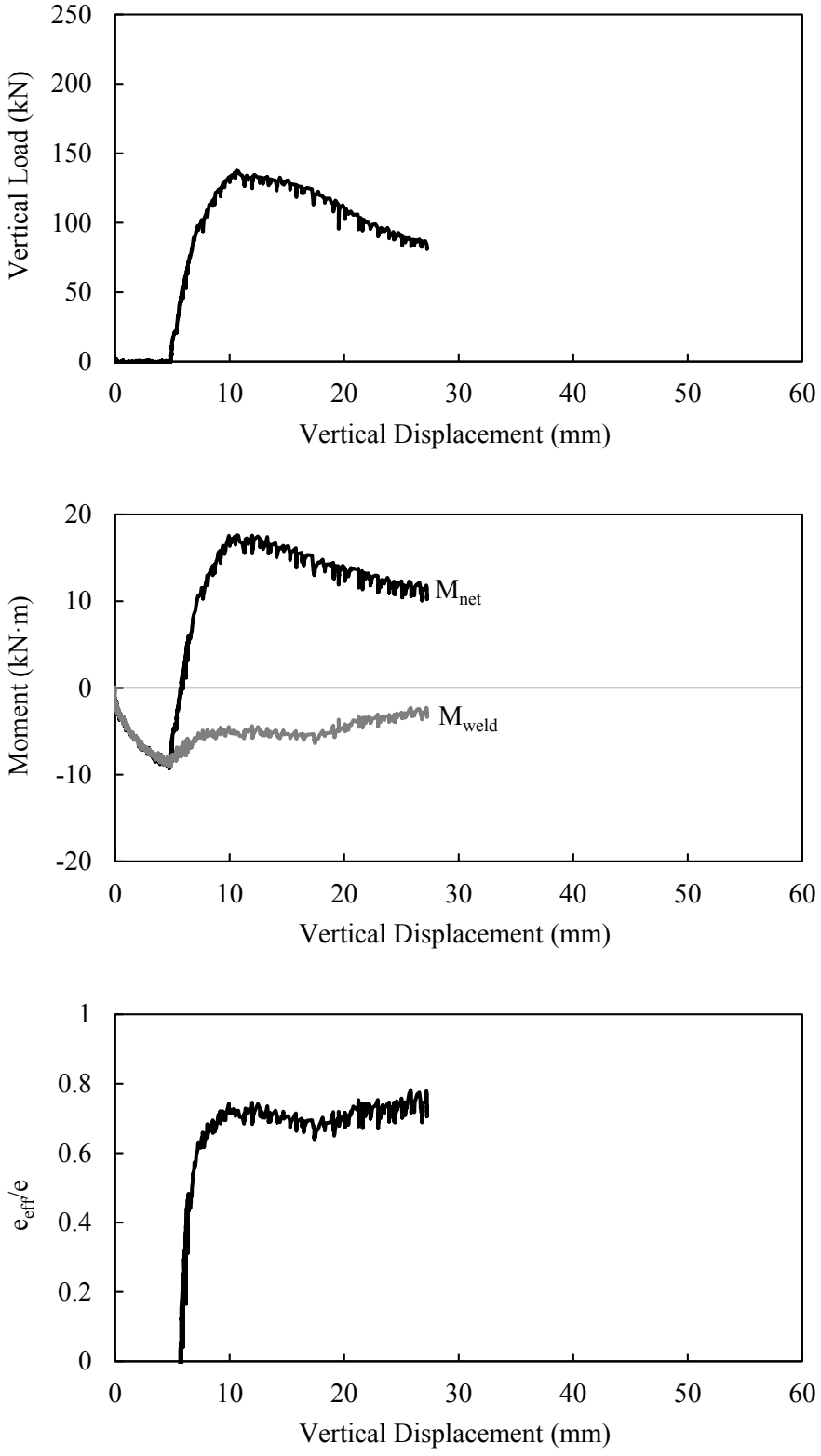

Figure C-11: Specimen 2B-3-0-R

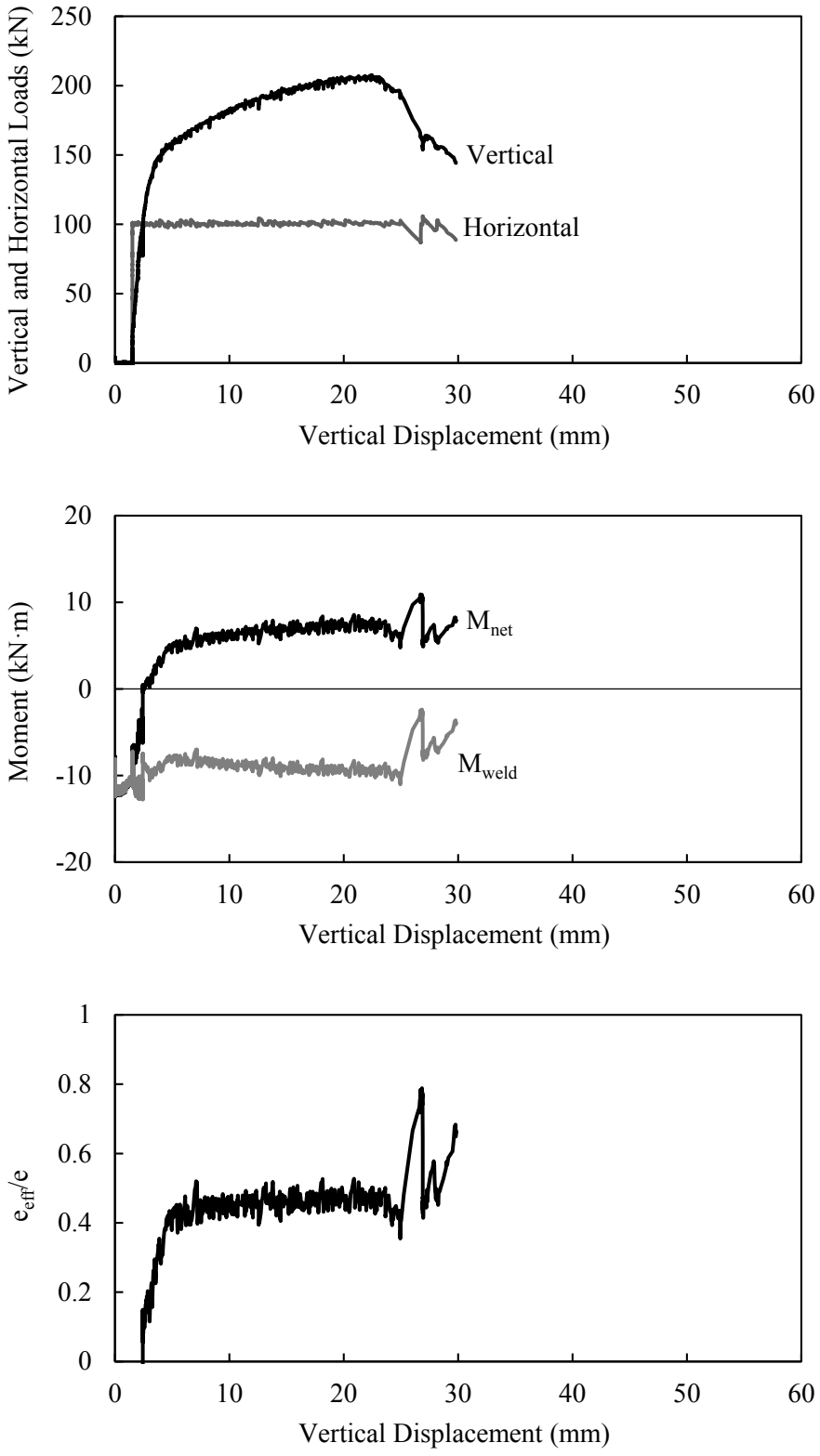

Figure C-12: Specimen 2C-1-100T-R

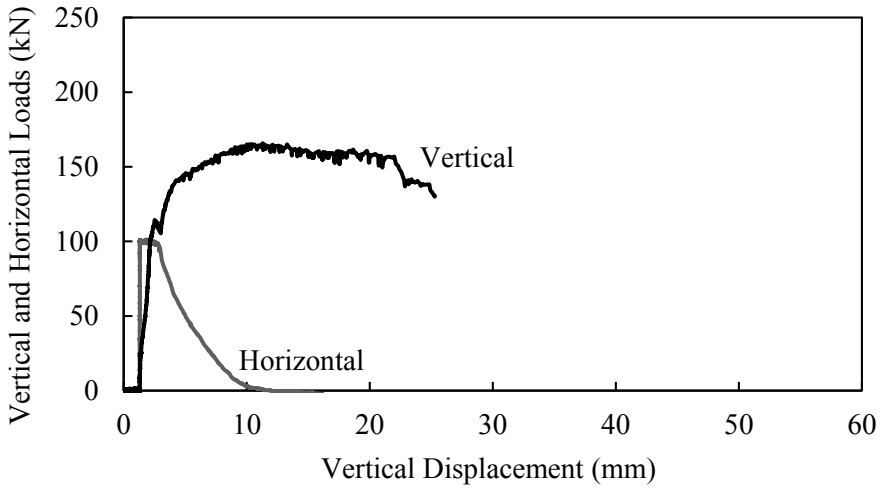

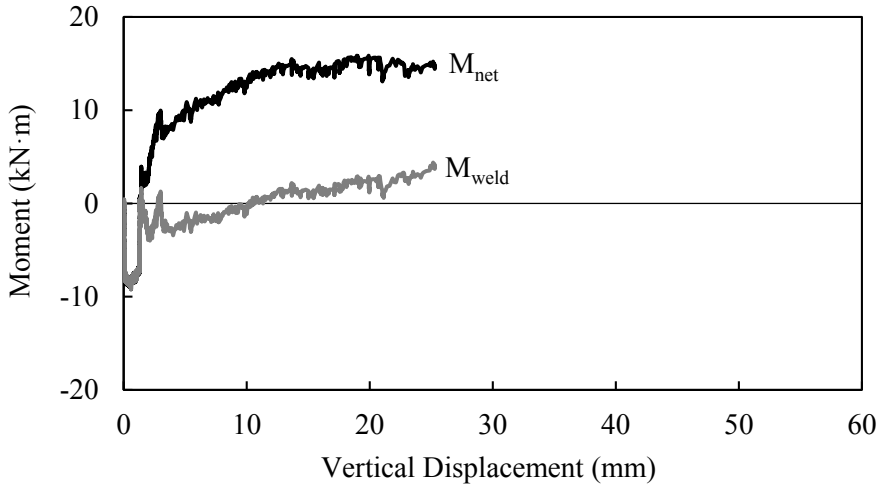

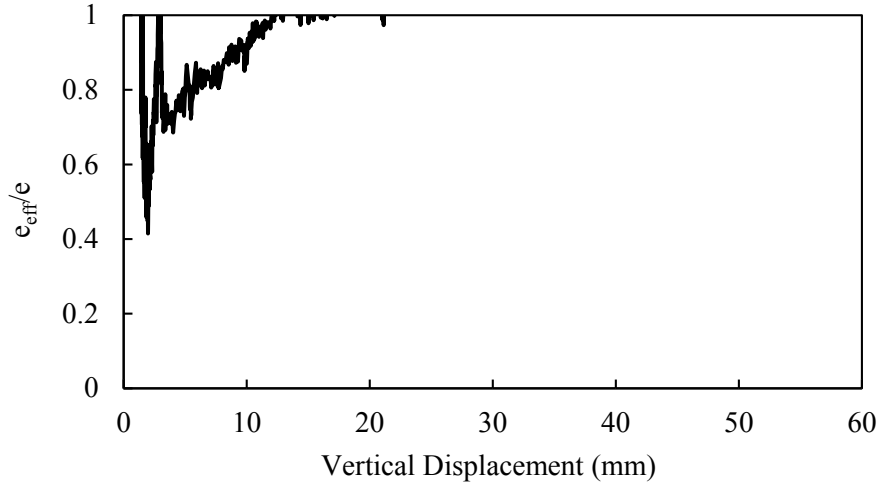

Figure C-13: Specimen 2C-1-100C-R

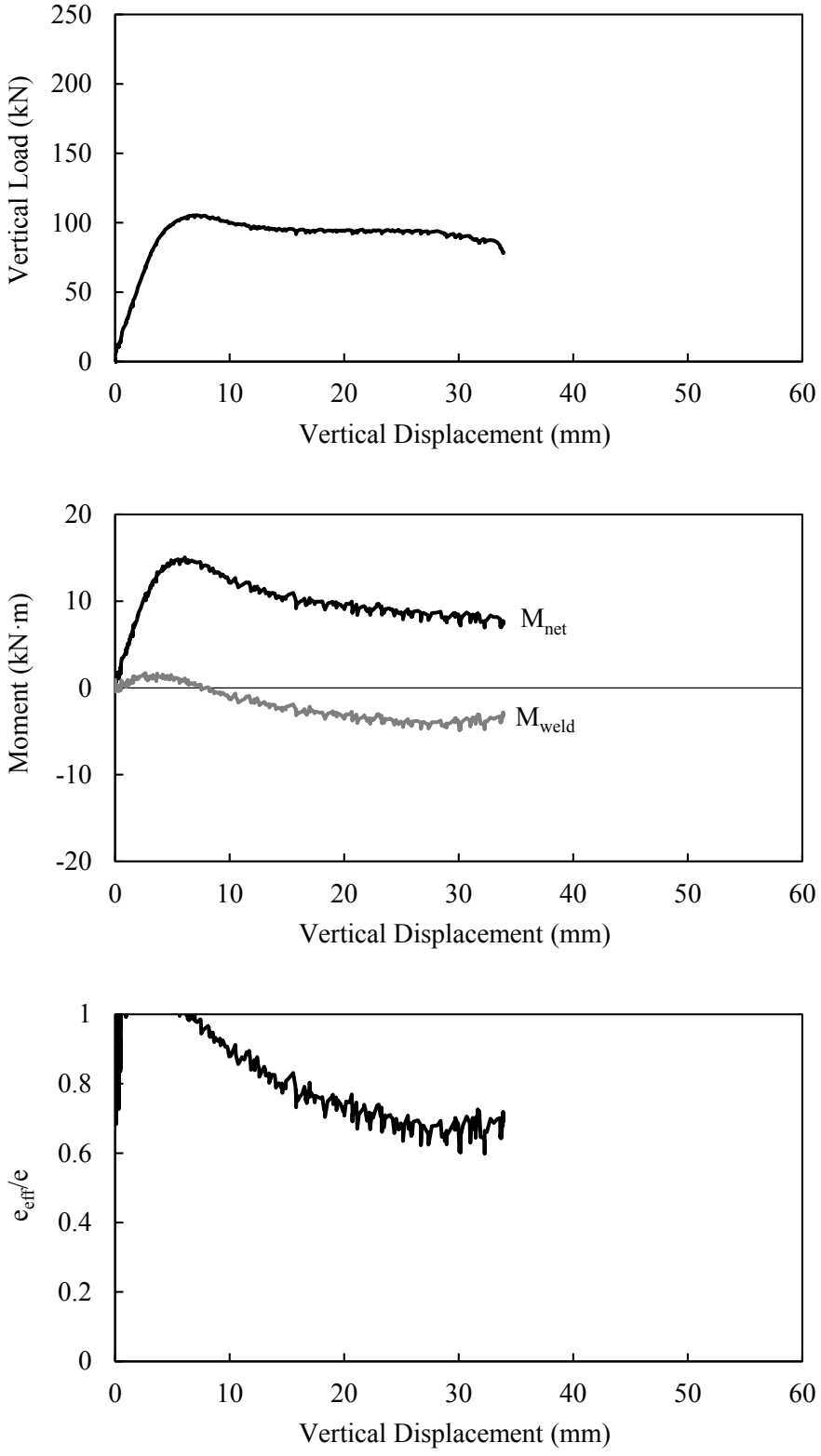

Figure C-14: Specimen 2D-2-0-NR

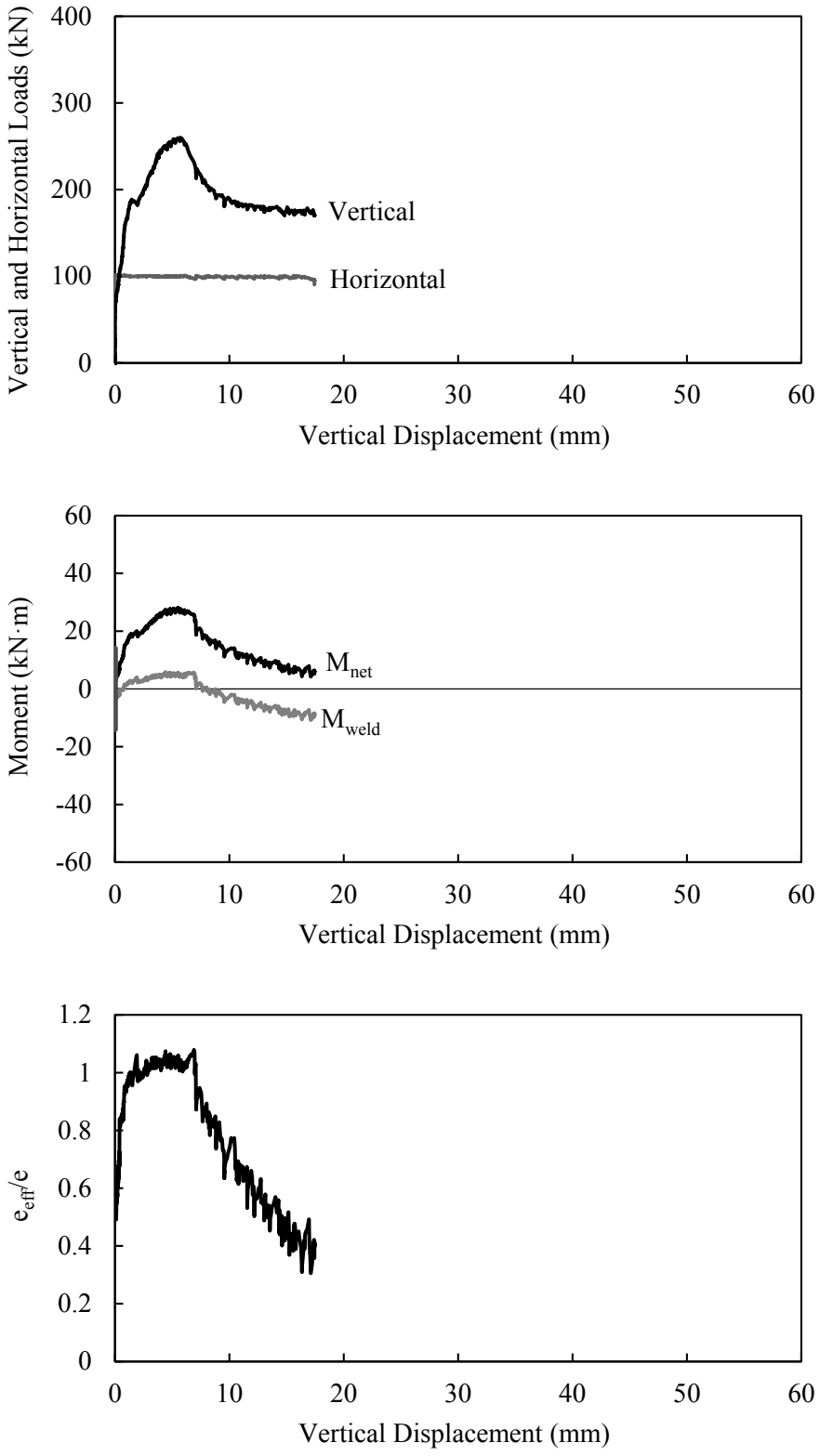

Figure C-15: Specimen 3A-1-100C-NR

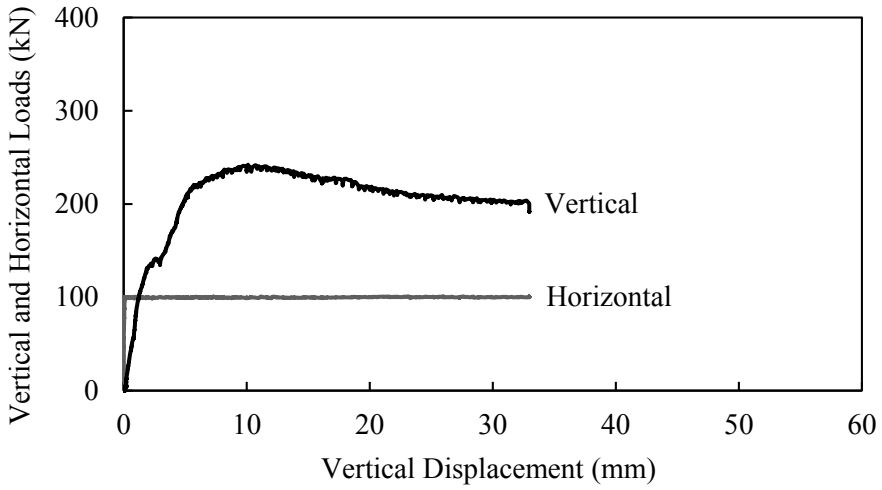

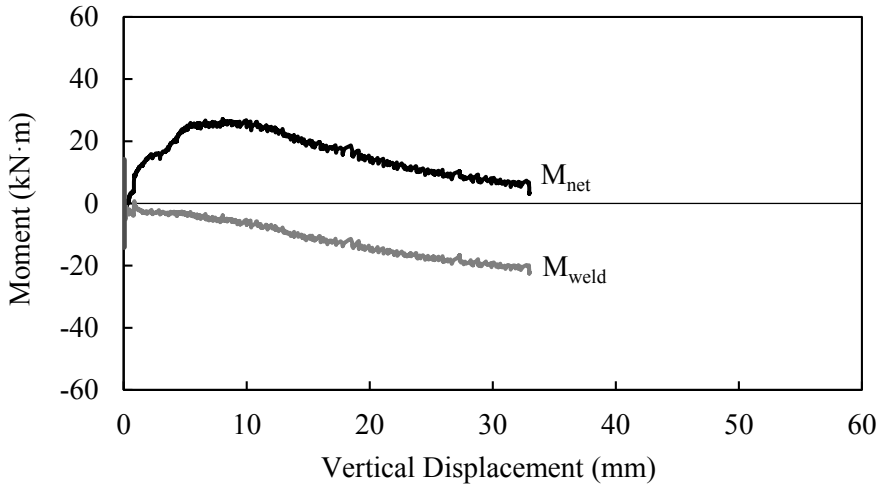

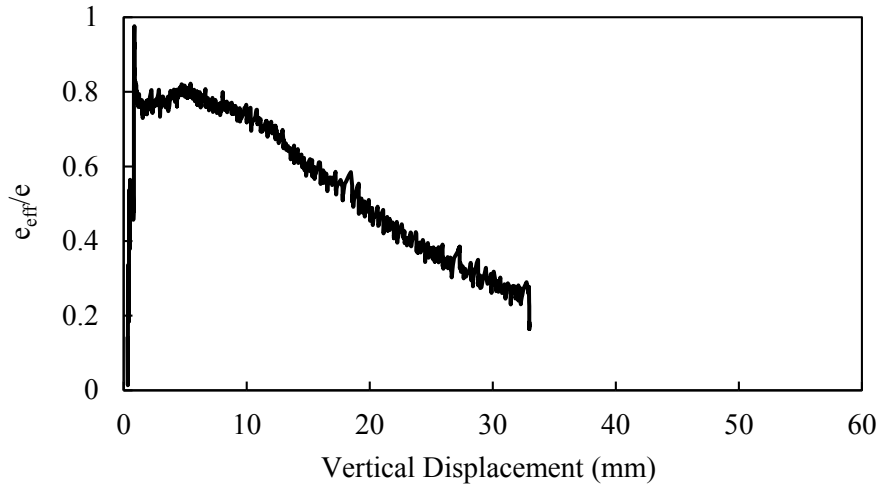

Figure C-16: Specimen 3A-2-100T-NR

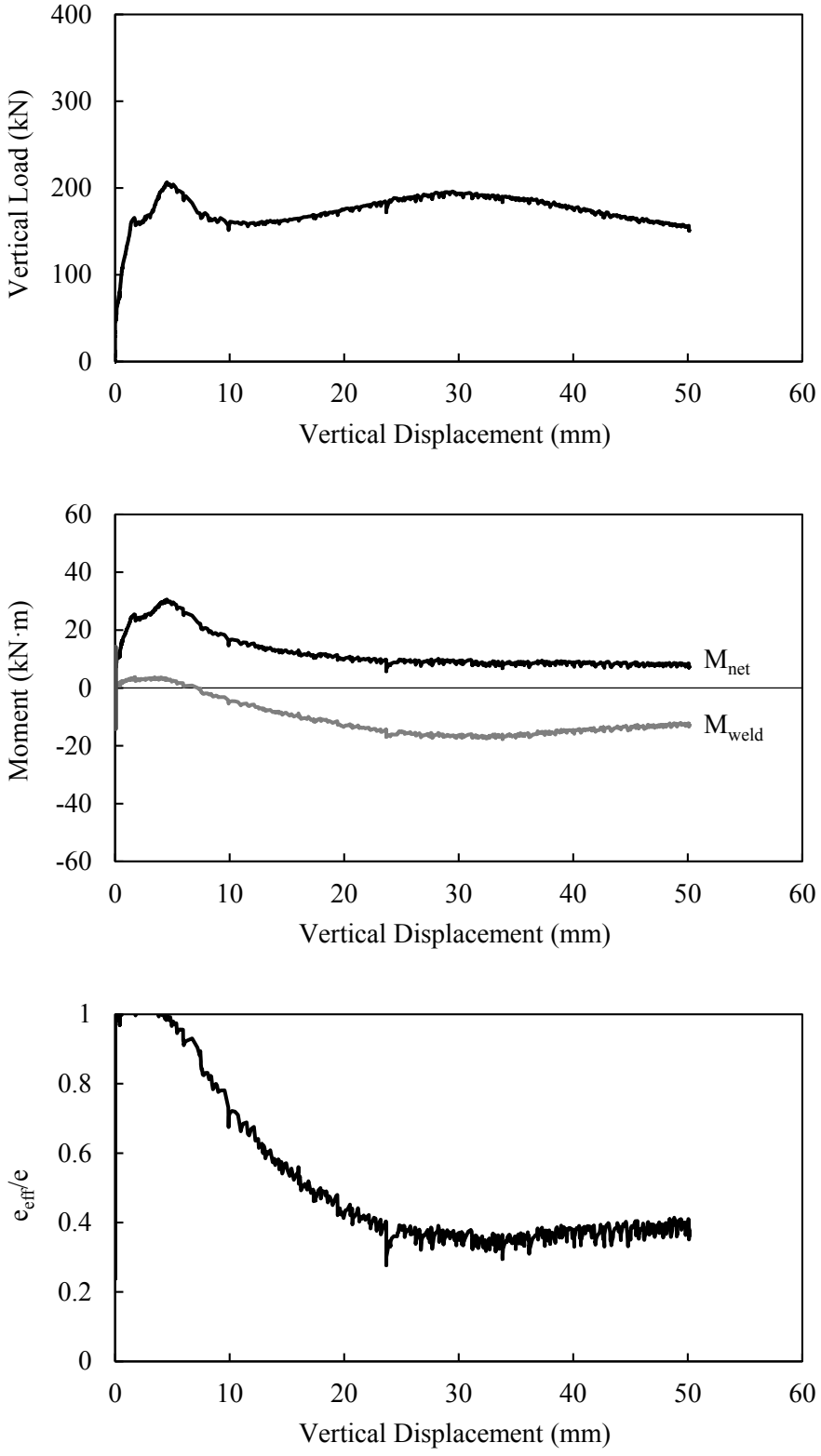

Figure C-17: Specimen 3A-2-0-NR

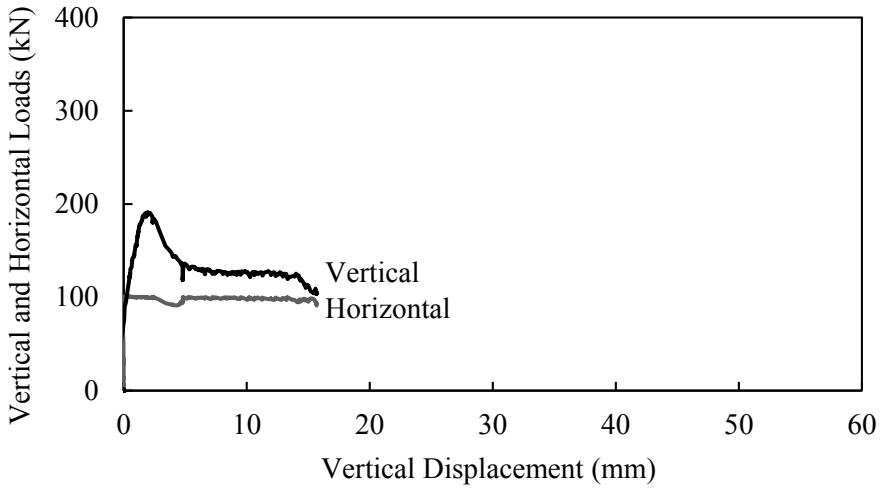

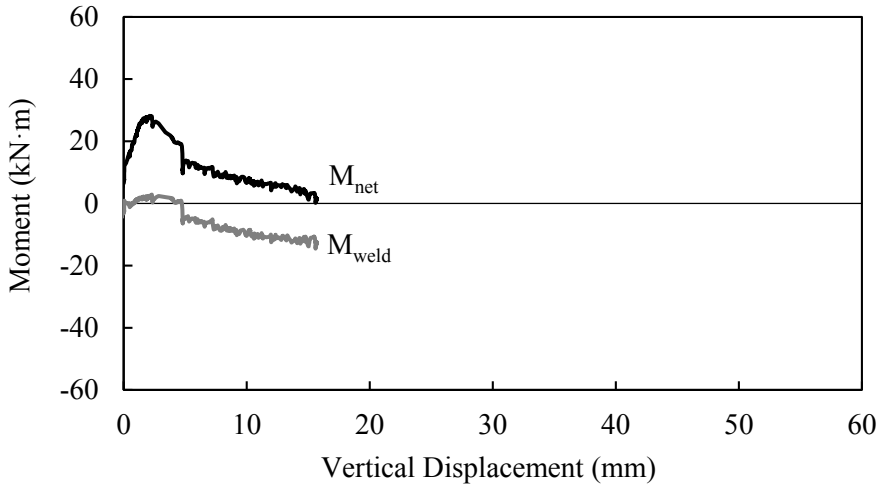

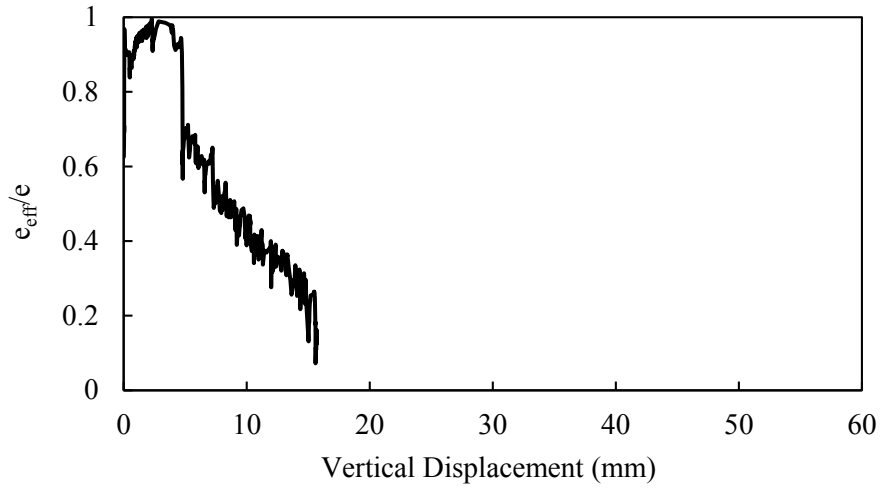

Figure C-18: Specimen 3A-2-100C-NR

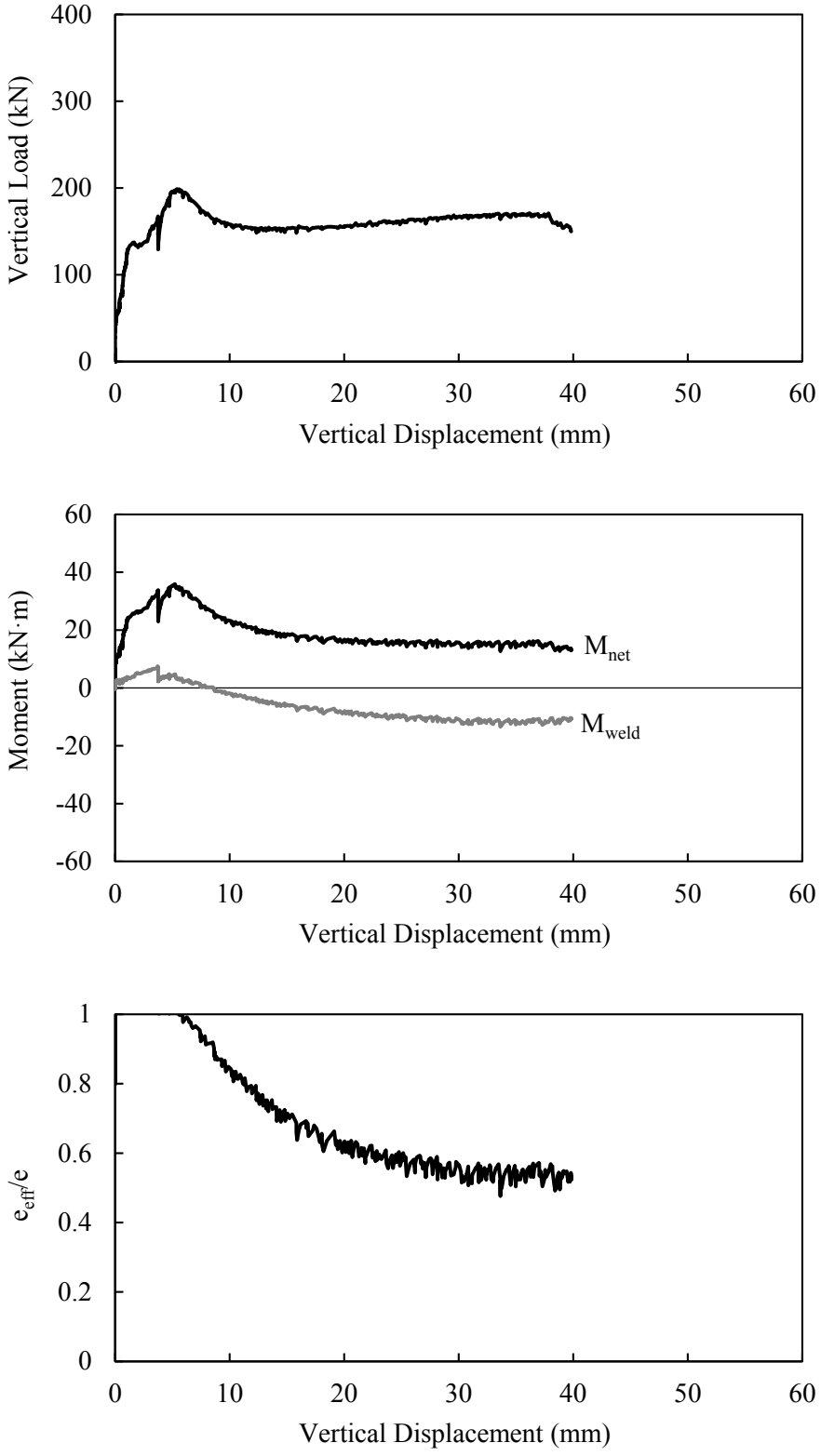

Figure C-19: Specimen 3A-3-0-NR

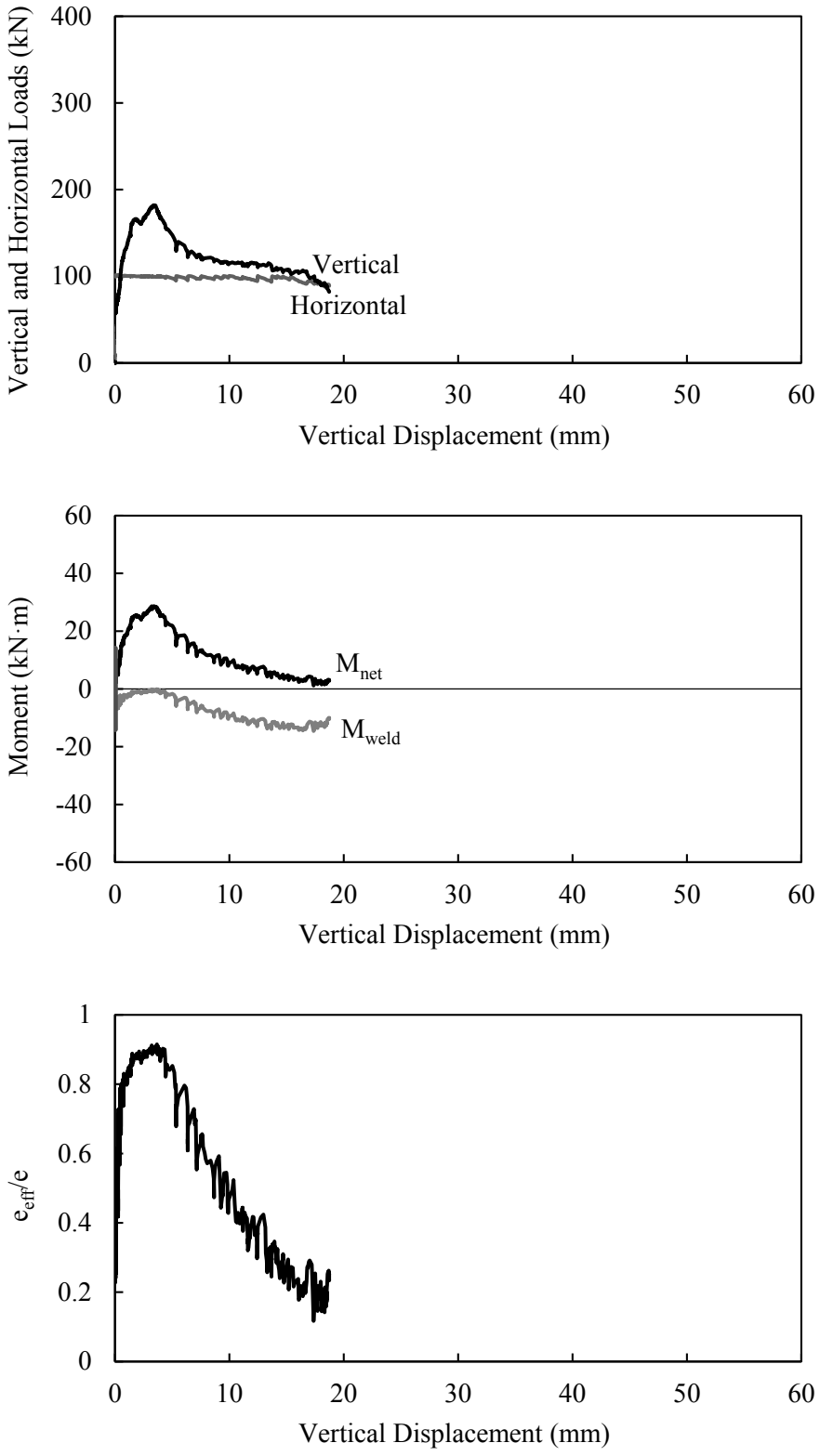

Figure C-20: Specimen 3A-3-100C-NR

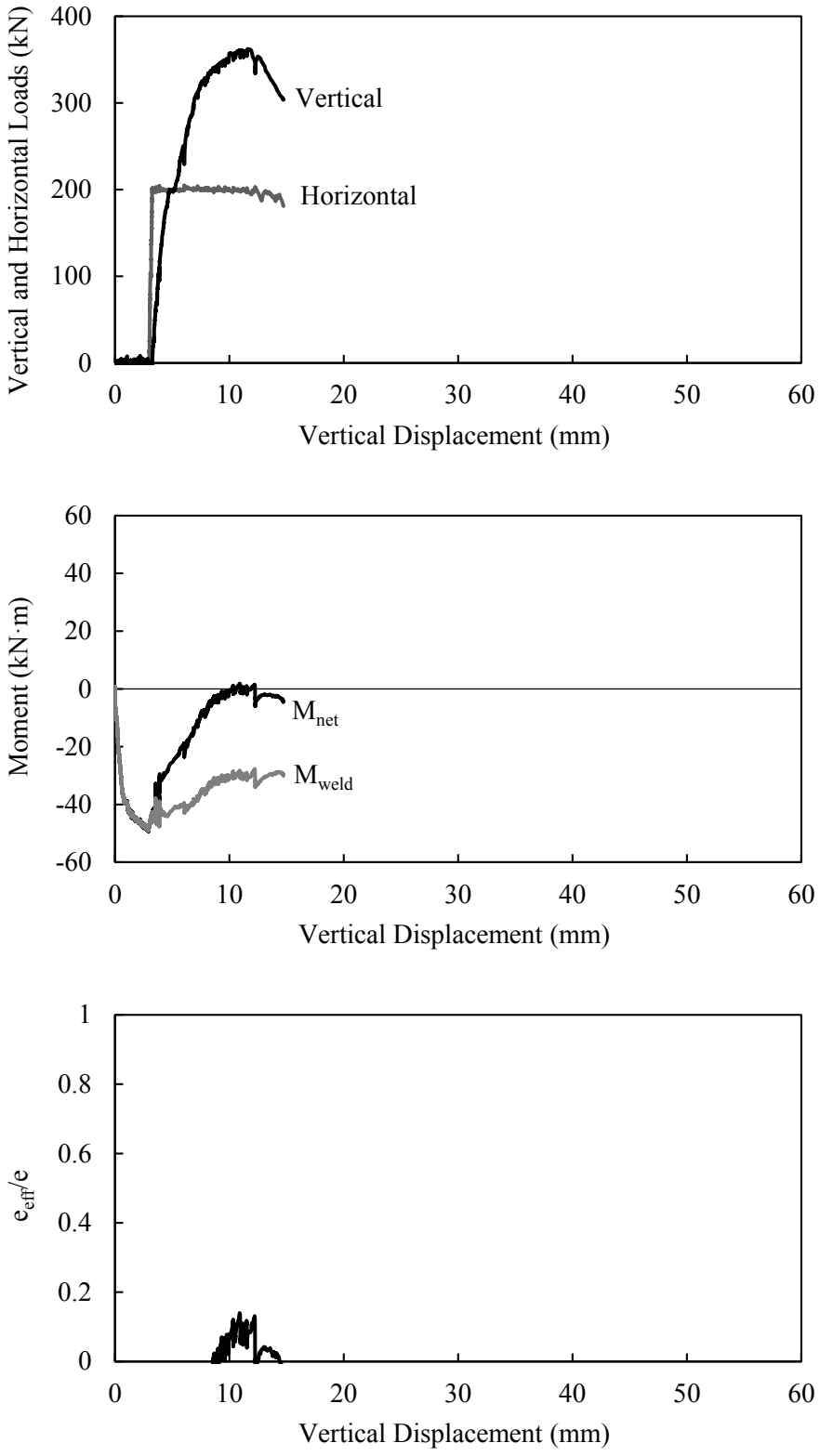

Figure C-21: Specimen 3B-1-200C-R

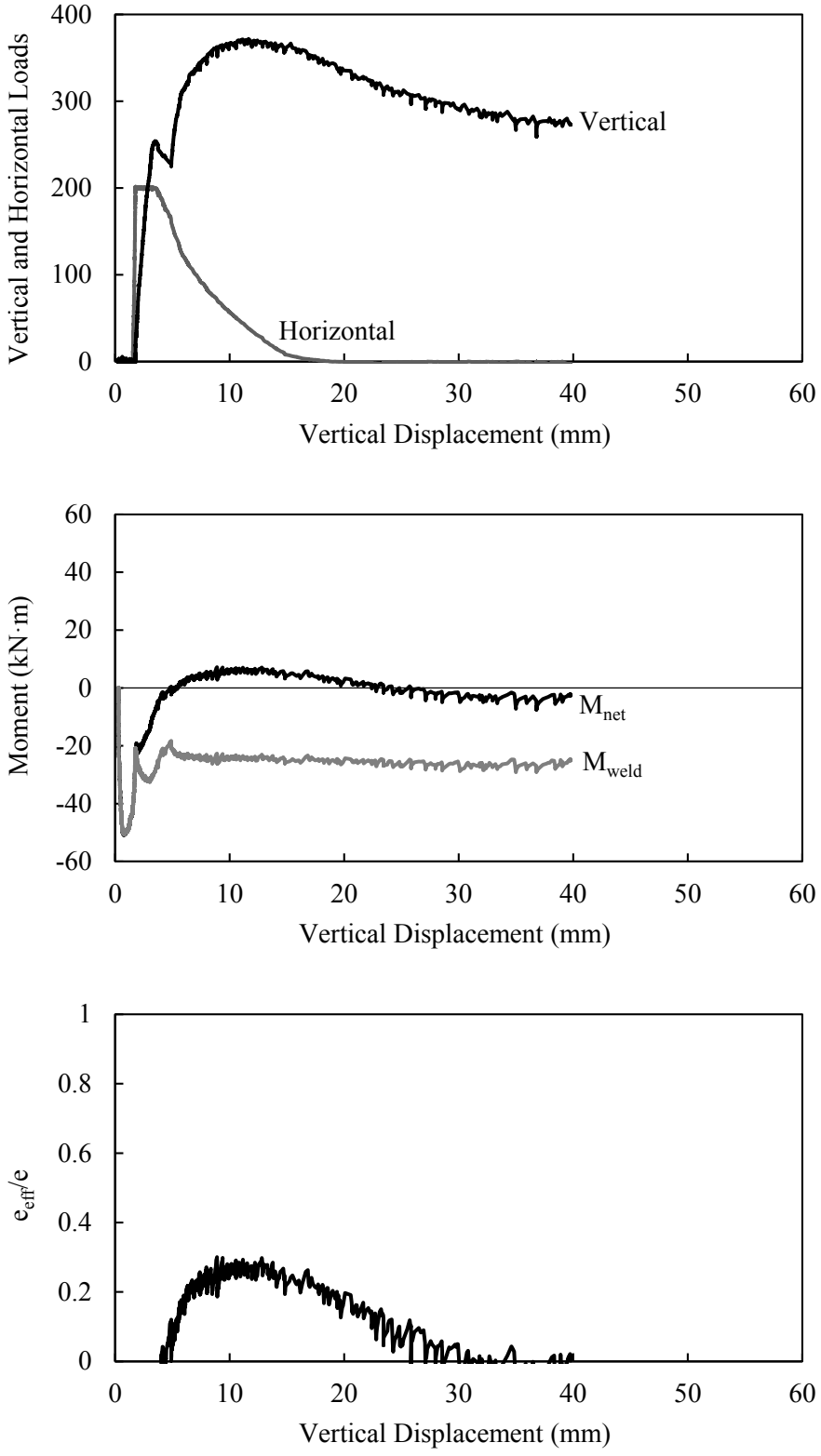

Figure C-22: Specimen 3C-1-200C-NR

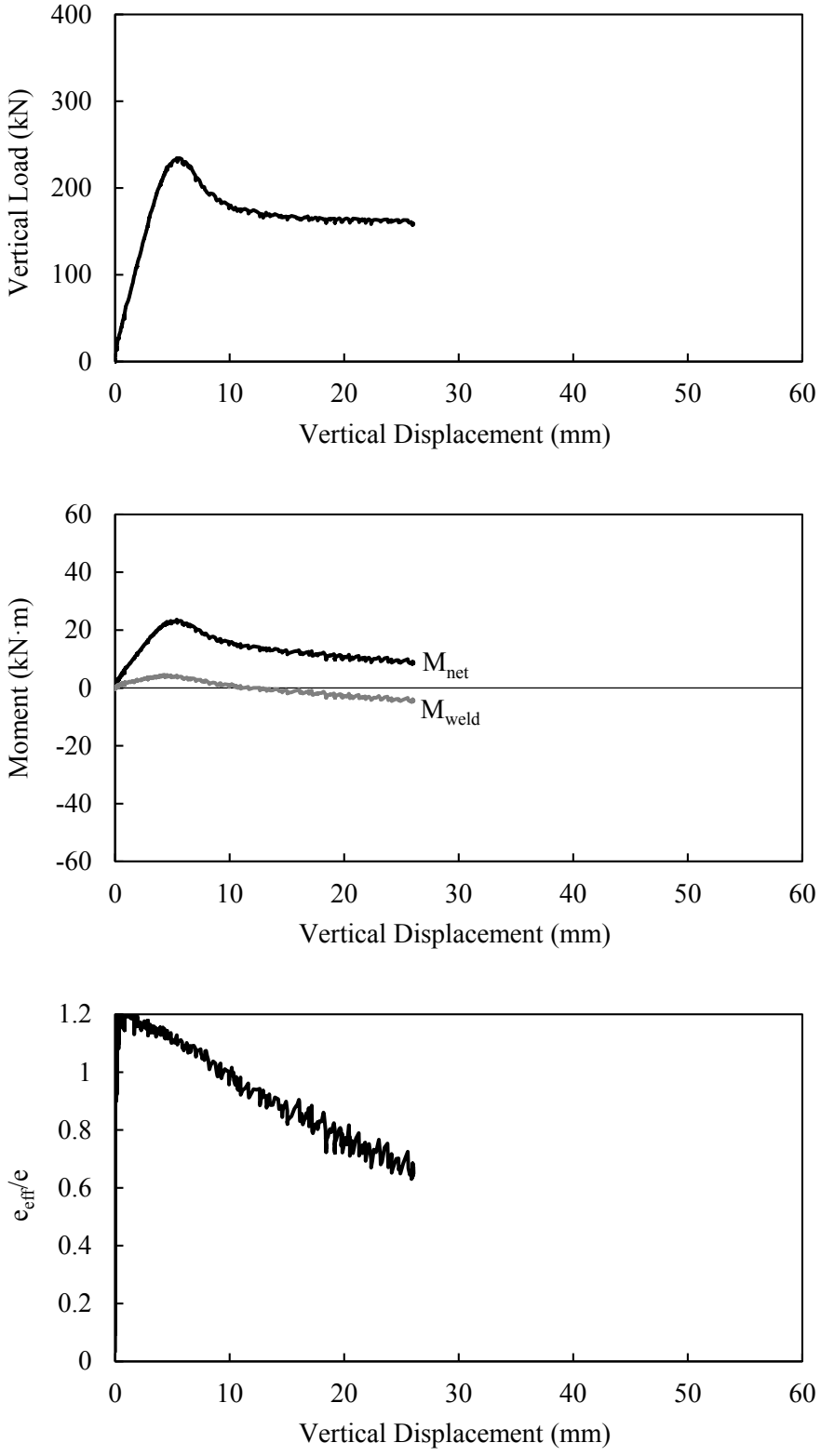

Figure C-23: Specimen 3D-2-0-NR

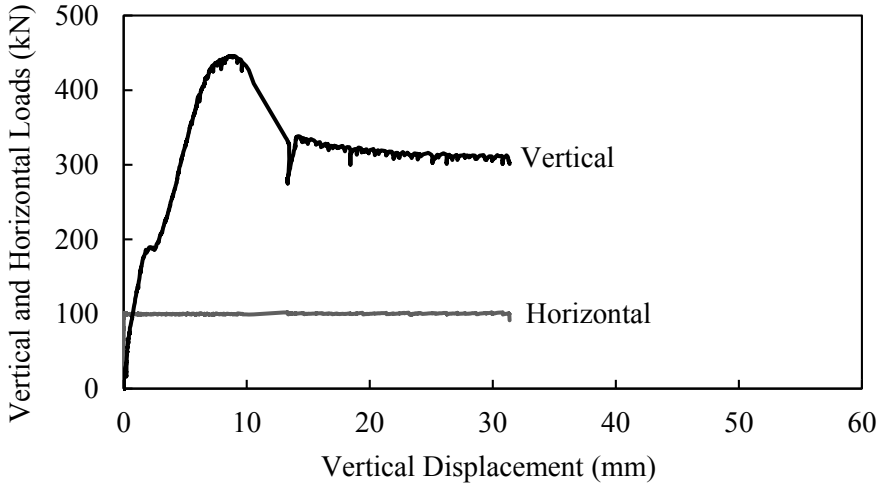

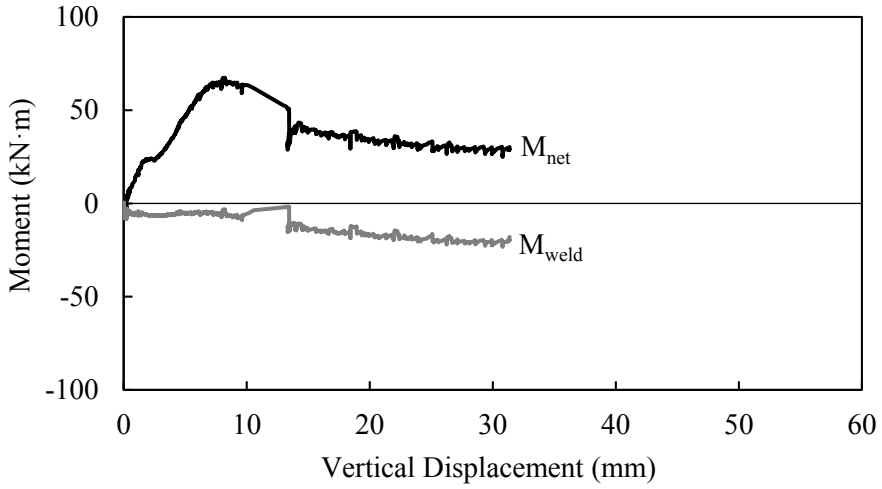

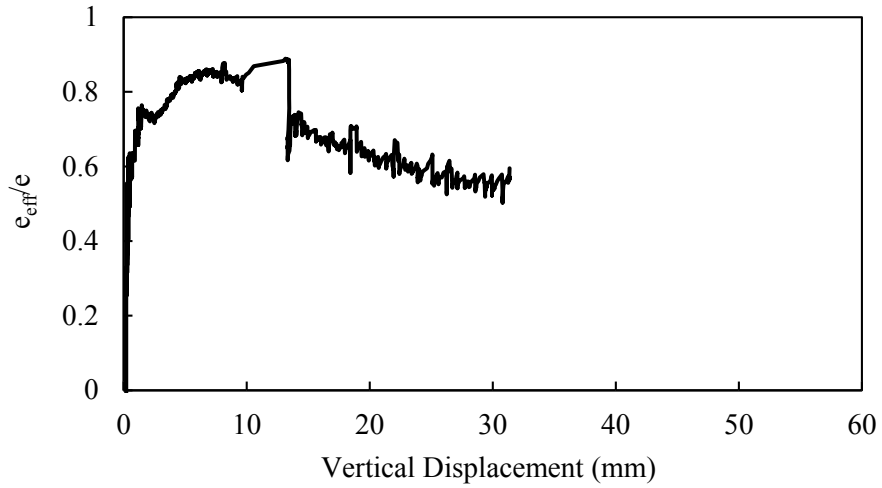

Figure C-24: Specimen 4A-3-100T-NR

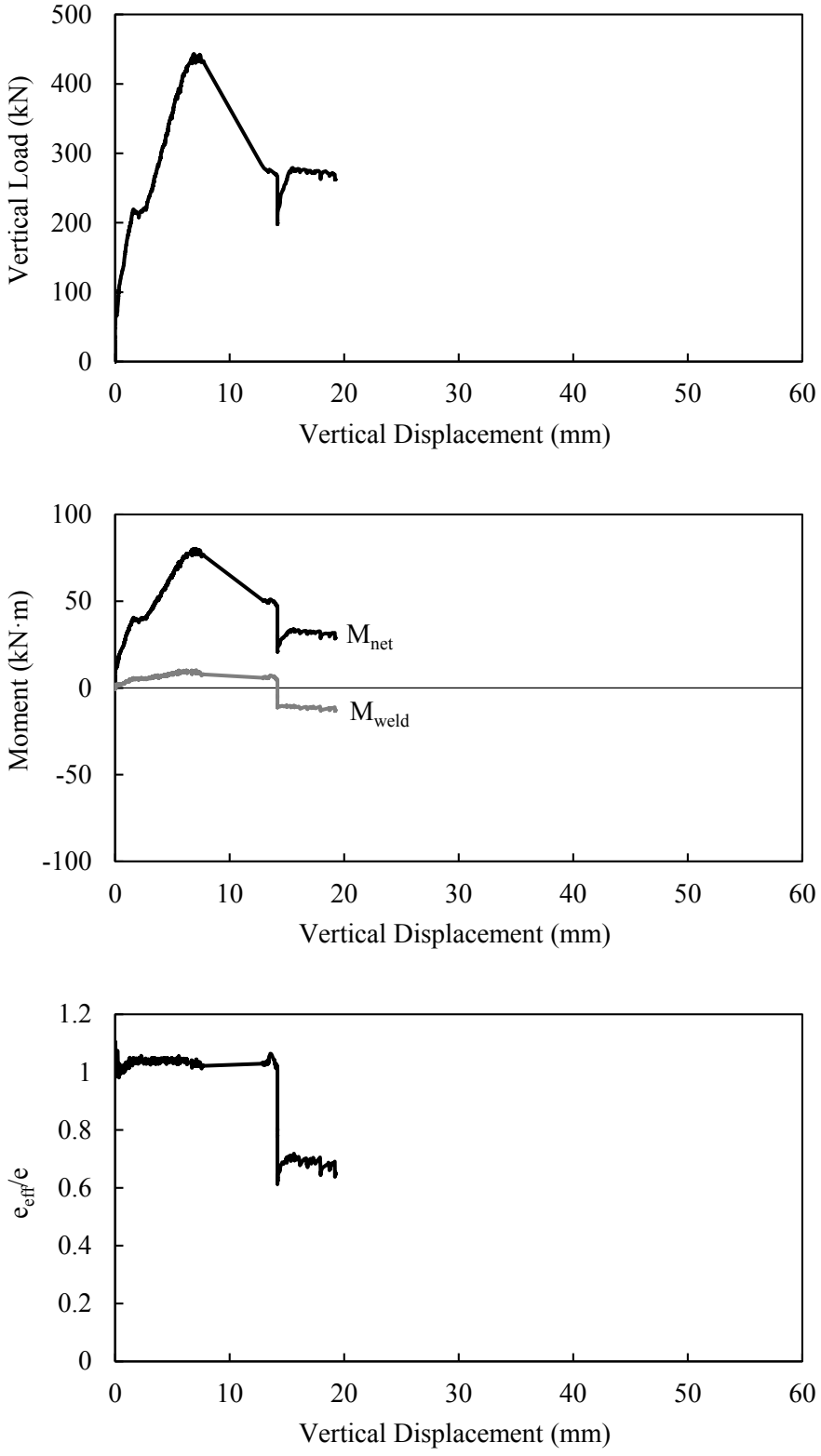

Figure C-25: Specimen 4A-3-0-NR

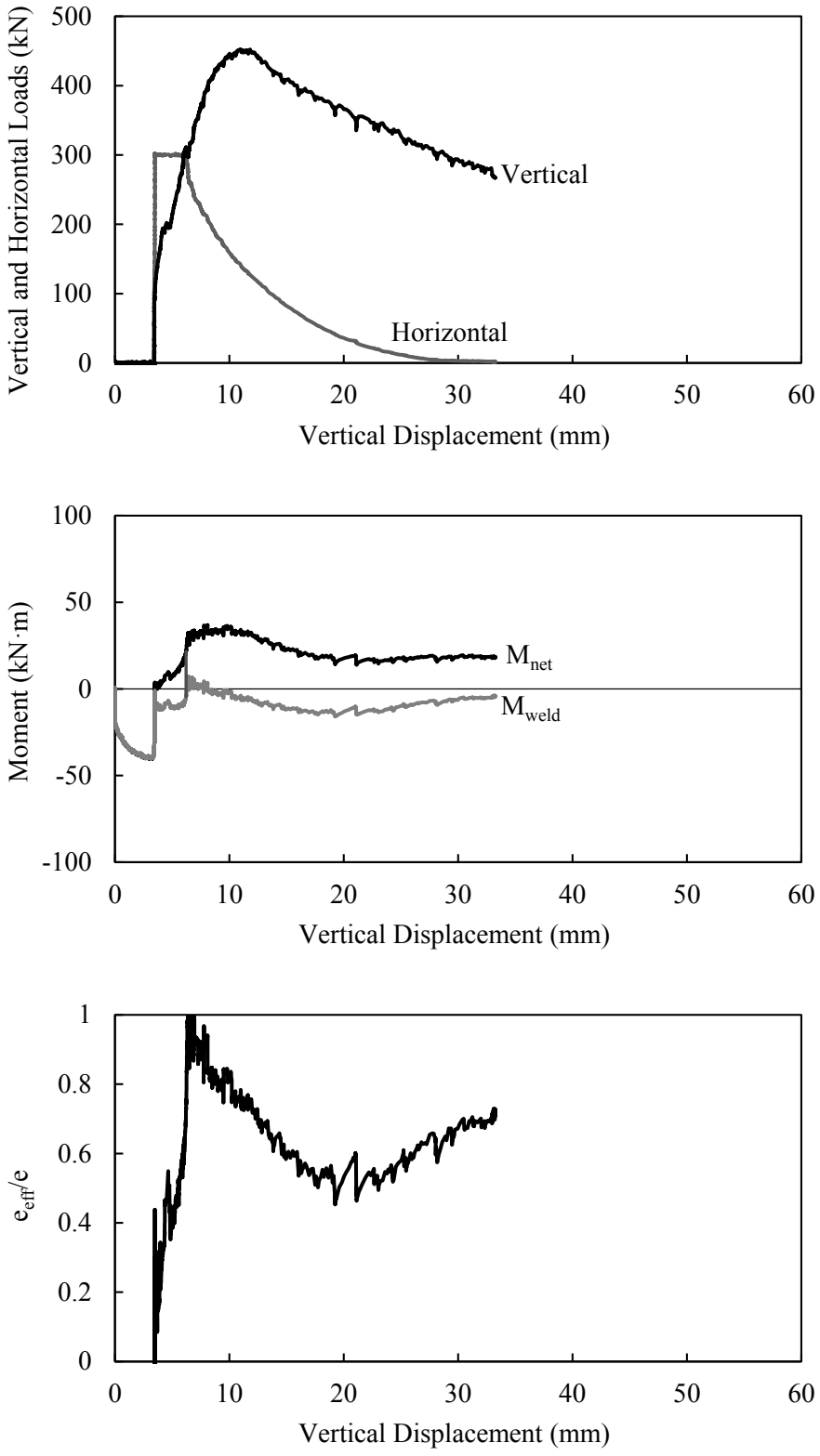

Figure C-26: Specimen 4B-1-300C-R

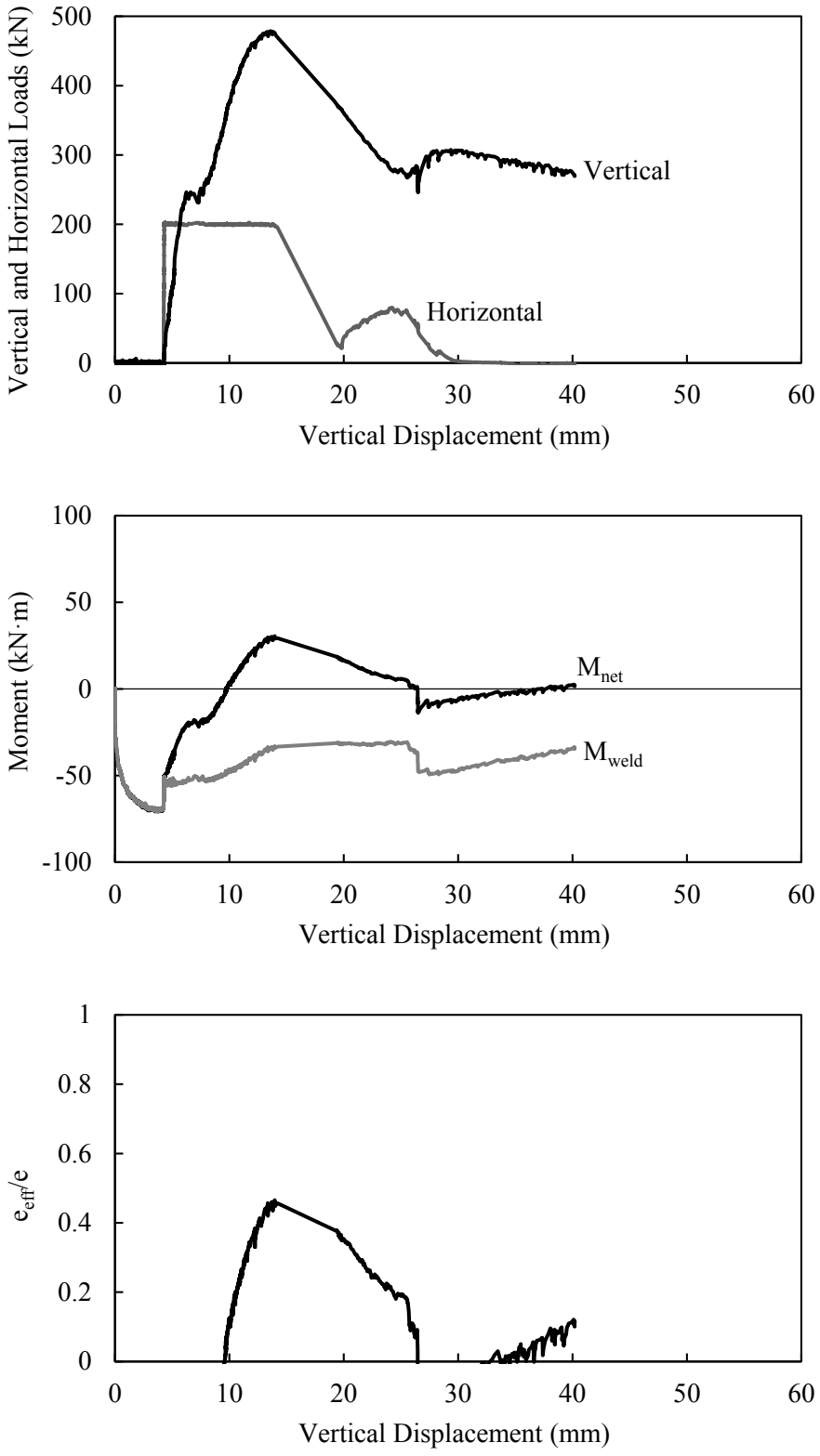

Figure C-27: Specimen 4B-2-200C-R

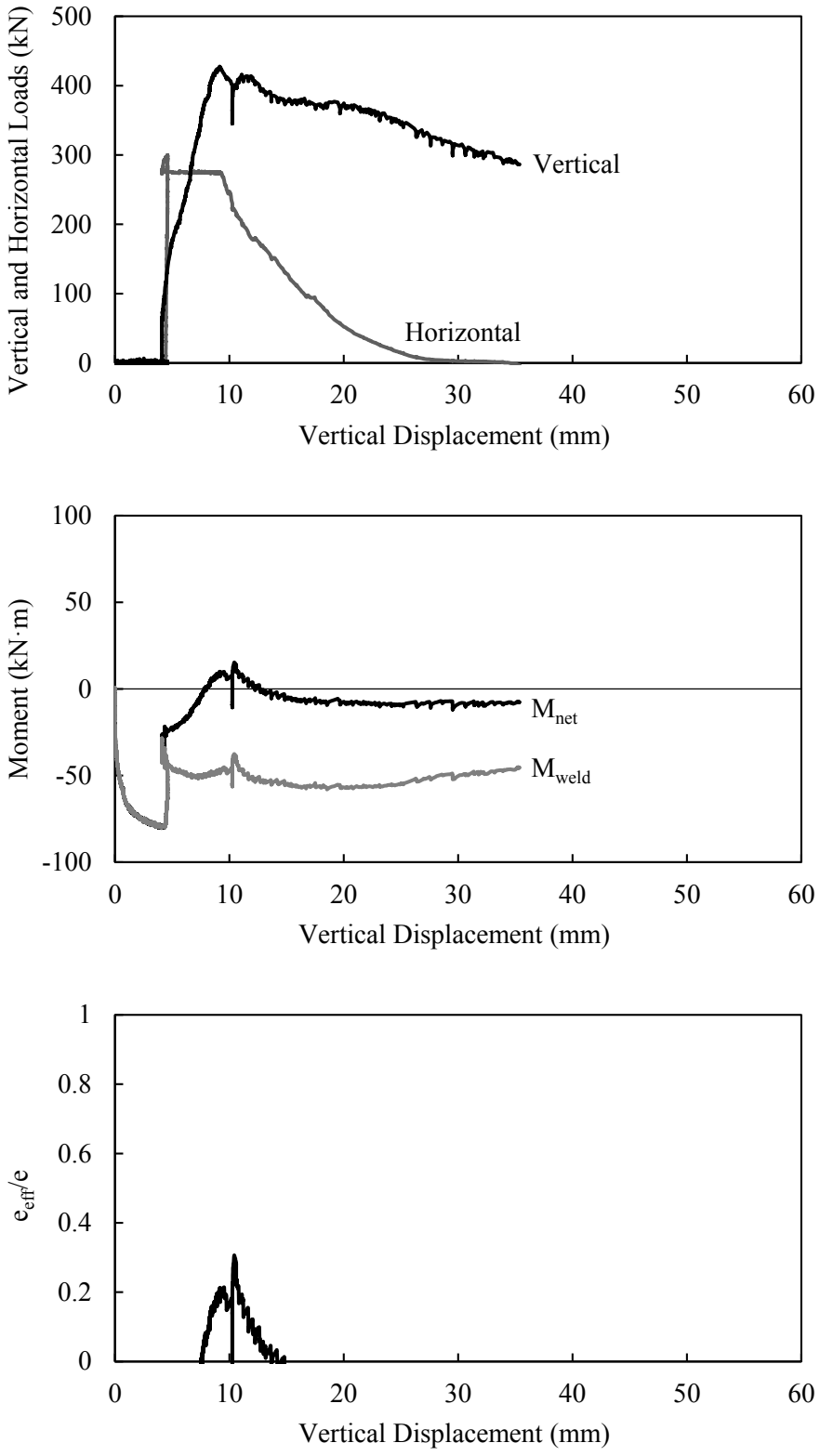

Figure C-28: Specimen 4B-2-300C-R

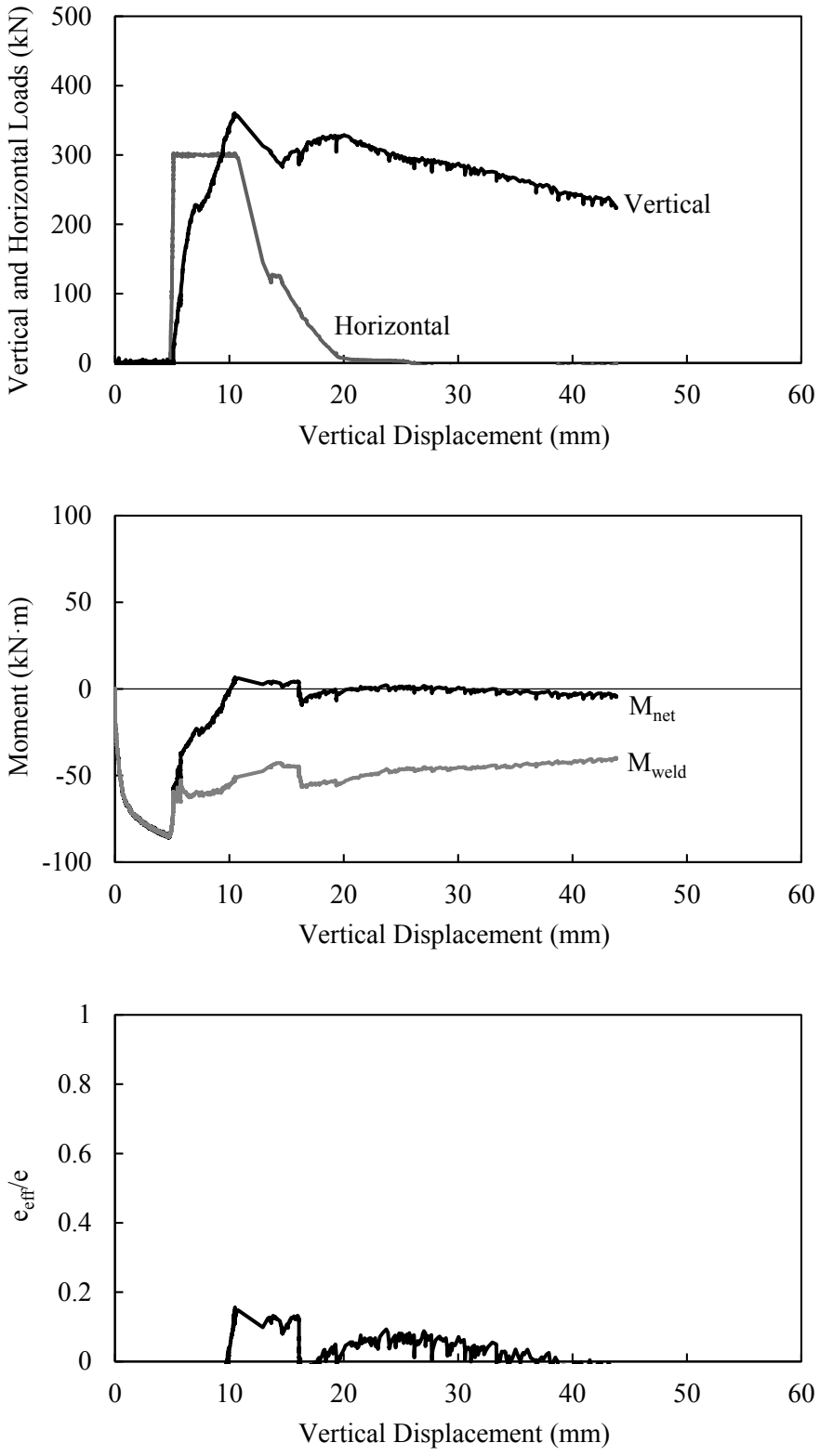

Figure C-29: Specimen 4B-3-300C-R